Calibration of Effective Pressure Coefficient for the Gulf of Mexico

……

An Abstract of a Dissertation

Presented to

the Faculty of the Department of Earth and Atmospheric Sciences

University of Houston

……

In Partial Fulfillment

of the Requirements for the Degree

Doctor of Philosophy

……

By

Hua Yu

May 2013

Calibration of Effective Pressure Coefficient for the Gulf of Mexico

_____

Hua Yu

APPROVED:

_____

Dr. Fred Hilterman, Supervisor
Department of Earth and Atmospheric Sciences

_____

Dr. John Castagna, Committee Chair
Department of Earth and Atmospheric Sciences

_____

Dr. Aibing Li, Committee member
Department of Earth and Atmospheric Sciences

_____

Dr. Dan Ebrom, Committee member
Statoil Company

_____

Dean, College of Natural Sciences and Mathematics

ACKNOWLEDGEMENTS

First and foremost, I would like to thank my advisor, Dr. Fred Hilterman. Without his support I couldn't finish this work. Every time I have questions he is always patient to answer them and gives very insightful comments about that. Whenever I am stuck at some places, he sits down and discusses with me about all the possible paths I can explore. He teaches me amazing Excel programming skills! Besides giving me detailed instruction and supervision about research, he also shares his study and work experience with me, which encourages me to overcome obstacles on the path of PhD study. His curiosity about scientific questions, keen about cutting edge technology, rigorousness altitude towards research sets up an excellent model for me. I can't say thank you enough to him.

I also want to thank my committee members: Dr. John Castagana, Dr. Aibing Li, and Dr. Dan Ebrom. Special thanks go to Dr. Castagna, who serves as my committee chair and gives me a lot of stimulating suggestions about research. I want to thank Dr. Aibing Li for her directions about my graduate program design and discussion about thesis. I also appreciate her recommendations without reservation for scholarship application every time, which encourages me to achieve more outstanding academic excellence and financially helps me during these four years. I want to thank Dr. Dan Ebrom for serving in my thesis committee, inviting me to the geopressure conference, and giving me very constructive suggestions about research topic.

I would like to thank Ms. Laura Bell, Ms. Tram Nguyen, Ms. Smita Ketkar, Ms. Sylvia Marshall, Ms. Ashley Tran, Ms. Zara Gaitan, Mr. Jay Krishnan, Mr. Jason Ognosky and other department staff, who provides a lot of help to me. I also want to thank my peers Arnold, Ayo, Luanxiao, and other office mates for their friendship and support.

Last, but not least, I am grateful to all of my family, especially my parents and my husband. Without their unlimited support all these years I couldn't continue my graduate study. Finally I want to thank my two lovely kids, Brian and Michelle; they are the most precious gifts I have. Their smiles are always the power for me to conquer all difficulties ahead.

Calibration of Effective Pressure Coefficient for the Gulf of Mexico

……

An Abstract of a Dissertation

Presented to

the Faculty of the Department of Earth and Atmospheric Sciences

University of Houston

……

In Partial Fulfillment

of the Requirements for the Degree

Doctor of Philosophy

……

By

Hua Yu

May 2013

ABSTRACT

Pore pressure prediction provides an important risk assessment in the oil and gas industry. It is widely used to estimate the seal integrity, reservoir pressure compartmentalization, hydrocarbon column height, and to design the optimum well mud weight and casing programs. This work ties pore pressure prediction to estimates of the effective pressure coefficient n. In many pore pressure predictions, the differential pressure rather than the effective pressure is estimated from velocity measurements as a value of 1 is assumed for n. In addition, the estimation of a Normal Compaction Trend (NCT) for shale velocity is compromised because of transitional disequilibrium at shallow depths. To compensate for this, we depth adjust the initial shale velocity NCT. Then, n is calibrated with well-log data in two different Gulf of Mexico (GOM) pressure regimes: compaction disequilibrium and unloading/clay digenesis processes. Values for n in abnormal pressure zones are approximately 0.83. Our pore pressure predictions based on the adjusted shale velocity NCT and the depth-calibrated n are consistent with measured mud weight profiles. For extending the results to areas where there is not sufficient well control to calibrate n, it can be inverted from Gassmann's equation. S-wave velocity decreases more than P-wave velocity below the onset of abnormal pressure, which is only 90% of Greenberg-Castagna estimation. Overall this study develops a consistent method to predict pore pressure in the GOM by incorporating reliable NCT and variations in the pore pressure coefficient, n, that result from different degrees of consolidation.

CONTENTS

LIST OF FIGURES

LIST OF TABLES

ABBREVIATIONS

P_P	Pore Pressure	K_{dry}	Dry Rock Bulk Modulus
P_E	Effective Pressure	K_{sat}	Saturated Rock Bulk Modulus
P_C	Confining Pressure	μ_{dry}	Dry Rock Shear Modulus
P_D	Differential Pressure	μ_{sat}	Saturated Rock Shear Modulus
V_P	Observed P-wave Velocity	K_{ma}	Matrix Bulk Modulus
V_S	Observed S-wave Velocity	K_{fl}	Fluid Bulk Modulus
n	Effective Pressure Coefficient	μ_{ma}	Matrix Shear Modulus
β	Biot Coefficient	NCT	Normal Compaction Trend
GOM	Gulf of Mexico	GP	Geopressure

1 INTRODUCTION

1.1 Effective stress law

Fundamental studies on elastic deformation of porous rocks (e.g. Biot, 1941; Gassmann, 1951; Geertsma, 1957; Fatt, 1958; Skempton, 1960) stated that for a microscopically homogeneous isotropic rock the stress and strain relationship is (Nur and Byerlee, 1971):

$$\varepsilon_{ij} = \frac{1}{2\mu}\left(\sigma_{ij} - \frac{1}{3}\sigma_{rr}\delta_{ij}\right) + \frac{1}{9K_{dry}}\left(\sigma_{rr}\delta_{ij}\right) - \frac{1}{3H}\left(P_P\delta_{ij}\right), \quad (1\text{-}1)$$

where ε_{ij} is a second rank strain tensor, which is

$$\varepsilon_{ij} = \begin{bmatrix} \varepsilon_{11} & \varepsilon_{12} & \varepsilon_{13} \\ \varepsilon_{21} & \varepsilon_{22} & \varepsilon_{23} \\ \varepsilon_{31} & \varepsilon_{32} & \varepsilon_{33} \end{bmatrix}.$$

σ_{ij} is a second rank stress tensor, which is

$$\sigma_{ij} = \begin{bmatrix} \sigma_{11} & \sigma_{12} & \sigma_{13} \\ \sigma_{21} & \sigma_{22} & \sigma_{23} \\ \sigma_{31} & \sigma_{32} & \sigma_{33} \end{bmatrix}.$$

σ_{rr} is the summation of principle stress, which is

$$\sigma_{rr} = \sigma_{11} + \sigma_{22} + \sigma_{33}.$$

δ_{ij} is Kroenecker's delta function, which is

$$\delta_{ij} = \begin{cases} 1 & i = j. \\ 0 & i \neq j. \end{cases}$$

K_{dry} is the dry rock bulk modulus; μ is shear modulus, and H is an elastic constant describing the incompressibility of the rock for a change of fluid pressure (Biot, 1941). Those coefficients can be determined with laboratory measurements. P_P is pore pressure in the pore space.

Nur and Byerlee (1971) differentiated the stress which produced the total strain on a porous rock into three parts: deviatoric stress, principle stress, and pore pressure. They are the three terms listed on the right side of equation (1-1). From equation (1-1) the volumetric strain θ can be expressed as

$$\theta = (\varepsilon_{11} + \varepsilon_{22} + \varepsilon_{33}) = \frac{1}{K}(P_C - \alpha P_P) \ , \qquad (1\text{-}2)$$

where P_C is confining pressure

$$P_C = \frac{1}{3}(\sigma_{11} + \sigma_{22} + \sigma_{33}).$$

The format of Equation (1-2) indicates that the volumetric strain θ is a function of a new quantity, $(P_C - \alpha P_P)$, which is defined as an effective pressure P_E by Nur and Byerlee (1971),

$$P_E = (P_C - \alpha P_P). \qquad (1\text{-}3)$$

Now the volumetric strain depends on one parameter, P_E. α, or n in this study is the effective pressure coefficient, which equals

$$\alpha = \frac{K_{dry}}{H}.$$

Equation (1-3) is the exact expression for the effective stress law, which means "the deformation and strength of porous bodies are neither proportional to the confining pressure nor to the pore pressure but to the difference between them, named 'effective pressure', P_E" (Kümpel, 1991). This effective stress law is the focus of our study.

The theory of the effective stress law can be traced back to Karl von Terzaghi in 1923 (Bjerrum et al, 1960). But in their theory, they thought the effective pressure coefficient n is unity, which means the measurable deformation from a change of stress depends only on the changes in differential pressure P_D, which is defined as net difference between confining pressure and pore pressure as

$$P_D=P_C-P_P. \tag{1-4}$$

This statement holds for large porosity sediments, especially for saturated clay (Terzaghi, 1936). This principle has been primary importance in soil mechanics (Bjerrum et al, 1960).

Numerous theoretical and laboratory works have been done to constrain the quantity n (e. g. Hicks and Berry, 1956; Wyllie et al., 1958; Nur and Byerlee, 1971; Berryman, 1992, 1993). Nur and Byerlee (1971) theoretically demonstrated that for static elastic deformation the effective pressure coefficient equals the Biot-Willis coefficient, β (Biot and Willis, 1957), as shown in equation (1-5).

$$n=\beta=1-\left(\frac{K_{dry}}{K_{ma}}\right), \tag{1-5}$$

where K_{ma} is rock matrix bulk modulus.

However Nur and Byerlee (1971) warned "the effective stress law…is applicable only to elastic strain…and it is not applicable to…velocities of elastic waves." Berryman (1992, 1993) demonstrated that different rock properties, such as total volume, pore volume, fluid content, porosity, solid volume, electrical conductivity, and fluid permeability for inhomogeneous rocks have different effective stress coefficients.

1.2 Seismic velocity response to effective pressure

Pressure plays an important role in influencing the rock compaction process and therefore, influencing the seismic velocities (Sayers, 2010). There are two types of pressure variations that are normally considered and these were developed in the previous section. One is overburden pressure or confining pressure P_C, which is caused by the weight of the overlying rock including the pore fluid. It squeezes the rock that makes the rock stiffer and more compacted; therefore, when the seismic wave propagates through the rock, seismic velocity tends to increase. The other pressure is the pressure exerted on the fluid held within the rock pore space, which is referred as pore pressure P_P. Pore pressure counteracts the overburden pressure. It attempts to push the grains apart; therefore, the seismic velocity will decrease when a seismic wave propagates through the rock. The seismic velocity variation with pressure obeys the effective pressure law (e.g. Eberhart-Phillips et al., 1989; Khaksar and Griffiths, 1996), but effective pressure often means differential pressure (Sayers, 2010).

Pioneer work relating seismic velocity and effective pressure started in 1950s. Brandt (1955) is one of the first researchers to relate the effective pressure to seismic velocity from a theoretical analysis of the elastic wave propagation through packings of elastic spheres. He pointed out that acoustic velocity V_P, similar to other properties like strain, compressibility etc., is a function of effective pressure:

$$V_P=f(P_E)=f(P_C-nP_P), \tag{1-6}$$

where n is a fraction between zero and unity. In a theoretical approach, Gurevich (2004) proved under moderate stresses for a rock that is made up of a single elastic grain material, and fluid's compressibility is independent of pressure, the effective pressure coefficient for acoustic wave velocity equals unity. But he further pointed out this conclusion does not hold for heterogeneous rocks like shale.

A laboratory method to measure n is summarized by Todd and Simmons (1972) as

$$n=1-\frac{(\partial V_P/\partial P_P)_{P_D}}{(\partial V_P/\partial P_D)_{P_P}} . \tag{1-7}$$

The method as sketched by Hofmann et al. (2005) is shown in Figure 1-1. This suggests one can measure the gradient of V_P-P_P and V_P-P_D from laboratory results.

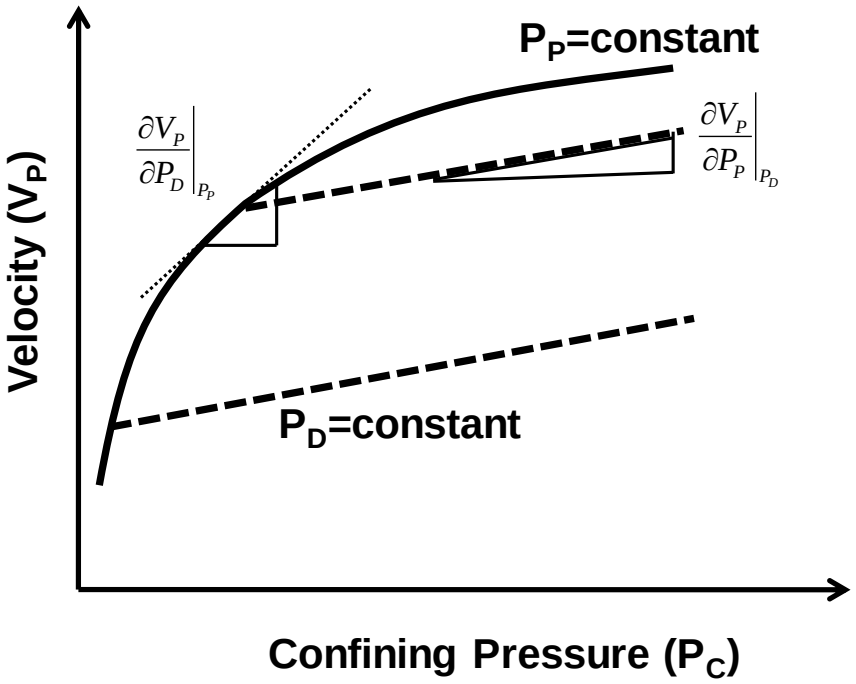

Figure 1-1: Illustration showing how to measure n in laboratory experiments (modified from Hofmann et al., 2005).

But, laboratory measurements show controversial values for n. Hicks and Berry (1956) and Wyllie et al. (1958) proposed equation (1-8), which means for high porosity sandstones (porosity approximately equal to 20%), the acoustic velocity is a function of differential pressure:

$V_P=f(P_D)=f(P_C-P_P)$. (1-8)

Their observations are represented by Figure 1-2, which revealed n is quite close to 1 as the V_P-P_D curve is a straight line. However, numerous other laboratory experiments indicate that n is less than one (e.g. Banthia et al., 1965; Todd and Simmons, 1972;

Christensen and Wang, 1985; Hornby, 1996; Sarker and Batzle, 2008). Their observations are represented by Figure 1-3.

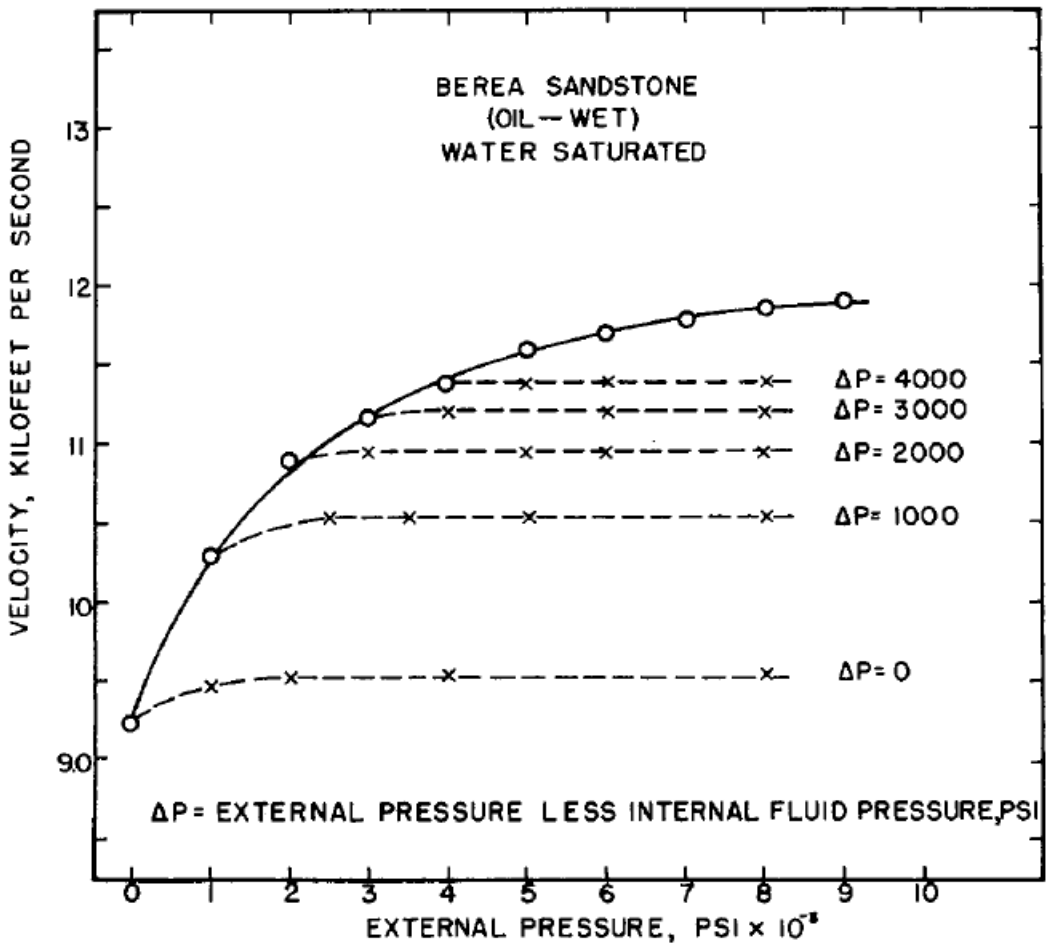

Figure 1-2: Influence of pore pressure on P-wave velocity for high porosity (20%) sandstone (Wyllie et al., 1958).

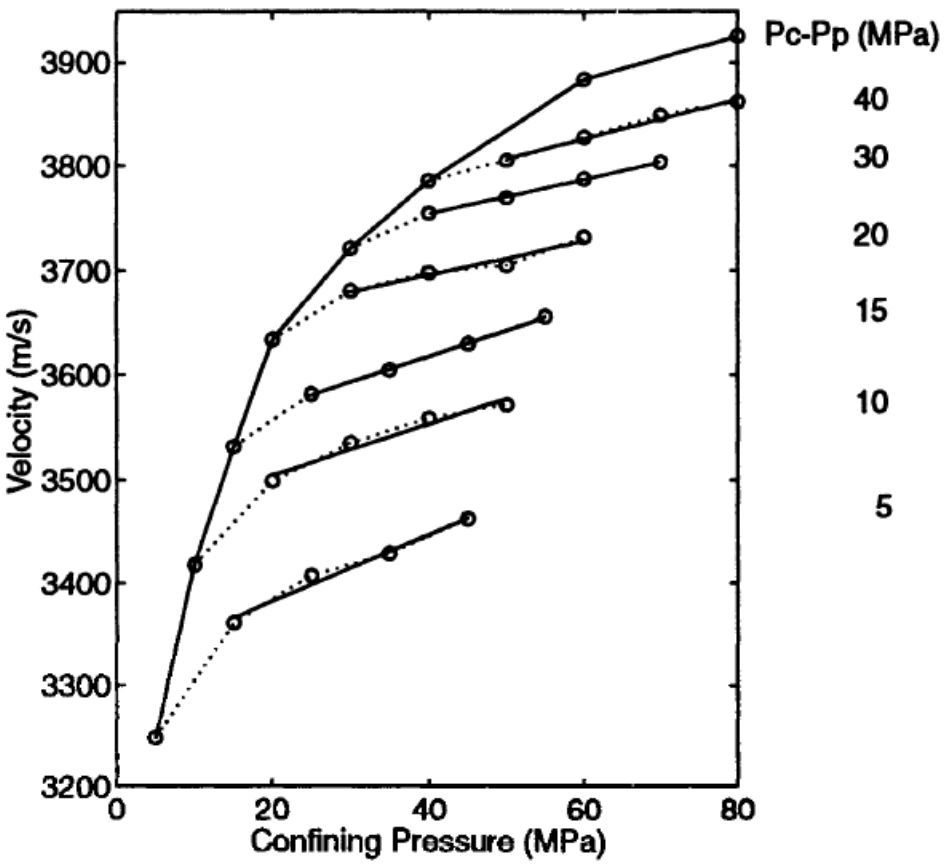

Figure 1-3: Influence of pore pressure on P-wave velocity for low porosity (9.1%) shale (from Hornby et al., 1996).

An interesting fact we found from the published experiments is that n values close to one were obtained from samples with high porosity, while n values appreciably less than unity are from experiments on samples with low porosity like granite (Todd and Simmons, 1972) or North Sea shale (Hornby, 1996; Sarker and Batzle, 2008). It seems there is a correlation between a rock's porosity and the n value. As sketched in Figure 1-4, for high-porosity rocks which are very compressible, velocity is essentially constant when the differential pressure is constant, so that velocity = $f(P_D)$ (Hicks and Berry, 1956;

Wyllie, et al., 1958). However, for low-porosity rocks which are more difficult to compress, velocity = $f(P_E)$. In a basin as rocks are buried deeper the porosity decreases exponentially (e.g. Athy, 1930; Mondol et al., 2007); and the compressibility of rocks decreases, therefore velocity becomes more sensitive to the confining pressure, meaning the effective pressure coefficient approaches zero.

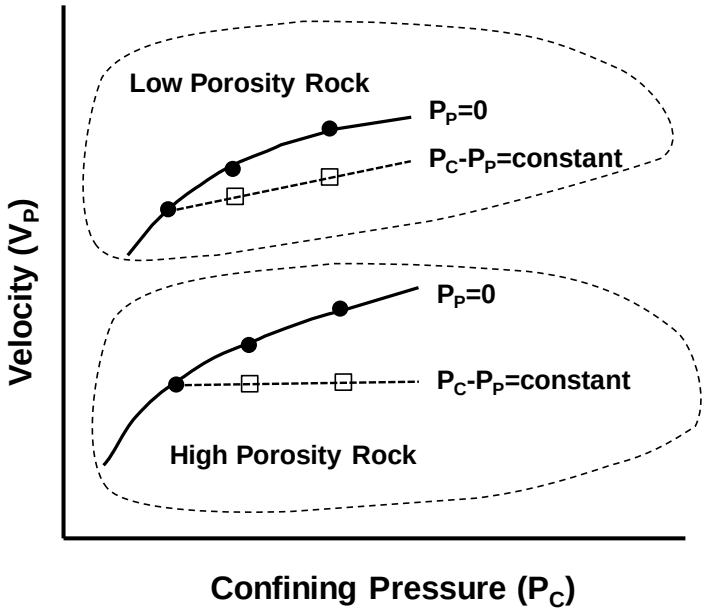

Figure 1-4: Summary of published experiments relating pore pressure to P-wave velocity for rocks with different porosities.

Gardner et al. (1965) studied the pressure dependence of seismic velocity and stated that the seismic velocity is not only dependent on current pressure situation; it also depends on past pressure history. Hysteresis is the main reason accounting for the discrepancy of n. In other words, if the experiment does not follow the hysteresis cycle, the value of n is less than one (Gardner et al., 1965).

1.3 Motivation

Knowledge of pore pressure is crucial in all aspects of exploration and production for oil and gas. If the pore pressure is not appropriately predicted before drilling a kick-out or leakage may occur, which can be quite disastrous. Likewise, if there is abnormal pressure in parts of a region, it will force hydrocarbons to regions of lower pore pressure. Therefore studies of pore pressure are quite important for exploration, drilling, and production. Historically, pore pressure has been predicted from seismic interval velocities by applying an empirical velocity versus pressure transform. The pressure dependence of rock results from the closing of grain boundaries, microcracks, and flaws, which elastically stiffens the rock mineral frame. Increasing pore pressure softens the elastic mineral by opening grain contacts and microcracks, tending to lower velocities. Therefore the effective stress is a primary factor controlling velocity changes (Todd and Simmons, 1972; Eberhardt-Phillips et al., 1989; Gutierrez et al., 2006; Sayers, 2010).

Most velocity to pressure transforms, including the widely-used Eaton's (1975) and Bowers' (1995) methods, are based on the effective-stress principle expressed in equation (1-9). This formula suggests if we know seismic velocity, we can get effective pressure, and then we can predict pore pressure if we know the confining pressure and effective pressure coefficient.

$$V_P=f(P_E)=f(P_C-nP_P)\Rightarrow P_P=(P_C-f(V_P))/n. \quad (1\text{-}9)$$

Surface seismic and well-log sonic data are commonly used to predict pore pressure (e.g. Hottman and Johnson, 1965; Eaton, 1975; Martinez et al., 1991; Bowers, 1995, 2002; Dutta et al., 2002a, b; Dutta, 2002; Huffman, 2002; Sayers et al., 2002; Ebrom et al., 2006; Taylor et al., 2011). In exploration practice the value for n, is often assigned to unity (Sayers, 2010). But as we discussed earlier, as the compaction of rock continues with depth, the porosity of rock decreases, and possibly the value of n equal to one is not applicable for all the depth. Ebrom et al. (2004) has also noted that the assumption that n equals one holds for shallow Gulf of Mexico (GOM) depths with low vertical stress. However, at greater depths as the sediment becomes cemented and more consolidated, this assumption becomes questionable.

As mentioned in Section 1.2, n can be ideally determined through static laboratory measurements. But this n is different than the one obtained from the in-situ dynamic conditions due to different frequencies and strain magnitudes used in laboratory and field. Currently the error resulted from n variation in pore pressure prediction is rarely mentioned. However equation (1-9) reveals the significance of estimating an accurate n if accurate pore pressure predictions are desired.

In this research, we use borehole data at numerous well locations to calibrate the variation of n in different pressure regimes. By examining the density and velocity trends in two different pressure regimes in the GOM, we establish an alternate method to predict pore pressure. Within this scope we establish a different overburden pressure model for

different pressure regimes. We compute the effective pressure coefficient and discuss its importance for pore pressure prediction. Finally we propose an alternate way to obtain effective pressure coefficient by inverting dry rock bulk modulus from Gassmann's equation in a wildcat area without offset wells to do the calibration. Reliable shear wave velocity either from multicomponent seismic data or well-log data is a key issue for this inversion.

2 PORE-PRESSURE EFFECT ON ROCK-PROPERTIES

2.1 Introduction

Pore pressure influences rock properties such as porosity, density, velocity, etc. as discussed in Chapter 1. In this chapter we use statistical methods to check rock property responses in different pressure regimes and discuss the reasons behind them.

2.1.1 Pore pressure terms

Pore pressure (or formation fluid pressure, P_P) is the pressure in the pore space of the formation acting on the fluids which include formation water, oil and gas. When the pore pressure is produced by the weight of the overlying fluid column, or hydrostatic pressure from the surface to the subsurface formation (Gretener, 1976), it is called normal formation pressure. Abnormal formation pressures are those characterized by any departure from the normal hydrostatic trend line. Formation pressures exceeding hydrostatic pressure are defined as surpressures, whereas formation pressures less than hydrostatic pressure are called subpressures (Fertl et al., 1976). Abnormal formation pressures occur worldwide either onshore or offshore with surpressures occurring more often than subpressure (e.g. Fertl et al., 1976; Law and Spencer, 1998; Heppard et al., 1998; Kukla et al., 2011). There are numerous factors associated with abnormal formation pressures such as burial, tectonism, hydrocarbon generation, mineral

transformation, temperature increase, etc. (e.g. Fertl, 1976; Osborne and Swarbrick, 1997; Carcione and Gangi, 2000; Yassir and Addis, 2002; Dugan and Sheahan, 2012). Dugan and Sheahan (2012) summarized the mechanisms and classified them into two general categories: one is physical processes; the other is thermal and chemical processes. Physical processes mainly include rapid sedimentation and fluid migration (Osborne and Swarbrick, 1997). Thermal and chemical processes involve the increased fluid volume in a fixed pore space, which generates overpressure (e.g. Dugan and Sheahan, 2012).

The Gulf of Mexico (GOM) is an ocean basin resulting from rifting within Pangea at a passive margin (Huerta and Harry, 2012). It is bounded by the North American continent on the north and the island of Cuba on the south (Figure 2-1). The areal extent of the GOM basin is approximately 1.6×10^6 km² (http://www.epa.gov/gmpo/about/facts.html). It has a broad continental shelf along Louisiana. It is one of the world's largest oil and gas production basins (Reed et al., 1987). Wells on the GOM continental shelf often encounter abnormal pore pressure (e.g. Dickinson, 1953; Fertl et al., 1976; Martinez et al., 1991). The GOM abnormal pore pressures are reported to be the result of two different physical processes; one is "compaction disequilibrium" and another is called "unloading" and/or clay diagenesis (Bowers, 1995; Verm et al., 1998; Gorden and Flemings, 1998; Hilterman, 2001).

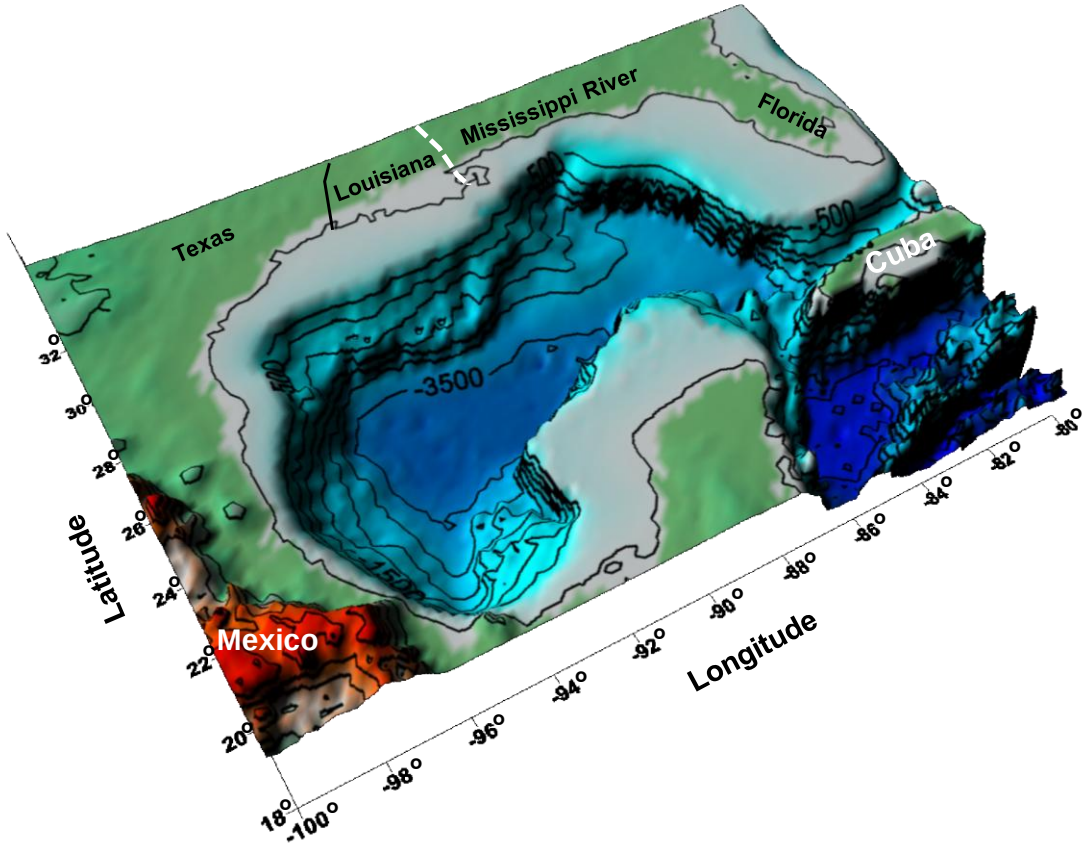

Figure 2-1: Bathymetry map of the Gulf of Mexico (GOM, data is from http://www.ngdc.noaa.gov).

2.1.2 Compaction disequilibrium

When sediments are first deposited, their porosity is determined by factors such as grain size, shape, sorting, and the packing mode of the individual grains. Very fine-grained sediments, such as shale, have a very high porosity and low bulk density because the surface areas of the thin laminae are very large compared to the spacing. A significant amount of fluid (including liquid and gas) is absorbed between the laminae, and grains

are usually very irregular. At the sea floor shale porosity is large, up to 80-90% (Athy, 1930). For coarser sediments like sand, the porosity is usually lower. After additional sediments have been deposited, other factors decrease the porosity such as pressure, fluid diagenesis, recrystallization, secondary growth and cementation, and solution. Of these factors, pressure, either vertical or horizontal, is the primary one affecting porosity. It compacts the grains, resulting in closer spacing, and also expels the interstitial and absorbed water (Athy, 1930).

Compaction, or reduction in volume, is a result of continued application of pressure. As sediments compact, porosity is reduced and density is increased. Sandstone and limestone properties are very variable, so it is difficult to generate a general compaction trend for them (Athy, 1930). However shale has a well-defined compaction trend in a specific locality. The porosity or density change is a direct result of increased pressure. This process is called normal compaction trend (NCT), which produces a stress system in the sediments, where the overburden pressure on a given rock is in equilibrium with the sum of the fluid pressure and the grain pressure within the rock (Smith and Thomas, 1970). Athy (1930) established a porosity-depth trend for shale based on 2200 samples from wells in Oklahoma and Texas.

Athy's normal compaction trend for density is given by

$$D=B+A(1-e^{-bz}), \qquad (2\text{-}1)$$

where D is rock density, B is clay density at the surface, A is maximum possible density

increase, b is an empirically-derived constant, and z is the depth of burial. For porosity Athy (1930) provided a similar equation (2-2) to quantify the normal compaction trend:

$$\phi=\phi_0(e^{-bz}), \quad (2\text{-}2)$$

where ϕ is porosity, ϕ_0 is average porosity at the surface, b is empirically derived coefficient, and z is depth of burial. Swarbrick and Osborne (1998) compiled a series of porosity-depth trends for different lithologies and different basins. A recent review of porosity normal-compaction trends is shown in Figure 2-2 (Mondol et al., 2007).

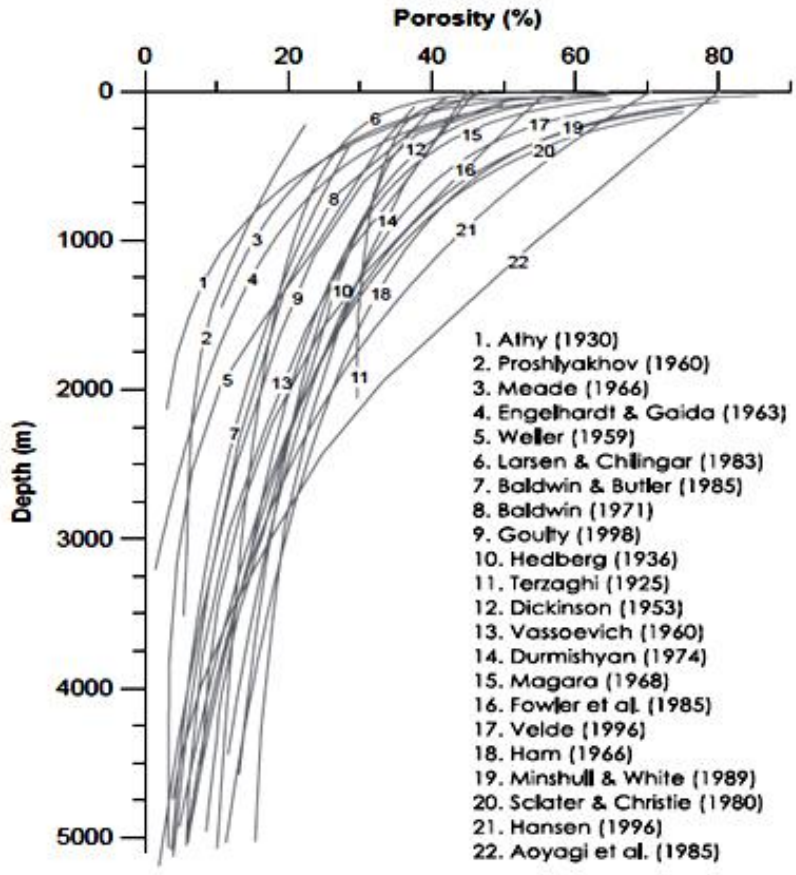

Figure 2-2: Normal compaction curves for shale porosity (Mondol et al., 2007).

A decrease of effective pressure will retard the compaction process. Therefore, the porosity will deflect from the NCT. In essence any measurement that senses porosity including surface seismic or sonic velocities, density and resistivity logs can be a tool to predict overpressure (e.g. Gutierrez et al., 2006). If in a certain geologic setting water is unable to escape from the pore space, the compaction process is retarded. With burial, the pore fluids start to support the extra load exerted by additional overburden pressure, which then generates abnormal high pore pressure, but the effective pressure is constant. In those zones, shale has an anomalously high porosity and low density which are lower than they would be under normal compaction at the same depth. This process is referred to as compaction disequilibrium or undercompaction (Leftwich and Engelder, 1998; Bruce and Bowers, 2002). It is reported as the most common mechanism for abnormally high pressure in petroleum provinces in young (Tertiary) deltaic sequences (Law and Spencer, 1998). Undercompaction typically generates a large overpressure at shallow depths because the rock matrix at shallow depths is relative soft and much more compressible than pore fluid; thus, increases in overburden pressure will be carried primarily by the pore fluid (Bowers, 1995).

2.1.3 Unloading/clay diagenesis

Unloading is a mechanical term, which means release or decrease of effective pressure due to the removal of overburden pressure (i.e. erosion, ice melting) and/or increase of pore pressure resulting from fluid expansion (Bowers, 1995). The volume expansion of

fluids has been reported to be caused by thermal expansion (e.g. Barker, 1972; Bethke, 1986; Mello et al., 1996; Osborne and Swarbrick, 1997), hydrocarbon generation (e.g. Luo and Vasseur, 1996; Gordon and Flemings, 1998; Lupa and Flemings, 2002) and expulsion of intergranual water during clay diagenesis (Colton-Bradley, 1987; Pollastro, 1993). If the produced extra fluids are not freely drained from the pore space, overpressure is generated. This process is called unloading because the effective pressure decreases (Bowers, 1995; Bruce and Bowers, 2002). The smectite-to-illite transformation has been reported as the major clay diagenesis process to cause abnormal formation pressure in GOM (e.g. Bruce, 1984; Freed and Peacor, 1989). Colton-Bradley (1987) found this process releases bound water at temperatures over 70 °C. As smectite transforms into illite, the illite packets coalesce and form very efficient seals, which promotes the magnitude of overpressure (Freed and Peacor, 1989). However there is still a debate if this process is elastic unloading or inelastic unloading (Katahara, 2006; Lahann and Swarbrick, 2011).

2.1.4 Distribution of different pressure regimes

For the undercompaction process, abnormal pore pressure builds up and mud weight increases gradually when overpressure is encountered. However, the pore pressure increase for unloading systems usually occurs abruptly. At the onset of unloading, the mud weight has to be significantly increased. In drilling practice, undercompaction is often referred to as a ‘soft’ onset of geopressure (GP) and unloading as a ‘hard’ onset of

GP (Hilterman, 2001). The term geopressure is synonymous with abnormal pore pressure. Verm et al. (1998) examined over 2500 wells in offshore Louisiana and revealed the relationship between the onset depth of geopressure and sand percentage. They further outlined the boundary between the hard onset and soft onset pressure regimes (Figure 2-3).

(a)

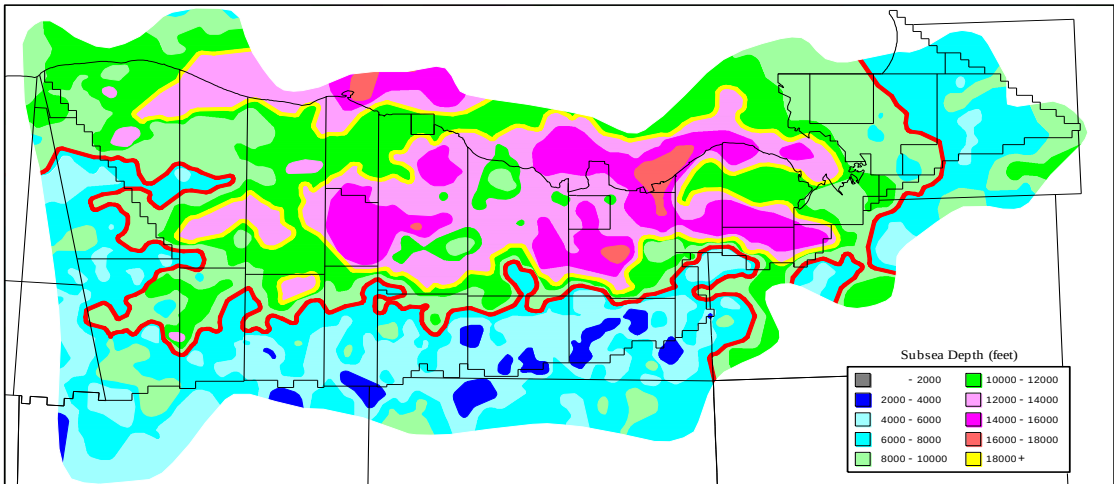

(b)

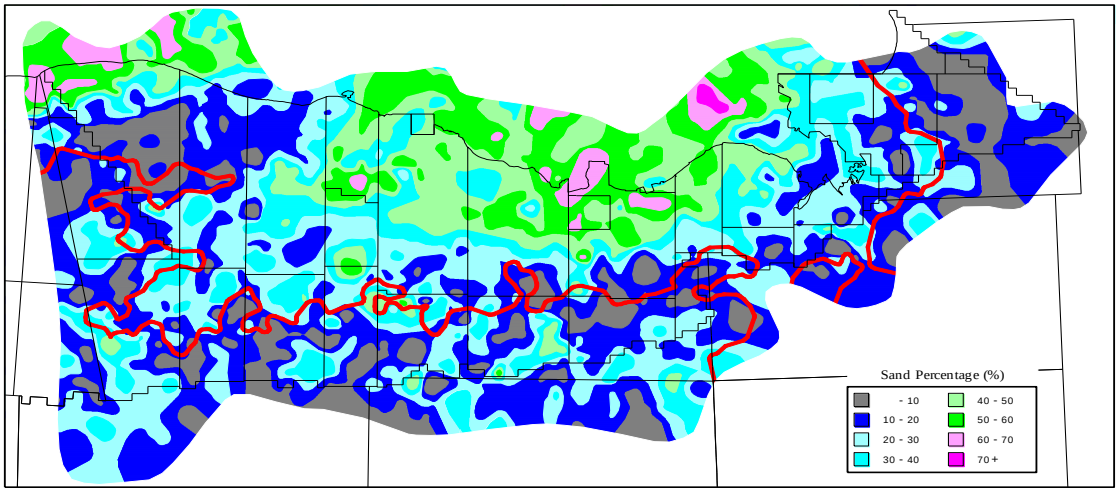

Figure 2-3: Onset depth of geopressure (a) and corresponding sand percentage distribution (b) at depth interval of 7000-8000 ft (2000-2500 m) (Verm et al., 1998). The red line is the 8000 ft (2500 m) contour line for the onset depth of geopressure.

In the offshore areas of South Marsh Island and Eugene Island, the impact of geopressure to shale properties are examined. We further divide the whole area into six tracts (Figure 2-4b) to isolate changing rock properties. Previous research has shown in the southern areas of the Louisiana shelf, the shale P-wave velocity increases approximately linearly with depth until the onset of geopressure. Below the onset, shale velocity and density values tend to be constant at the same value as those at the onset (Yu et al., 2011). This mechanism for geopressure is disequilibrium compaction or undercompaction, where shale stops dewatering due to rapid sedimentation. The weight of the drilling mud is gradually increased through the onset of geopressure (Figure 2-5b). In the northern part, the P-wave velocity also increases approximately linearly until the onset of geopressure and then the velocity abruptly decreases, while the density trend is usually not affected (Figure 2-5a, Yu et al., 2011). This sharp transition is called unloading and the mechanism is often thought to be a diagenetic fluid expansion following shale dewatering. Mud weight must be increased significantly through this onset of abnormal pressure. In short, two different physical processes take place in our study area. We want to develop a systematic strategy for pore pressure prediction in both of these pressure processes.

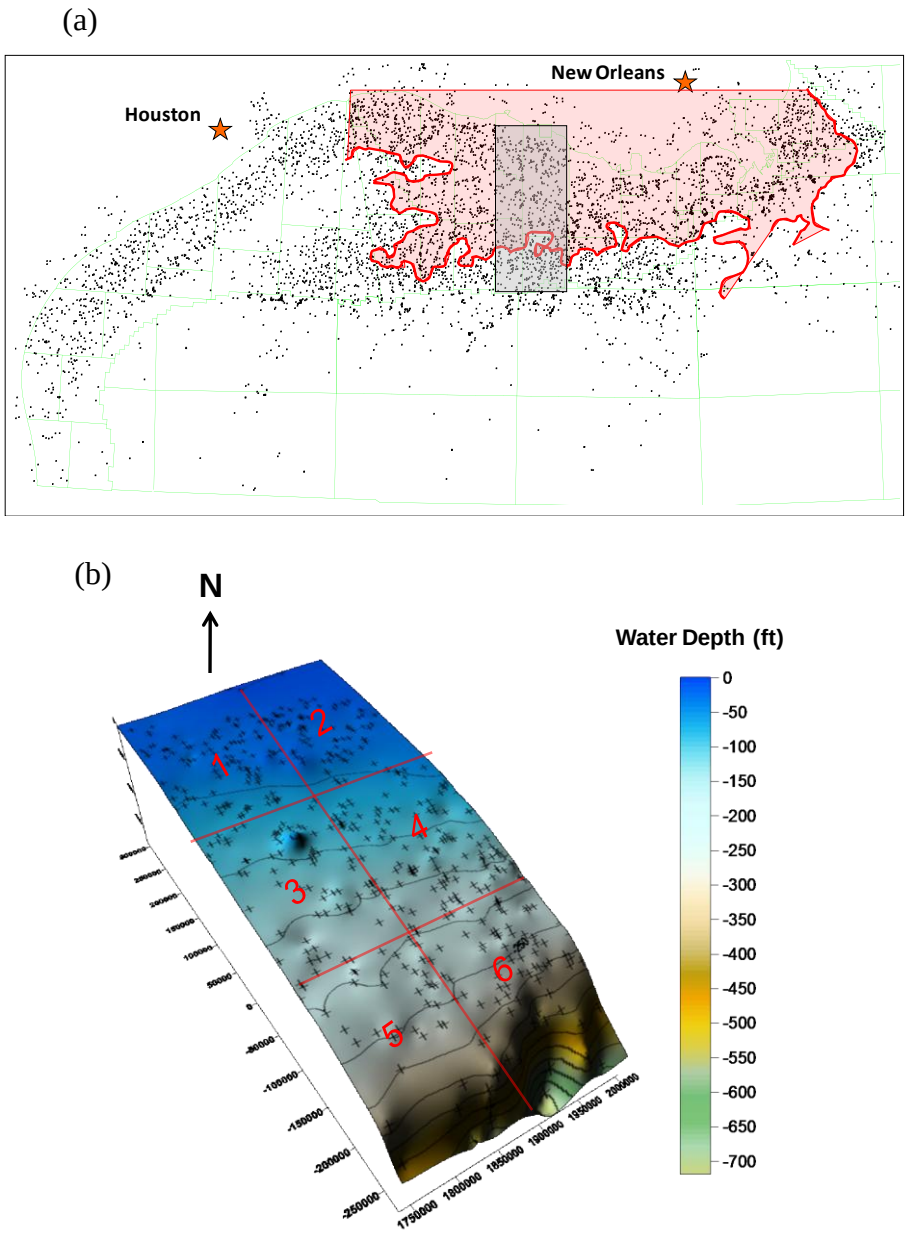

Figure 2-4: Bathymetry map of study area (gray shaded area in (a)) with well locations (b). The red line is the boundary between hard onset and soft onset of geopressure (modified from Verm et al., 1998). Cross symbols in (b) represent well locations.

(a) (b)

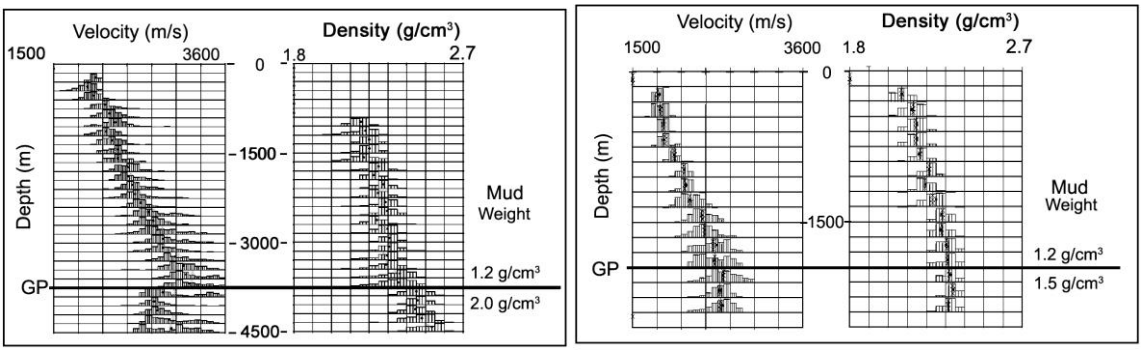

Figure 2-5: Density and velocity trends for single wells in the northern (a) and southern (b) areas (Hilterman, 2001).

2.2 Methods

In this study, rock-property catalogs for shale are developed from over 480 wells in the study area. As the northern and southern areas have different overpressure mechanisms, it is necessary to study the density and velocity trends for these two processes separately. We further split the area into 6 tracks to better isolate the influence of data bias and variations in rock properties. The distribution of wells in the six tracts is given in Table 2-1. Tracks 3 and 4 are in the transitional area between hard and soft onset of geopressure.

In our data sets, we define sand as sediment with a shale volume less than 50%; and shale, greater than 50%. Mean and standard deviation values for the rock properties of sand and shale over 60 m (200 ft) intervals are created for each well. Ancillary information, such

as mud weight, sand percentage and temperature are also included in each 60 m interval. The statistics, starting from ocean-bottom datum, include P-wave velocity, density, and resistivity properties for both sand and shale. Statistics from over 20,000 60 m intervals are available for this study, and the distribution between the six tracks is shown in Table 2-1. The onset of geopressure is estimated for each well based on resistivity, sonic and density gradient changes, mud weight and sufficient shale thickness at the onset of geopressure. Intervals with questionable logging quality are omitted along with hydrocarbon intervals. As geopressure is usually build up in low permeability shale, we focus our discussion on shale properties.

In addition to the petrophysicist's pick for the onset of abnormal pressure, the normal and abnormal depth intervals are also identified by mud weight. Depth intervals with mud weight less than 12 lb/gal are defined as intervals above geopressure and intervals with mud weight more than 12 lb/gal as below geopressure. As a mechanism to guard against statistical outliers, we further constrain each depth interval to have at least 10 wells before a statistic for the depth trends is accepted. Normally, the density log is unreliable at shallow depths, thus, density trends start below 1000 m.

Temperatures are determined by linear interpolation of the bottomhole temperature between logging runs. Mud weights are likewsie interpolated. No high-quality Repeated Formation Test (RFT) pressure data are available, so the pore pressure is estimated from the mud weights.

Table 2-1: Area statistics of well locations and 60 m rock-property intervals.

Tract	No. Wells	No. Intervals
1	74	3517
2	110	5640
3	47	2200
4	82	4460
5	48	2219
6	126	5781
total	487	23817

2.3 Results

2.3.1 Density trends of shale

Shale density statistics for the six tracts of the study area are displayed in Figure 2-6. There are three depth panels displayed for each tract. The red annotations relate to statistical values in normal pressure; and blue, abnormal pressure. Besides the density trend in the left panel of each tract plot, the number of wells entering into the statistics is plotted in the middle panel and the mud weight in the right panel. In addition, the standard deviations are plotted around the mean values for density and mud weight. Best

fit mathematical trends are overplotted on the density trends for normal and abnormal pressure.

The shale density depth trends are different between the northern and southern areas. In the northern part of the study area, which includes Tracts 1 to 4, the density exponentially increases with depth (Figure 2-6); although the exponentiation is near a linear trend for the depth intervals displayed. This trend appears to be continuous even in the translation from normal to abnormal pressure regimes. This means within overpressure zone, the density keeps increasing with depth. However in the southern area, the density trends in geopressure are different from the northern 4 tracts. The density values in the geopressure zone remain the same or are "frozen" at the same value as that at the onset of geopressure. This process will be better illustrated later when sub-zones of a tract are analyzed. The density response in different tracts corresponds to different pressure regimes. In the north area overpressure is believed mainly caused by smectite to illite transition. Illite has a higher density than smectite (Grim, 1953), so even though more mobile water is released from the intergranular structure of smectite, the changed matrix keeps the density high. While in the southern area, disequilibrium compaction is the major reason for geopressure. There sediment section is sand poor with too much shale. Water doesn't have chance to escape from the pore space, so compaction of shale stops in abnormal pressure zone, and the density 'freezes'.

In order to quantify the different trends in study area, from Tracts 1 to 4, we fit Athy (1930) type equations to the trends both above and below geopressure. For above geopressure in Tracts 5 and 6, we fit Athy (1930) type equation (2-3) and below geopressure we fit a linear trend (equation (2-4)) to represent the 'freezing' of density in the geopressure zone.

$$\rho(z) = \rho_0 - ae^{-bz} . \tag{2-3}$$

$$\rho(z) = \rho_0 + cz . \tag{2-4}$$

ρ (z) is the bulk density in g/cm^3, ρ_0 is the possible minimum density in g/cm^3, a, b and c are coefficients, and z is depth in meters. We use a least-squares curve fitting method to get the best parameters for equations (2-3) and (2-4). Those parameters are listed in Table 2-2. The RMS (root-mean-square) errors, Δ, between predicted and measured density are also show in Table 2-2.

$$\Delta = \sqrt{\frac{\sum_{1}^{n}(\rho_{predicted} - \rho_{measured})^2}{n}} , \tag{2-5}$$

where $\rho_{Predicted}$ is predicted density from equation (2-3) and equation (2-4); $\rho_{measured}$ is density from database; and n is the number of 60 m intervals.

Table 2-2: Least-squares coefficients and RMS errors for shale density trends above and below geopressure.

	Above geopressure				Below geopressure				
Tract	ρ_0 (g/cm^3)	a (g/cm^3)	b (1/m)	Δ (g/cm^3)	ρ_0 (g/cm^3)	a (g/cm^3)	b (1/m)	c (1/m)	Δ (g/cm^3)
1	2.60	0.60	2.63×10^{-4}	0.01	5.78	3.65	1.86×10^{-5}	/	0.02
2	3.05	1.02	1.07×10^{-4}	0.01	2.48	0.38	3.59×10^{-4}	/	0.01
3	2.56	0.67	3.46×10^{-4}	0.02	4.53	2.41	3.06×10^{-5}	/	0.02
4	3.08	1.00	9.49×10^{-5}	0.01	2.47	1.46	8.62×10^{-4}	/	0.01
5	2.31	0.62	1.30×10^{-3}	0.01	2.18	/	/	3.03×10^{-5}	0.02
6	3.10	1.02	1.02×10^{-4}	0.01	2.14	/	/	4.73×10^{-5}	0.01

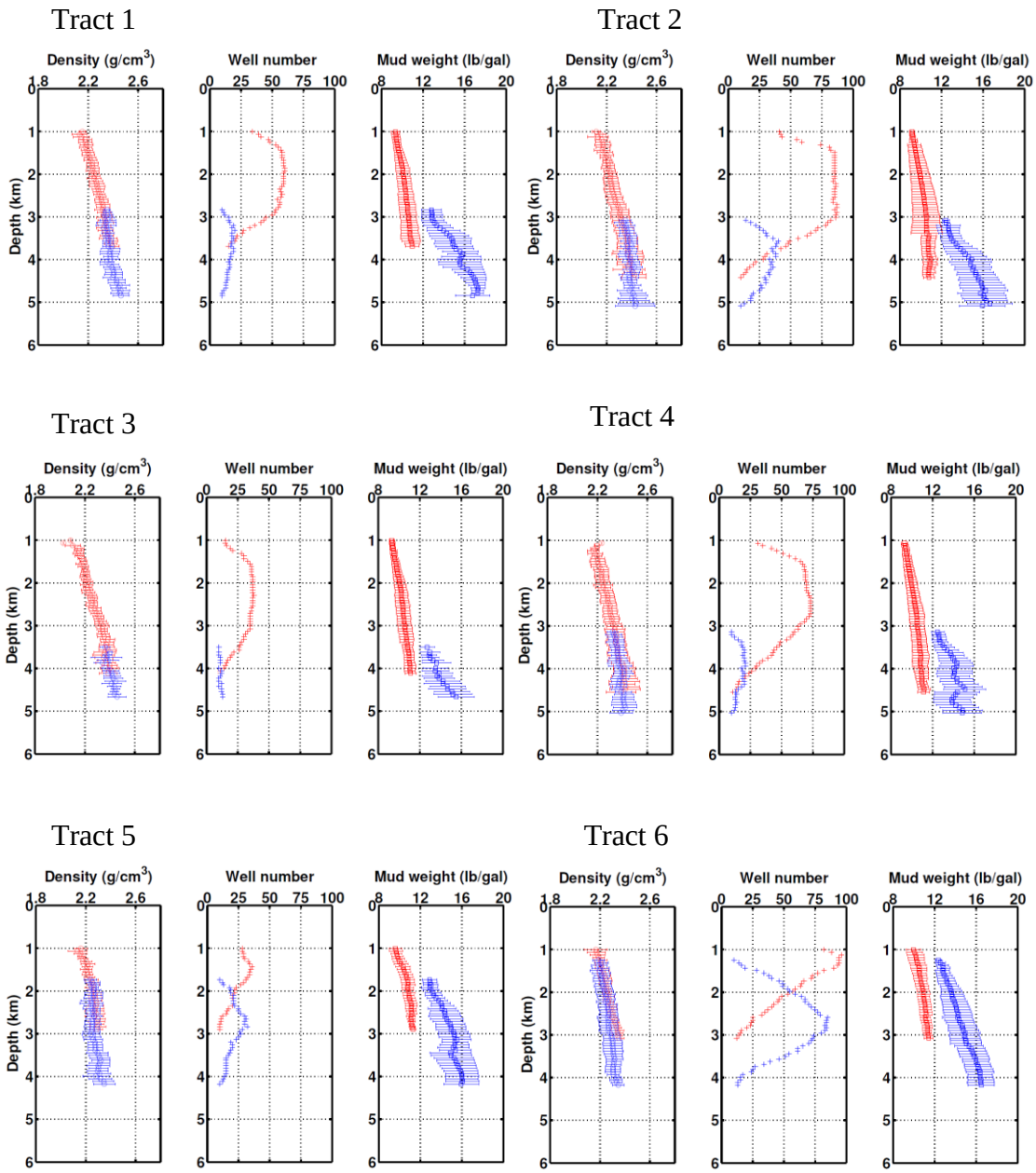

Figure 2-6: Mean shale density (open circle) and mud weight (open square) with standard deviation (horizontal bar) for above (red) and below (blue) onset of geopressure for Tracts 1 to 6.

In order to visualize the density variations in the different pressure regimes, all trends are over plotted in Figure 2-7. Above geopressure the density trends in all 6 tracts are quite similar, while below geopressure the density trends in Tracts 5 and 6 are quite different from other tracts. This difference will be described later when the statistics for Tracts 1 and 6 are subdivided.

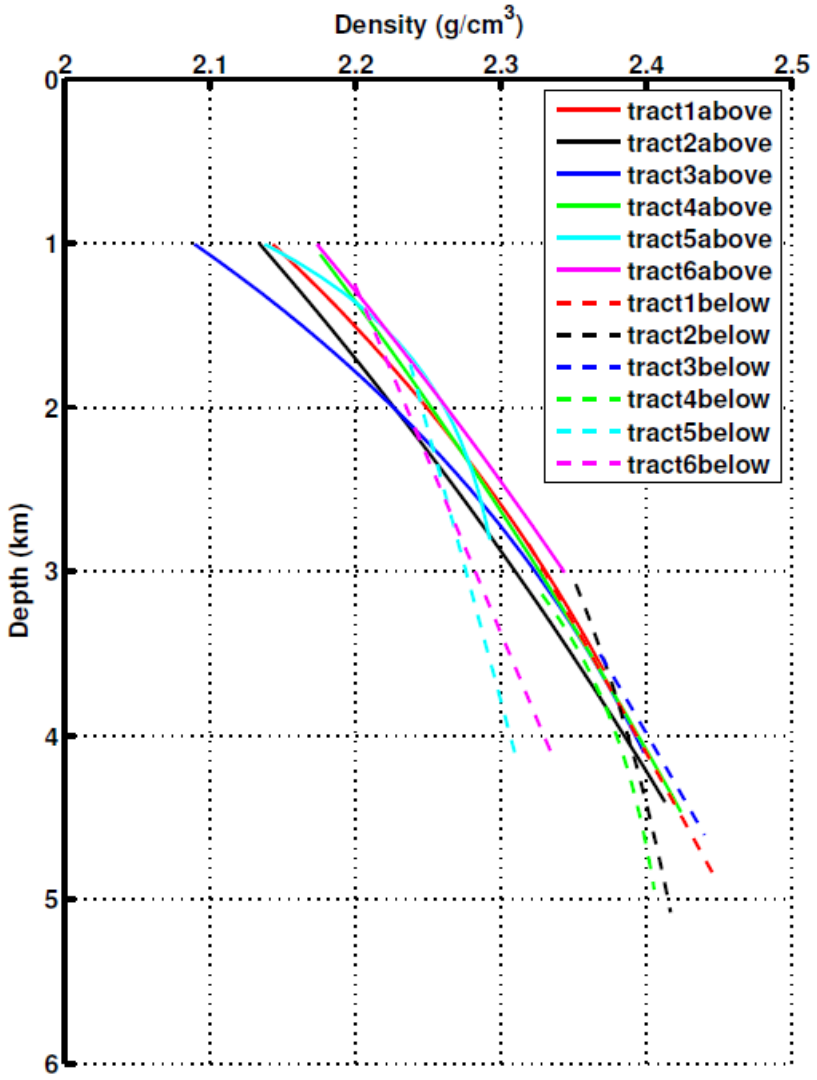

Figure 2-7: Shale density trends for above and below onset of geopressure for Tracts 1 to 6.

2. 3. 2 Velocity trends of shale

Similar to density, we establish the velocity trends for the six tracts. For each tract there are two different trends, above and below geopressure (Figure 2-8). Above geopressure, the P-wave velocity linearly increases with depth. But from the start of the onset of geopressure, the velocity freezes. In Tracts 1 and 2 the V_P below geopressure even slightly pulls back. Two different linear trends are fitted for above and below geopressure for six tracts as

$$v = v_0 + az. \tag{2-6}$$

The empirically derived parameters are listed in Table 2-3. The RMS errors, Δ, between predicted and measured velocity are also show in Table 2-3.

$$\Delta = \sqrt{\frac{\sum_{1}^{n}(V_{predicted} - V_{measured})^2}{n}}\ , \tag{2-7}$$

where $V_{Predicted}$ is predicted velocity from equation (2-6); $V_{measured}$ is velocity in database; and n is the number of data samples.

Table 2-3: Least-squares coefficients and RMS errors for shale velocity trends above and below geopressure.

	Above Geopressure			Below Geopressure		
Tract	V_0 (m/s)	a (1/s)	Δ (m/s)	V_0 (m/s)	a (1/s)	Δ (m/s)
1	1798	0.40	37.33	3302	-0.12	60.19
2	1765	0.42	30.61	3153	-0.01	45.59
3	1760	0.41	23.54	2979	0.07	46.07
4	1757	0.40	28.46	2258	0.22	88.10
5	1760	0.42	53.21	2222	0.12	78.68
6	1776	0.41	47.55	2208	0.11	31.49

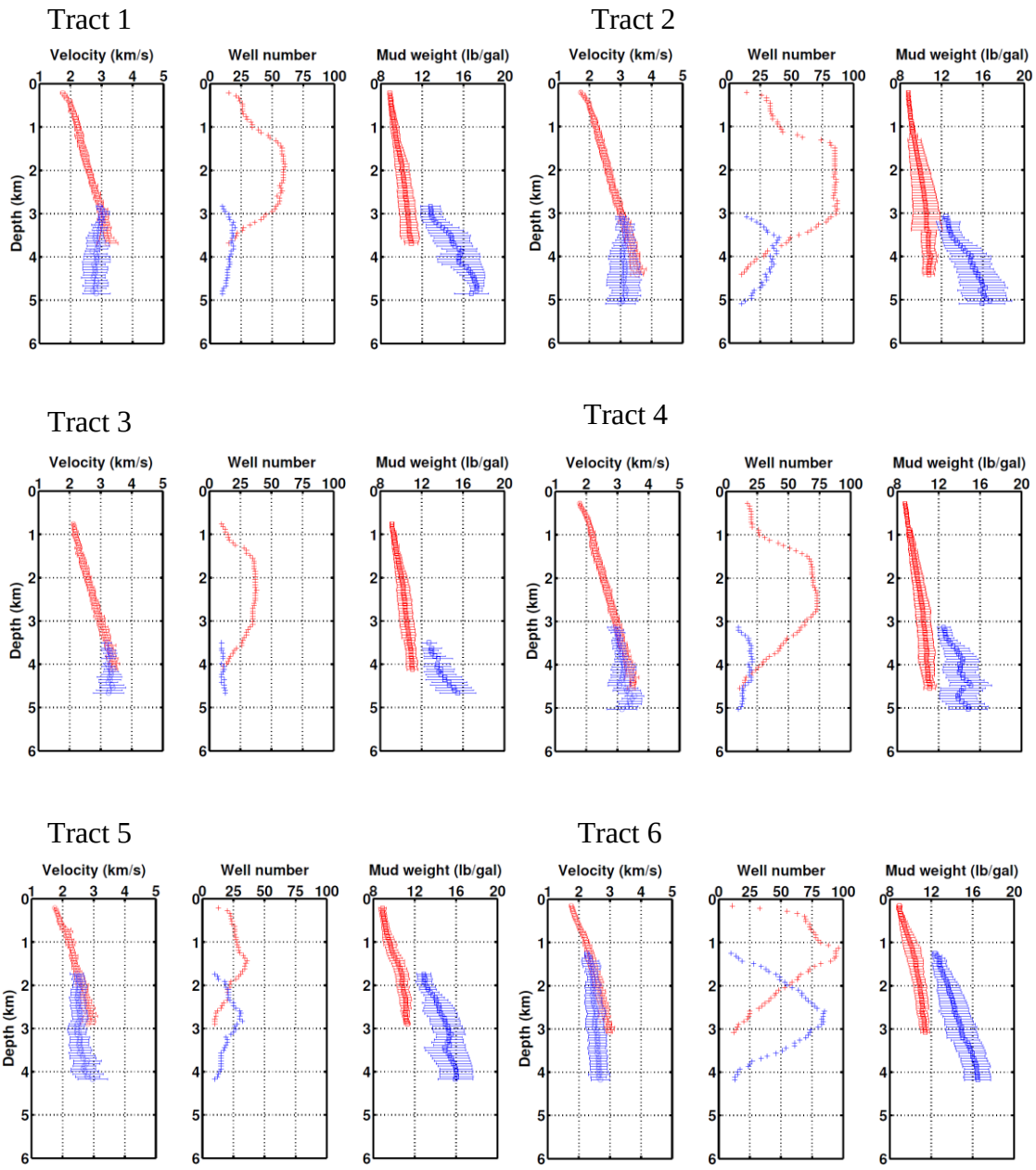

Figure 2-8: Mean shale velocity (open circle) and mud weight (open square) with standard deviation (horizontal bar) for above (red) and below (blue) onset of geopressure for Tracts 1 to 6.

In order to get an overall view of velocity trends in the whole study area we overlapped all 12 trend lines. In Figure 2-9, a consistent trend above geopressure obviously exists, which is defined as an original normal compaction trend (NCT). However below geopressure there are three types of trends. For Tracts 1 and 2, the gradient is a negative linear trend, which suggests the velocity decreases with depth in the geopressure zones. For Tracts 3 and 4 velocities slightly increase with depth. For Tracts 5 and 6 velocity increases at a very small gradient. The transition of velocity trends for each tract indicates that the onset of geopressure starts at a much deeper depth in the northern area, around 3000 m, than that of southern area, 1500 m.

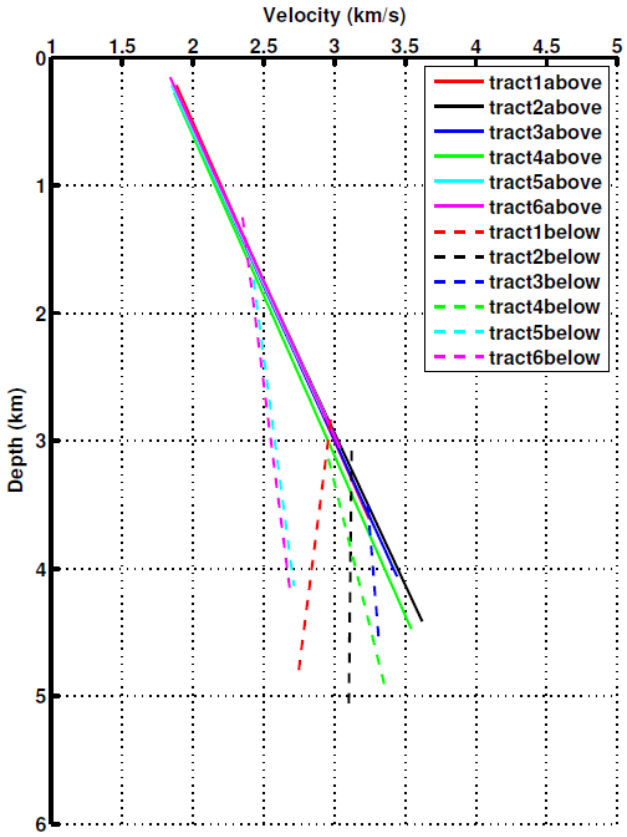

Figure 2-9: Shale velocity trends for above and below onset of geopressure for Tracts 1 to 6.

2.3.3 Density and velocity trends in tract subdivisions

The previous section implied that the density and velocity trends are different in the northern area, Tracts 1 to 4 from the southern area, Tracts 5 and 6. For the undercompaction mechanism, the density and velocity trends are anticipated to be near vertical lines in the abnormal pressure zone in the southern area. But in Figures 2-6 and 2-8, the density and velocity increase slightly with depth for Tracts 5 and 6. This is actually an artifact resulting from the averaging method used to generate the statistics. In previous trend analyses a mud weight of 12 lb/gal was the threshold to delimit normal and abnormal pressure zone; then all the data points in normal pressure are averaged for each particular depth interval, and the same is done for those data points in abnormal pressure. But in fact, the onset of abnormal pressure is not at a distinct depth for all the wells in the southern tracts, but spreads over a depth range of 1200-4200 m as is illustrated for Tract 6 in Figure 2-10. This means if the density and velocity values within a 60 m depth interval are averaged over all the wells, then wells with different onsets of abnormal pressure will be averaging different density or velocity values that are associated with pressure onset. The trends in Figures 2-6 and 2-8 are influenced by data smear. In order to get more realistic density and velocity trends in geopressure, the wells are sorted based on the onset of the GP depth, which was determined when the wells were initially initiated and edited. More realistic density and velocity statistics are calculated, especially for the southern area.

Tracts 1 and 6 are selected for this analysis as they represent two extreme cases: unloading and undercompaction. Additionally both tracts contain enough wells to obtain reliable statistical results (Table 2-1). As mentioned, the onset depth of GP for each well is determined based on resistivity, sonic and density gradient changes, mud weight and sufficient shale thickness at the onset of GP. Tracts 1 and 6 have very different distribution patterns for onset depth of GP (Figure 2-10). In Tract 1 most of the wells step into abnormal pressure zone approximately 3000 m, while in Tract 6 the onset GP depth has a wide distribution. Many wells start GP at 1500 m, followed by 2000 m, 2500 m, and 3000 m. In order to obtain more accurate density and velocity trends, all the wells are separated into eleven different depth zones for Tracts 1 and 6 based on their onset depth of GP which ranges from 1.2 km to 4.5 km. The start and end depths of each onset GP zone, and number of wells in that specific zone are listed in Table 2-4. We focused the statistical analyses on zones that have more than 3 wells (bold numbers in Table 2-4) in order to obtain more reliable results. Then data points in each specific 60 m depth interval are averaged regardless of their mud weight values. But in order to compare the mud weight profile with the onset depth of GP, the average mud weight for each 60 m depth interval was also computed.

Tract 1

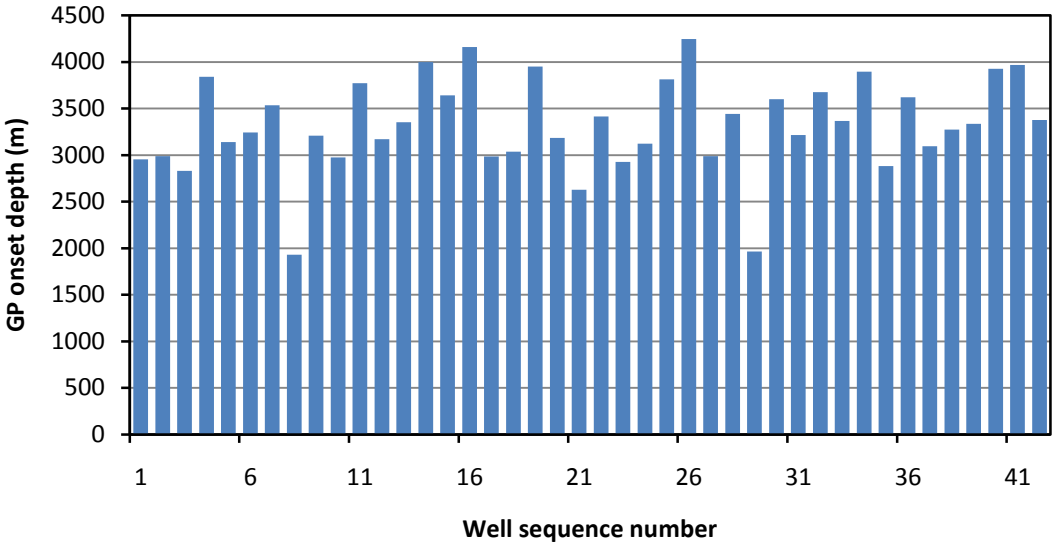

Tract 6

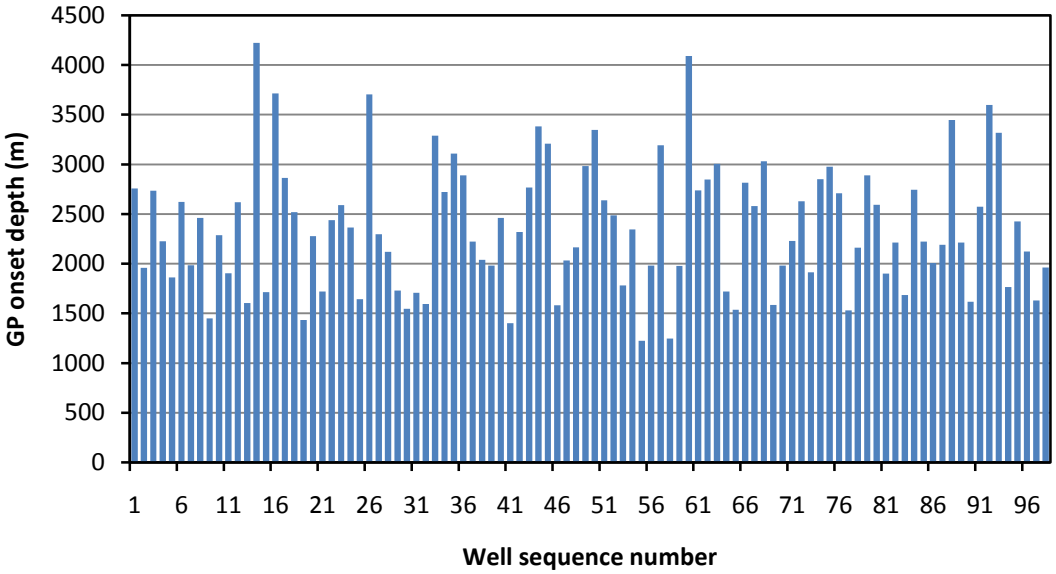

Figure 2-10: Histograms of onset depth of GP for Tracts 1 and 6.

Table 2-4: List of onset of GP zones in Tracts 1 and 6. Bold numbers in the last two columns represent the zones which have more than 3 wells.

Zone	Onset of GP (km)	No. Wells	
		Tract 1	Tract 6
A	1.2-1.5	0	**5**
B	1.5-1.8	0	**18**
C	1.8-2.1	2	**14**
D	2.1-2.4	0	**17**
E	2.4-2.7	1	**14**
F	2.7-3.0	**8**	**15**
G	3.0-3.3	**10**	**6**
H	3.3-3.6	**8**	**5**
I	3.6-3.9	**7**	2
J	3.9-4.2	**5**	1
K	4.2-4.5	1	1

The shale density depth statistics for Tracts 1 and 6 with different GP onset depth ranges are shown in Figures 2-11 and 2-12 respectively. Purple squares represent the depth of GP onset for each zone. For Tract 1, wells encounter GP at deeper depths than the wells in Tract 6. The density and velocity depth trends start at 2.7-3.0 km (Table 2-4 and Figure 2-11). A similar density trends are observed when comparing Figure 2-11 to Figure 2-6 for Tract 1; that is, the density trends are continuous going from normal to abnormal pressure.

Comparatively in Tract 6, wells encounter GP at shallower depths than wells in Tract 1. The statistical analyses start at 1.2 km (Figure 2-12). The most outstanding feature in Figure 2-12 is that a straight density trend (nearly vertical) exists in the abnormal pressure zones. In other words, density stops increasing beyond the onset depth of GP as expected for an undercompation mechanism. This effect of geopressure on density should be taken into account when an accurate overburden pressure model is desired for pore pressure prediction in the southern area.

In order to appreciate the variation of density at different onsets of GP, data from the 8 zones in Tract 6 are over plotted in Figure 2-13. The density trends have a consistent normal compaction trend in normal pressure except for the large scattering at shallow depths from ocean bottom to 1000 m (Figure 2-13 (a)). The density trends are relatively straight lines below GP for all 8 zones. But the start point of each straight line is different, which corresponds to different onsets of GP (Figure 2-13 (b)).

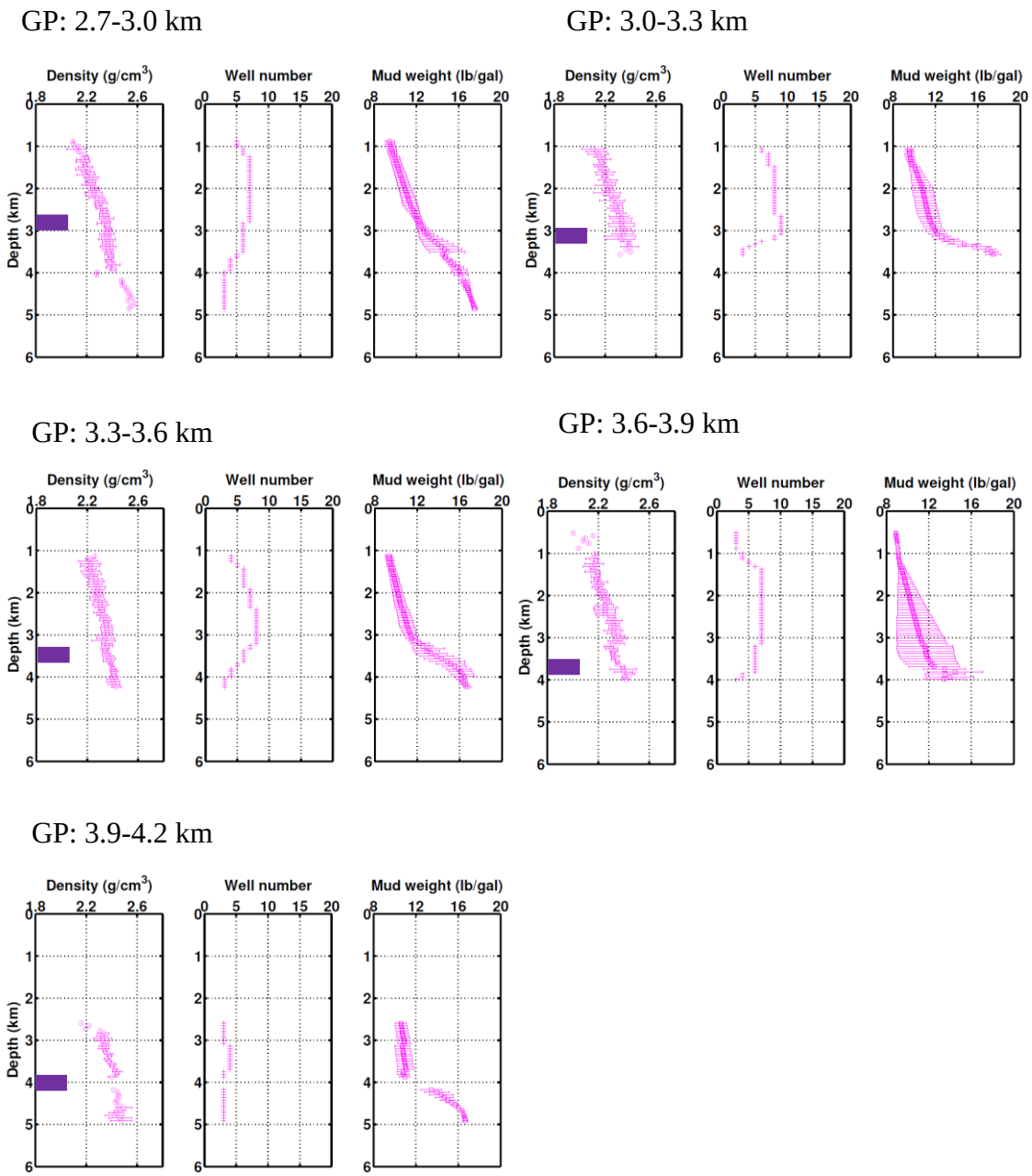

Figure 2-11: Mean shale density (open circle) and mud weight (open square) with standard deviation (horizontal bar) in Tract 1.

GP: 1.2-1.5 km

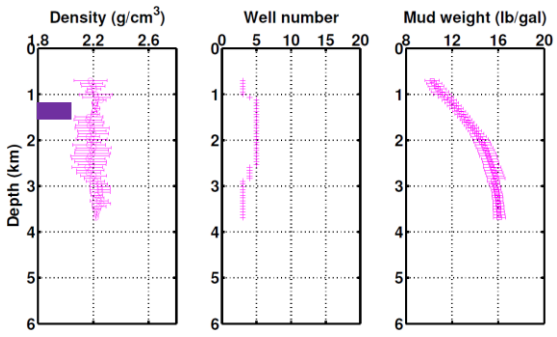

GP: 1.5-1.8 km

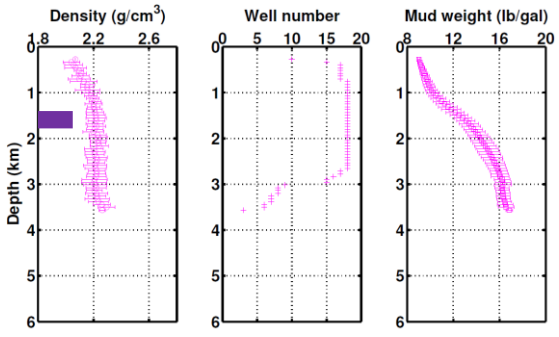

GP: 1.8-2.1 km

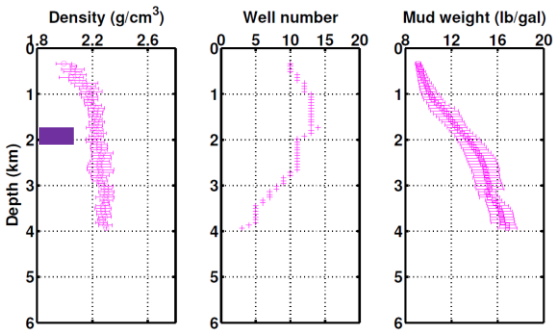

GP: 2.1-2.4 km

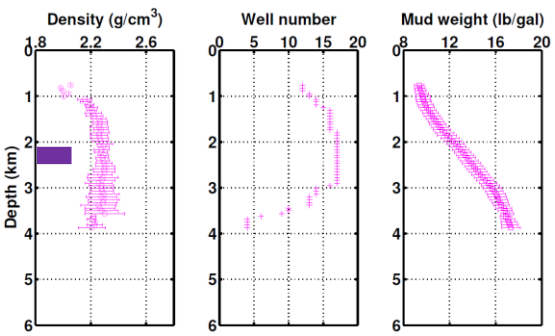

Figure 2-12: Mean shale density (open circle) and mud weight (open square) with standard deviation (horizontal bar) in Tract 6.

GP: 2.4-2.7 km

GP: 2.7-3.0 km

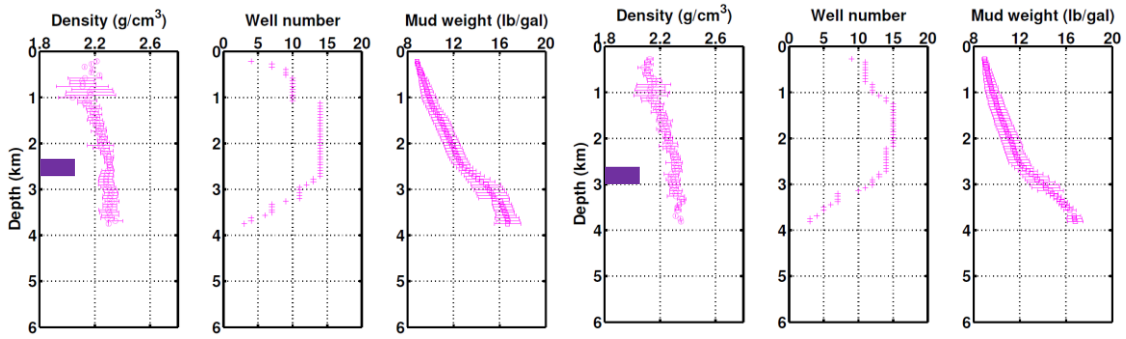

GP: 3.0-3.3 km

GP: 3.3-3.6 km

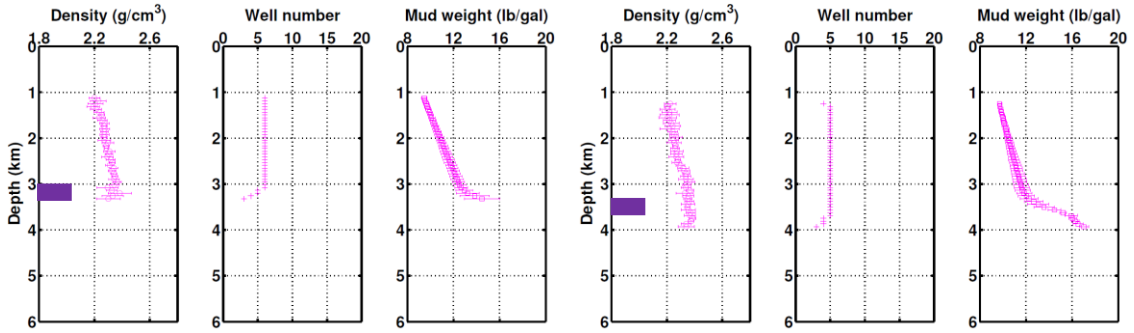

Figure 2-12: (continued) Mean shale density (open circle) and mud weight (open square) with standard deviation (horizontal bar) in Tract 6.

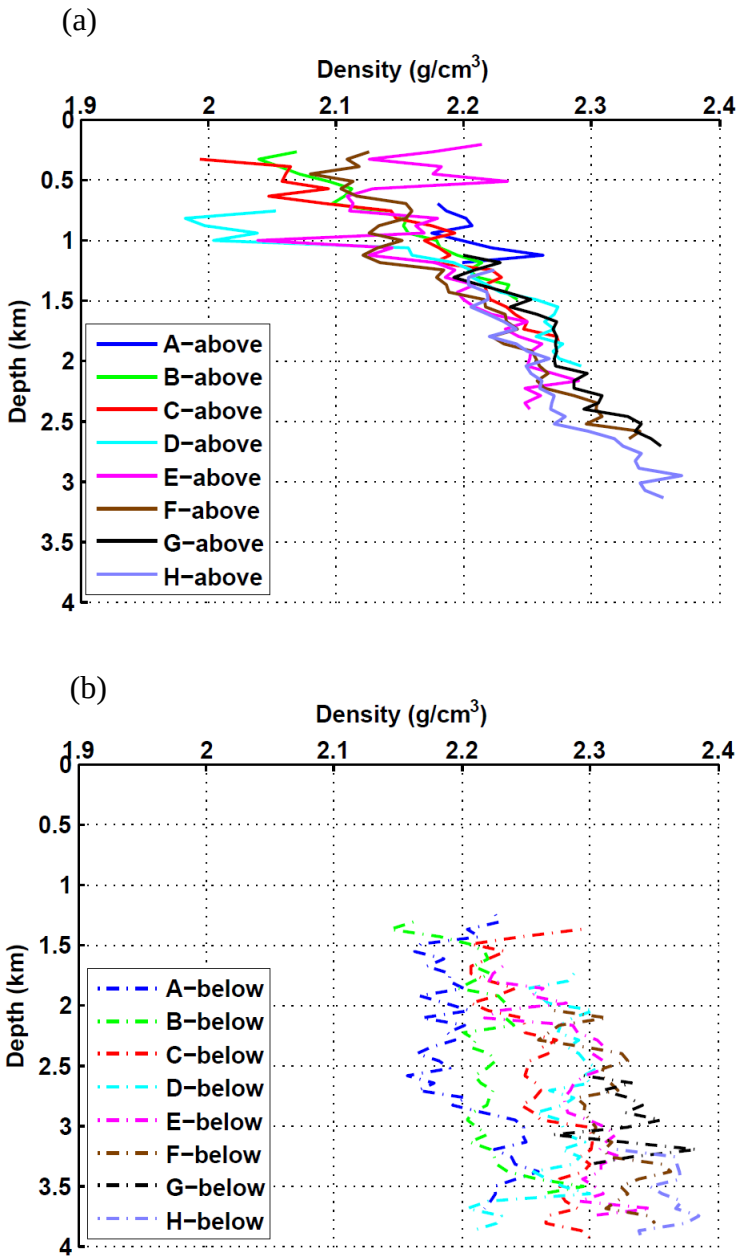

Figure 2-13: Density comparison among A-H zones in Tract 6; (a) is above GP and (b) is below GP.

A strong correlation exists between the onset depth of GP and the density freeze point (Figure 2-14 (b)). In order to quantify this relationship, the freeze density at each onset of GP depth are compiled and plotted in Figure 2-14. For pore pressure prediction in an area where undercompaction is the dominant mechanism for abnormal pressure, it is important to find the density at the onset of geopressure since below this point the rock density is essentially constant. This density can be predicted from the normal density trend.

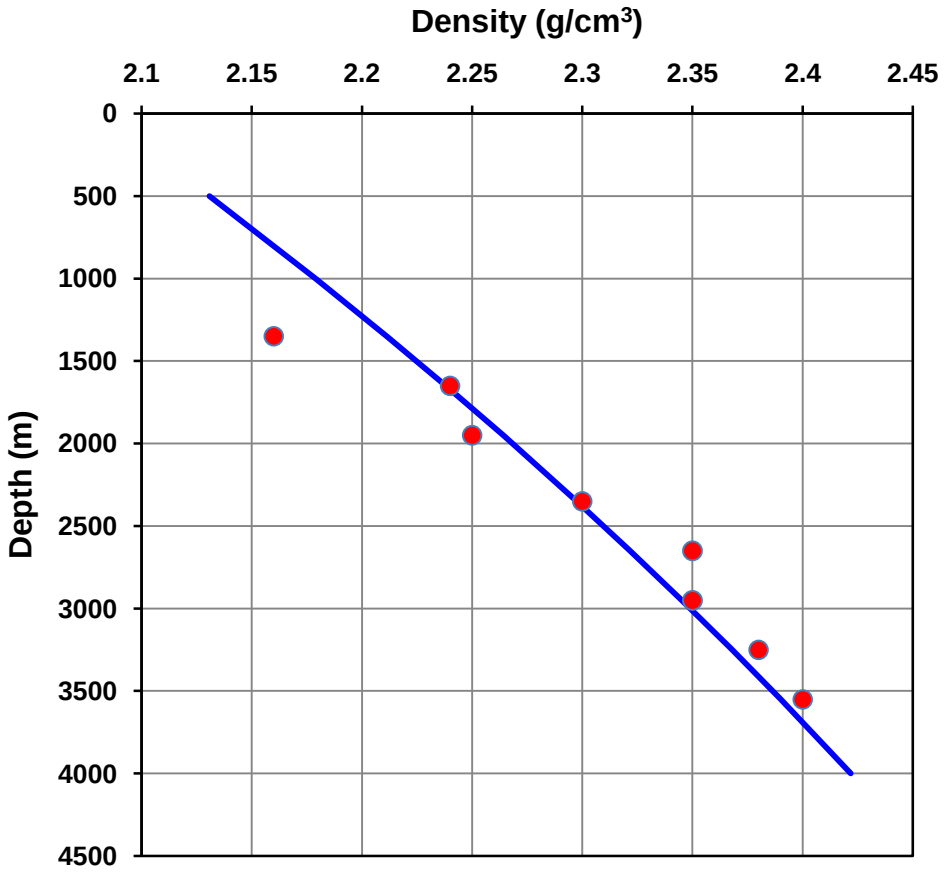

Figure 2-14: Relationship between the 'freezing' density and onset of GP depth for Tract 6. The blue line is the predicted density from normal pressure zone which is defined in section 2.3.1. It is computed from equation (2-3) with coefficient taken for Tract 6 in Table 2-2.

Velocity statistics for different GP zones in Tracts 1 and 6 are shown in Figures 2-15 and 2-16. In Tract 1 the pull back of velocity at the onset of abnormal pressure is obvious (Figure 2-15). While in Tract 6 below GP the velocity is also a straight line like density (Figure 2-16) but with a slight pull back at GP onset. In order to compare the normal compaction trend and freeze of velocity at different onset depths of GP in the southern area, all eight trends from Tract 6 are plotted in Figure 2-17. It shows the similar pattern as density in Figure 2-13. That is above GP velocity linearly increases tracing the NCT (Figure 2-17 (a)), while below GP velocity varies very slightly after the freeze point.

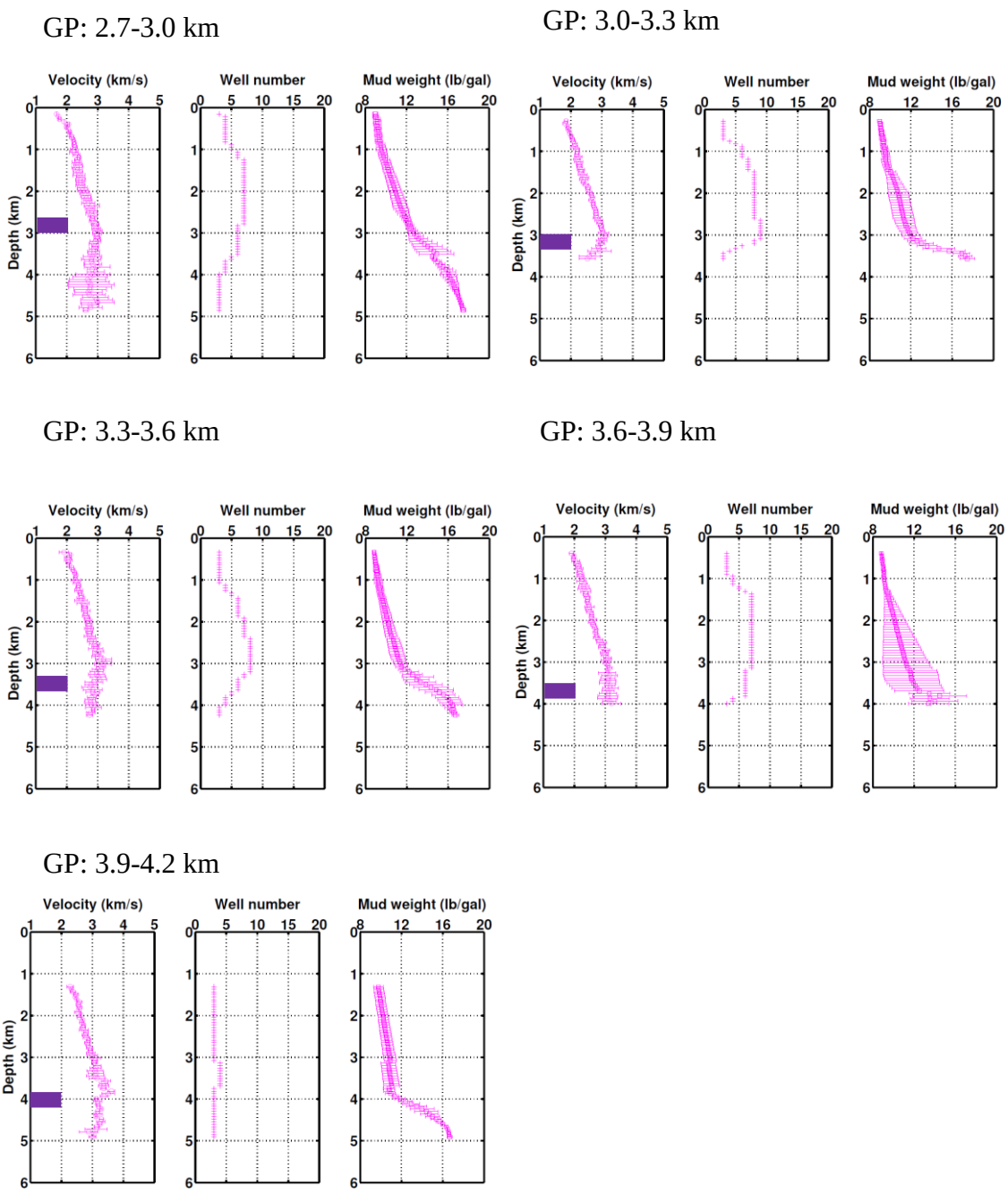

Figure 2-15: Mean shale velocity (open circle) and mud weight (open square) with standard deviation (horizontal bar) in Tract 1.

GP: 1.2-1.5 km

GP: 1.5-1.8 km

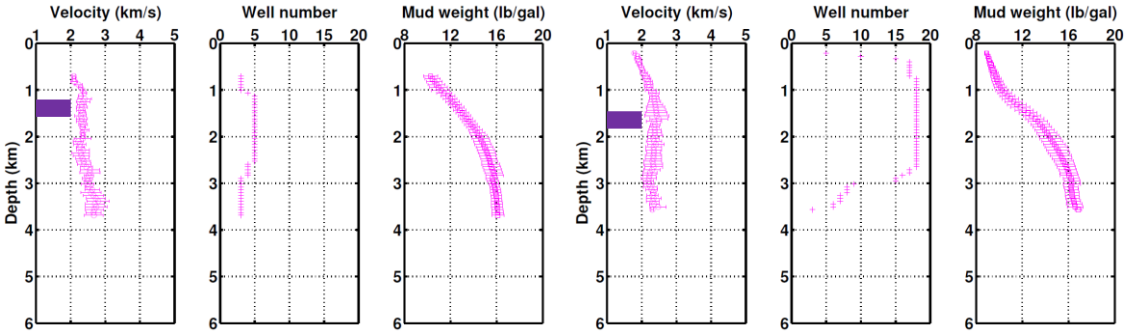

GP: 1.8-2.1 km

GP: 2.1-2.4 km

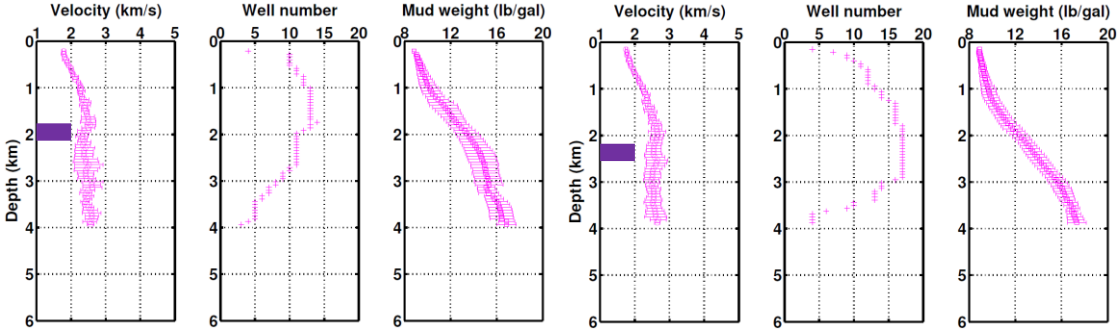

Figure 2-16: Mean shale velocity (open circle) and mud weight (open square) with standard deviation (horizontal bar) in Tract 6.

GP: 2.4-2.7 km

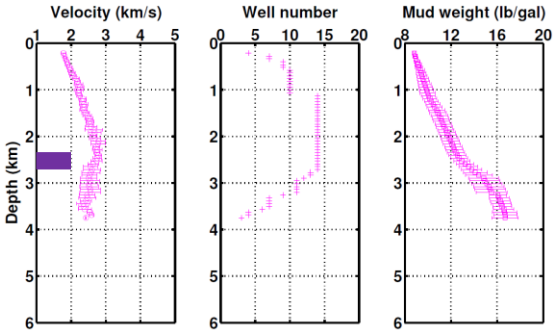

GP: 2.7-3.0 km

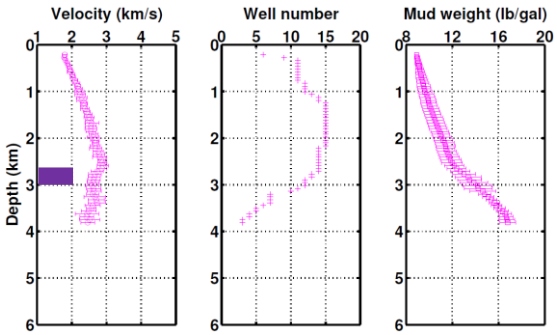

GP: 3.0-3.3 km

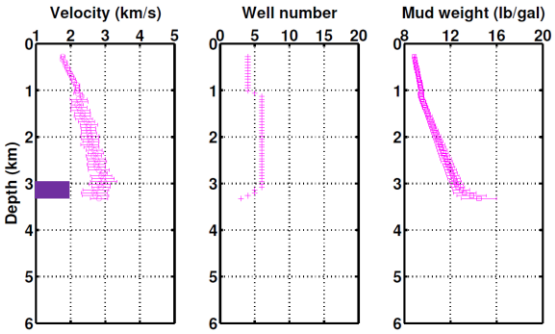

GP: 3.3-3.6 km

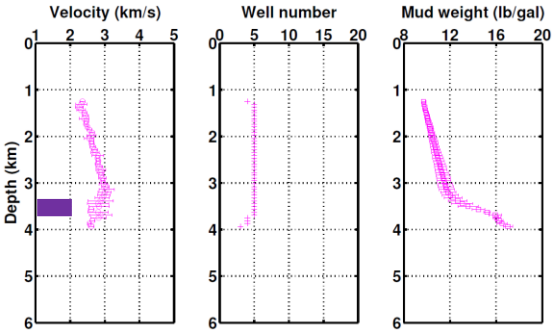

Figure 2-16: (continued) Mean shale velocity (open circle) and mud weight (open square) with standard deviation (horizontal bar) in Tract 6.

(a)

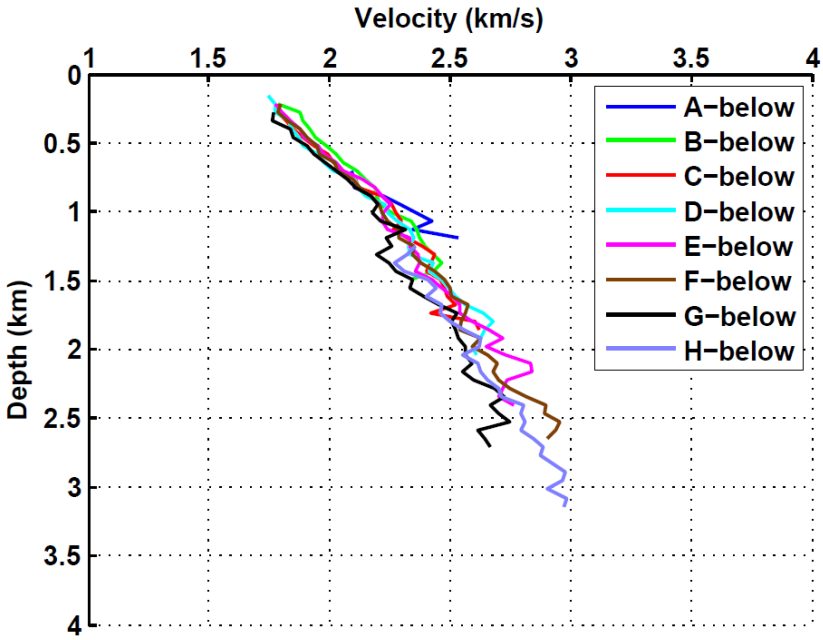

(b)

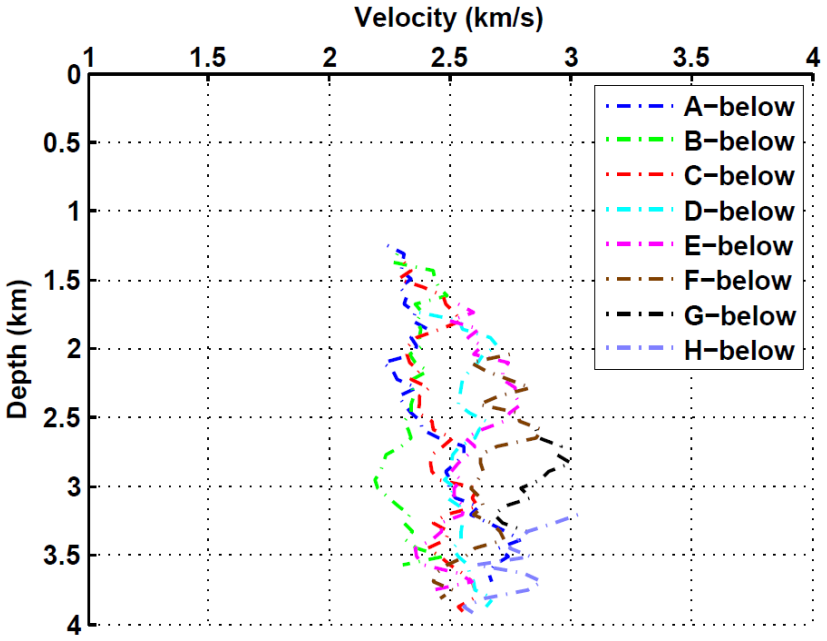

Figure 2-17: Velocity comparison of A-H zones in Tract 6; (a) is above GP and (b) is below GP.

We also plot in Figure 2-18, the freeze velocity and depth of GP onset for 8 zones and compare to the velocity NCT defined earlier for Tract 6. This figure demonstrates in the southern area that the velocity freezes at the onset of GP, and that the velocity at freeze point can be predicted by extending the normal compaction trend.

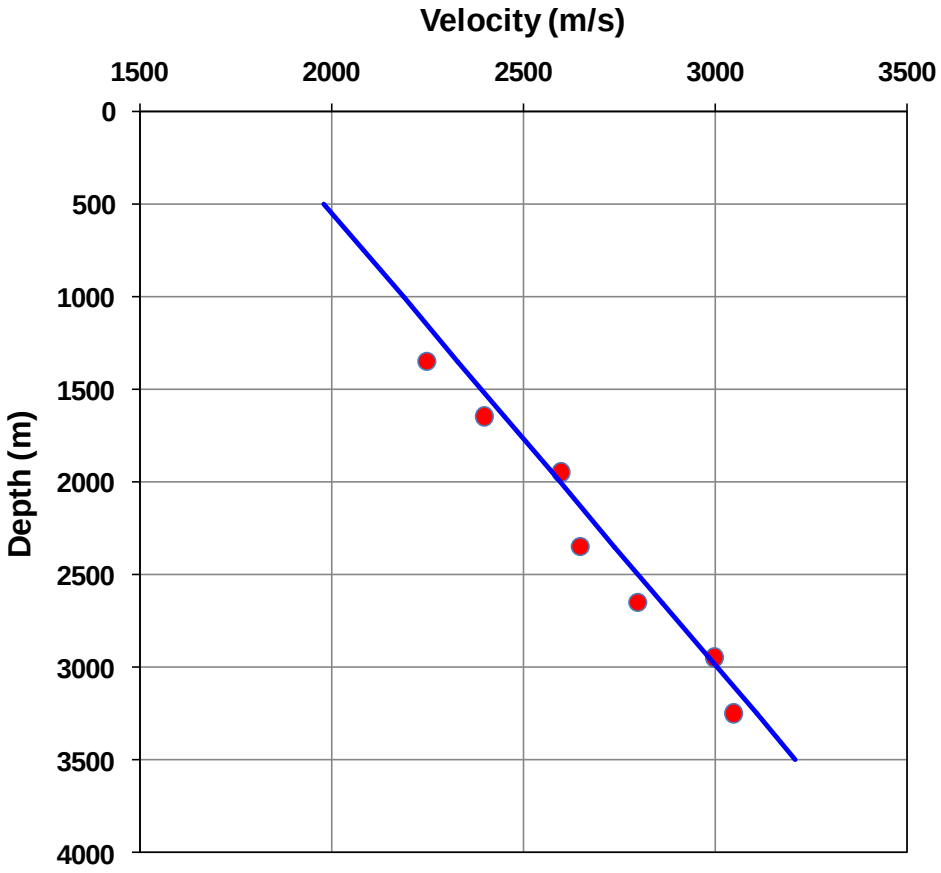

Figure 2-18: Relationship between the 'freezing' velocity and onset of GP depth for Tract 6. The blue line is the NCT defined in section 2.3.2 from equation (2-6) with coefficients for Tract 6 in Table 2-3 above geopressure.

The other important information conveyed by Figures 2-11, 2-12, 2-15, and 2-16 is the good correspondence between depth of onset GP and depth where the average mud

weight reaches 12 lb/gal. Thus, the 12 lb/gal mud weight is a reasonable threshold for distinguishing the onset of normal and abnormal pressure zones, which was assumed in previous sections and will be accepted in the next chapters.

2.4 Discussion

There are two categories of density and velocity trends among the 6 tracts. Tracts 1 through 4 have similar density and velocity trends: density increases through both normal and abnormal pressure, while velocity linearly increases above geopressure and decreases slightly below geopressure. And in Tracts 1 through 4, geopressure starts at very deep depths, around 3000 m. Comparatively, density and velocity show distinct trends in Tracts 5 and 6. Both density and velocity increase above geopressure, while below geopressure the density and velocity 'freeze' at the onset of geopressure. Additionally geopressure starts at very shallow depths, around 1500 m.

The different density and velocity responses result from different pressure regimes. In the northern areas we believe smectite to illite transition is the main mechanism causing geopressure; while in the southern areas compaction disequilibrium is the dominant mechanism. Then the question is "What causes the northern and southern areas to exhibit different geopressure mechanisms?" Next we outline two factors: sand percentage and temperature that impact the pressure regime.

2.4.1 Sand percentage

Sand percentage has a big impact on the onset depth of geopressure. This relationship can be seen in Figure 2-19. Similar to Figure 2-6, three depth panels including temperature, sand percentage, and the number of wells entering into the statistics are displayed for each tract. The red annotations relate to statistical values in normal pressure; and blue, abnormal pressure. A sand percentage less than 25% appears to be a threshold for abnormal pressure build-up because there are fewer sand pathways to carry expelled shale water to ocean bottom.

In order to gain an insights about the regional distribution of geopressure, sand percentage between different depth levels are computed for the whole study area. Sand percentage maps for different depth intervals are shown: 2000-3000 ft (600-900 m) (Figure 2-20 (a)), 5000-6000 ft (1500-1800 m) (Figure 2-20 (b)), 9000-10000 ft (2700-3000 m) (Figure 2-20 (c)), and, 10000-11000 ft (3000- 3300 m) (Figure 2-20 (d)). Figure 2-20 (a) shows a sand percentage map for shallow depths where the sediments in the whole study area have very high sand percentage content. The pore fluids in this sediment volume have a good exchange with surface water, so no abnormal pressure is established in the whole area. As the strata approaches 1500 m (Figure 2-20 (b)) the sand percentage in the southern area decreases to ~25%, where geopressure starts to build up. Comparatively, in the northern area at this depth, the sediment sand percentage is still high up to 40%, so no overpressure builds up in the northern area until at 9000-10000 ft

(2700-3000 m) when the sand percentage dips beneath 25% (Figure 2-20 (c)). Geopressure starts to build up in these regions of low sand percentage. And below 10000 ft (3000 m), the sand percentage in the whole study area is very low, generally less than 25%, and geopressure exists in the whole area (Figure 2-20 (d)). But even at this depth, the northern area stills contains a much higher sand percentage. As mentioned, hard onset of geopressure is common in northern area, which means the pore pressure increases suddenly. So there should be other factors contributing to this abrupt increase of pore pressure in the northern area.

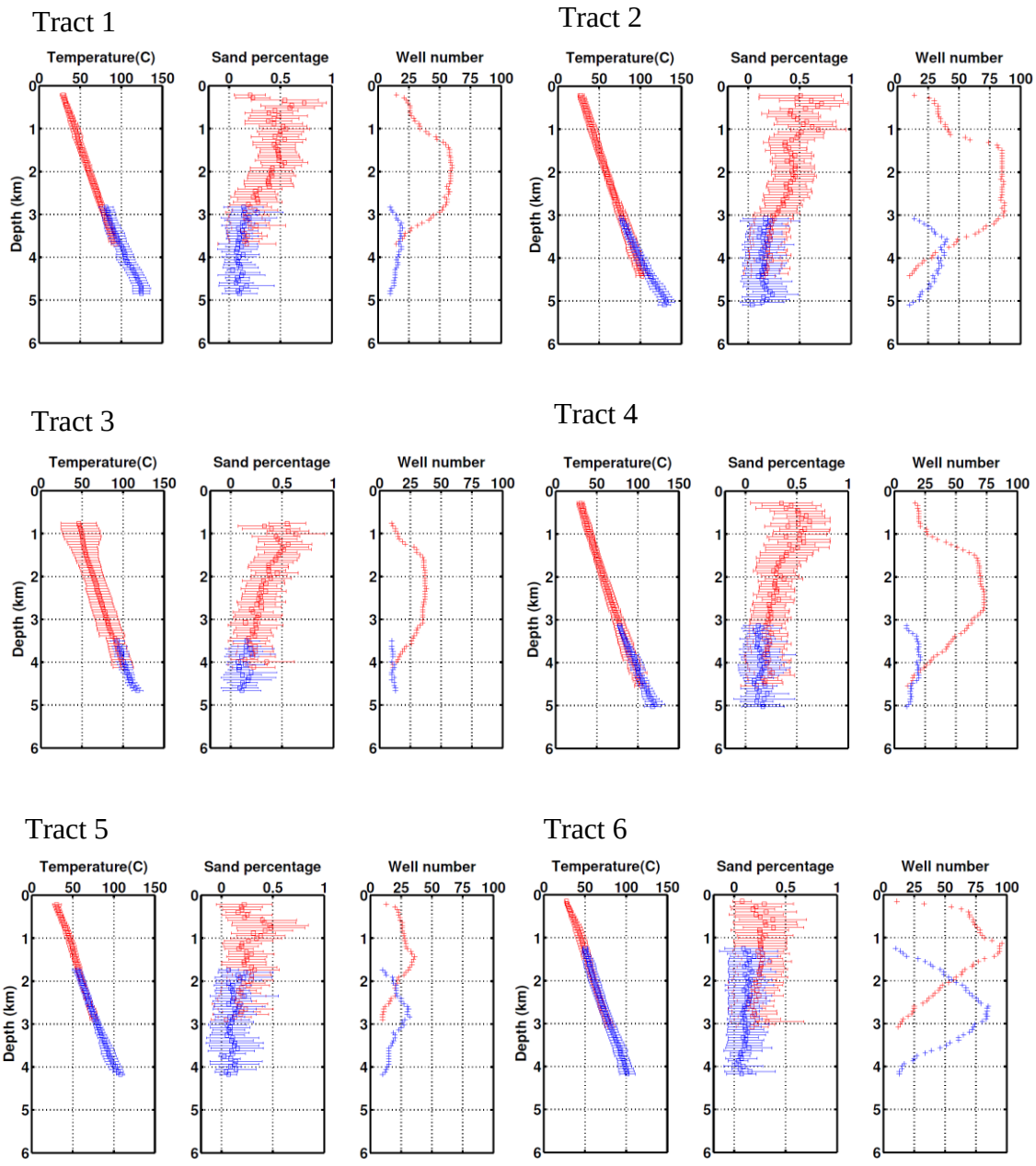

Figure 2-19: Mean temperature (open square) and sand percentage (open square) with standard deviation (horizontal bar) for above (red) and below (blue) onset of geopressure for Tracts 1 to 6.

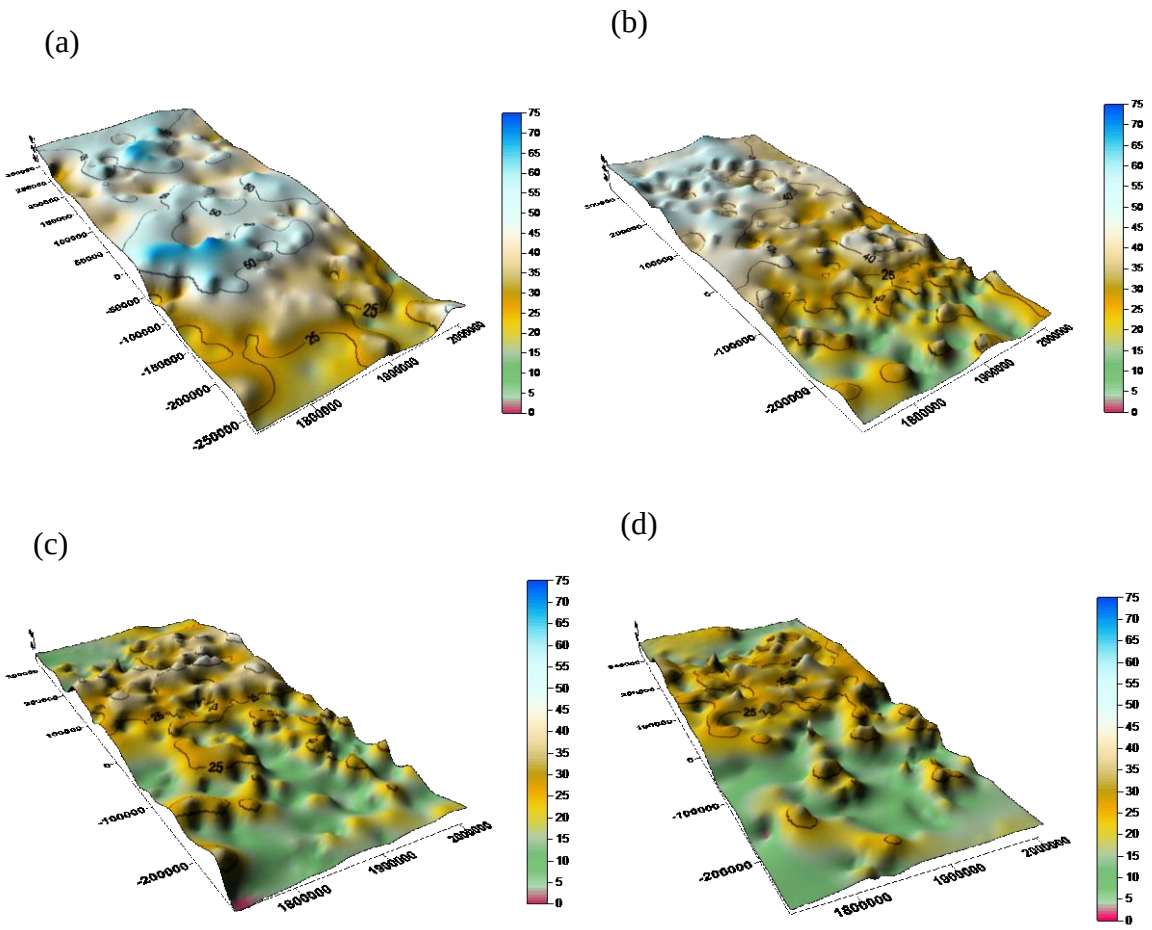

Figure 2-20: Sand percentage distribution in the whole study area at (a) 2000-3000 ft (600-900 m), (b) 5000-6000 ft (1500-1800 m), (c) 9000-10000 ft (2700-3000 m), (d) 10000-11000 ft (3000-3300 m).

2.4.2 Smectite to illite transition

The temperature distributions of six tracts are very interesting (Figure 2-19). In the northern area, this includes Tracts 1 and 2, the temperature gradient increases below geopressure. Temperature reaches over 70 ℃ around 3000 m at which point smectite

starts to change into illite (Colton-Bradley, 1987). While for Tracts 3 to 6 the temperature gradient doesn't change much. Tracts 1 and 2 have the biggest gradient, followed by transitional Tracts 3 and 4. Tracts 5 and 6 have the lowest temperature gradient beneath 3000 m (Figure 2-21). Another point is the temperature gradient for abnormal pressure in Tract 1 appears to be shifted towards higher temperatures.

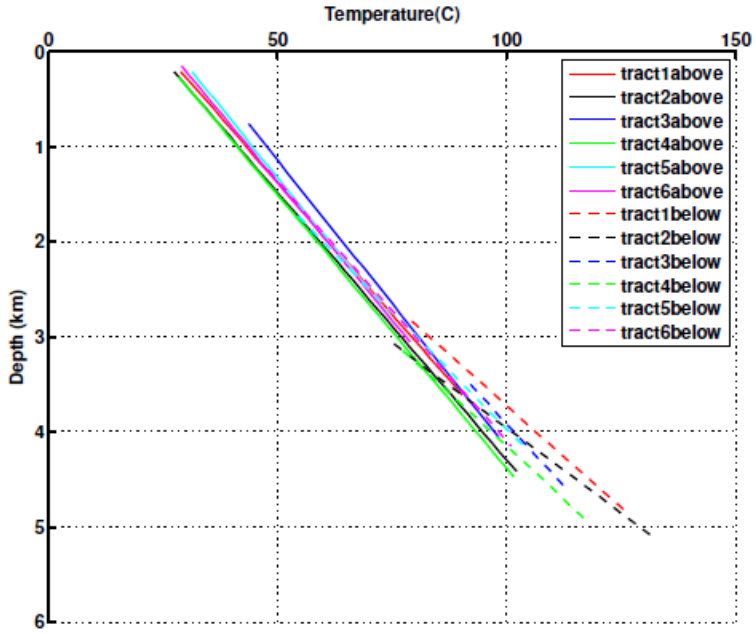

Figure 2-21: Temperature gradient comparison among 6 tracts.

During burial, the increase of temperature results in ions exchange between the pore fluids and clay structure, which ultimately transforms clays from one category to another. This process is known as diagenesis (Grim, 1953; Hunnur, 2006; Meunier., 2005). The diagenesis of smectite, principally montmorillonite, to illite has important implications for overpressure development in shale. The structure of montmorillonite is that of an octahedral layer sandwiched between two tetrahedral layers (Hunnur, 2006). About one eighth of the octahedral aluminum ions in montmorillonite are replaced by the magnesium ion. It results in the ability to draw water into the interlayer space, which makes the clay swell. Other ionic substitution can also occur, as silicon ions in the tetrahedral layers are replaced by aluminum ions. The increase in the charge imbalance allows other cations, commonly potassium, to be fixed in the interlayer position. This change means the transformation of smectite to illite, which will release interlayer water (Figure 2-22). The increased free pore water raises the possibility to augment the overpressure in a proper environment.

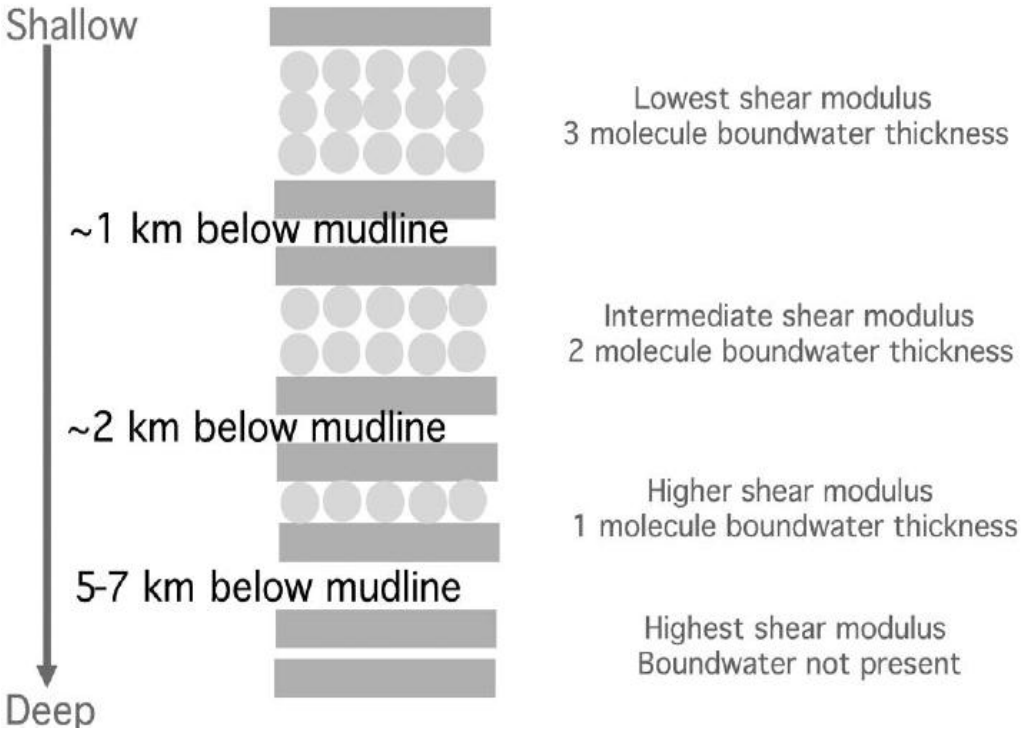

Figure 2-22: Smectite transformation to illite through depth (from Heppard and Ebrom, 2010).

The sediment in the Gulf of Mexico contains a significant amount of smectite (Heppard and Ebrom, 2010). Generally smectite starts to dehydrate at over 70 ℃. When the temperature rises up to 95 ℃ a huge amount of smectite transforms into illite (Pollastro, 1993). The released bound water from this process causes the overpressure build-up. Figure 2-21 shows it appears at around 3000 m the geothermal gradient in the northern area increase, while the geothermal gradient looks to be constant in the southern area. Detailed temperature statistics in Tracts 1 and 6 (Figure 2-23 and Figure 2-24) obviously show there is a geothermal gradient variation below 3 km. The temperature environment

provides a favorite place for smectite to transform into illite beneath 3 km. The matrix density of illite is higher than smectite (Grim, 1953); this could be the reason why in northern area the density keeps increasing below geopressure. In the southern area most of wells in this study do not penetrate to the deeper depth where higher temperatures exist. The correspondence between geothermal gradient variations to the onset depth of hard pressure in northern area, suggest clay diagenesis could play a crucial role in the pore pressure build-up in the deeper and hotter environment beneath 3000 m.

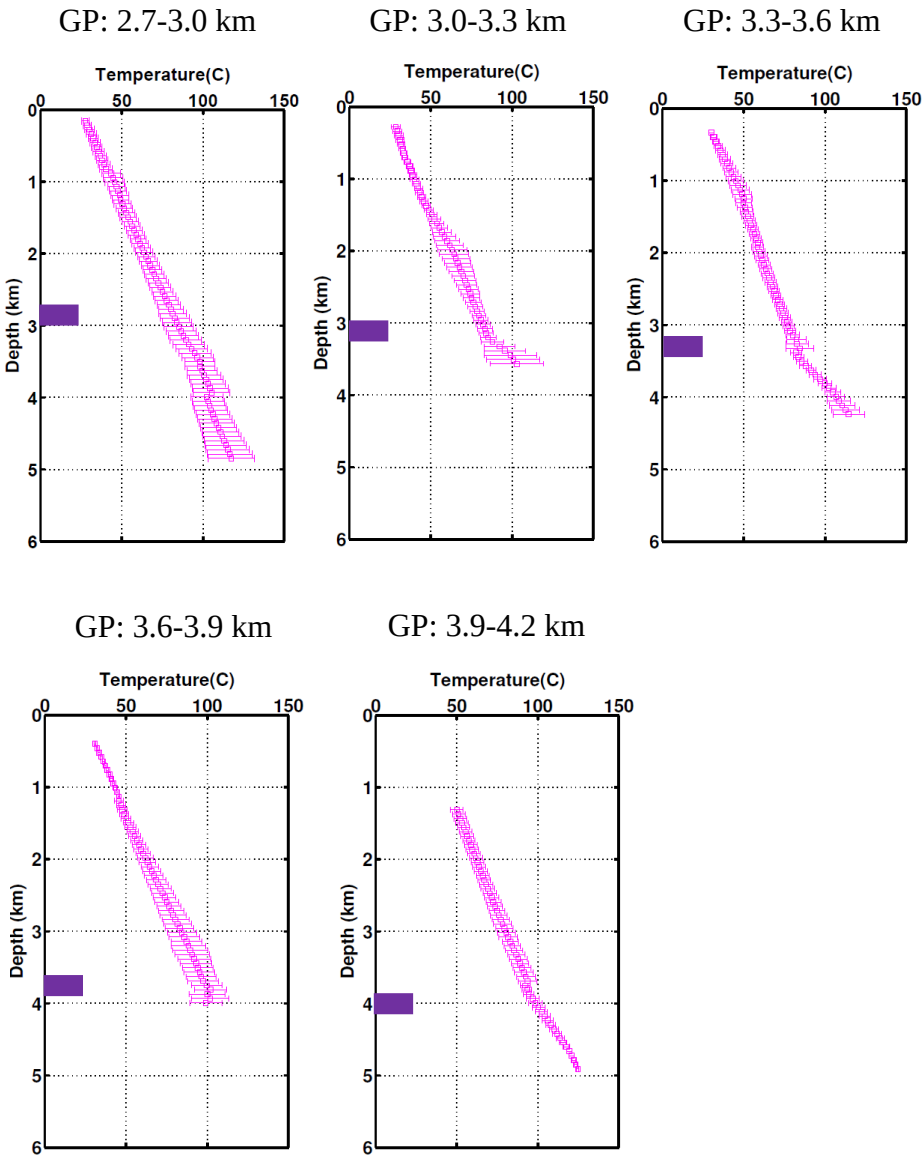

Figure 2-23: Mean temperature (open square) with standard deviation (horizontal bar) for different zones based on onset of GP in Tract 1.

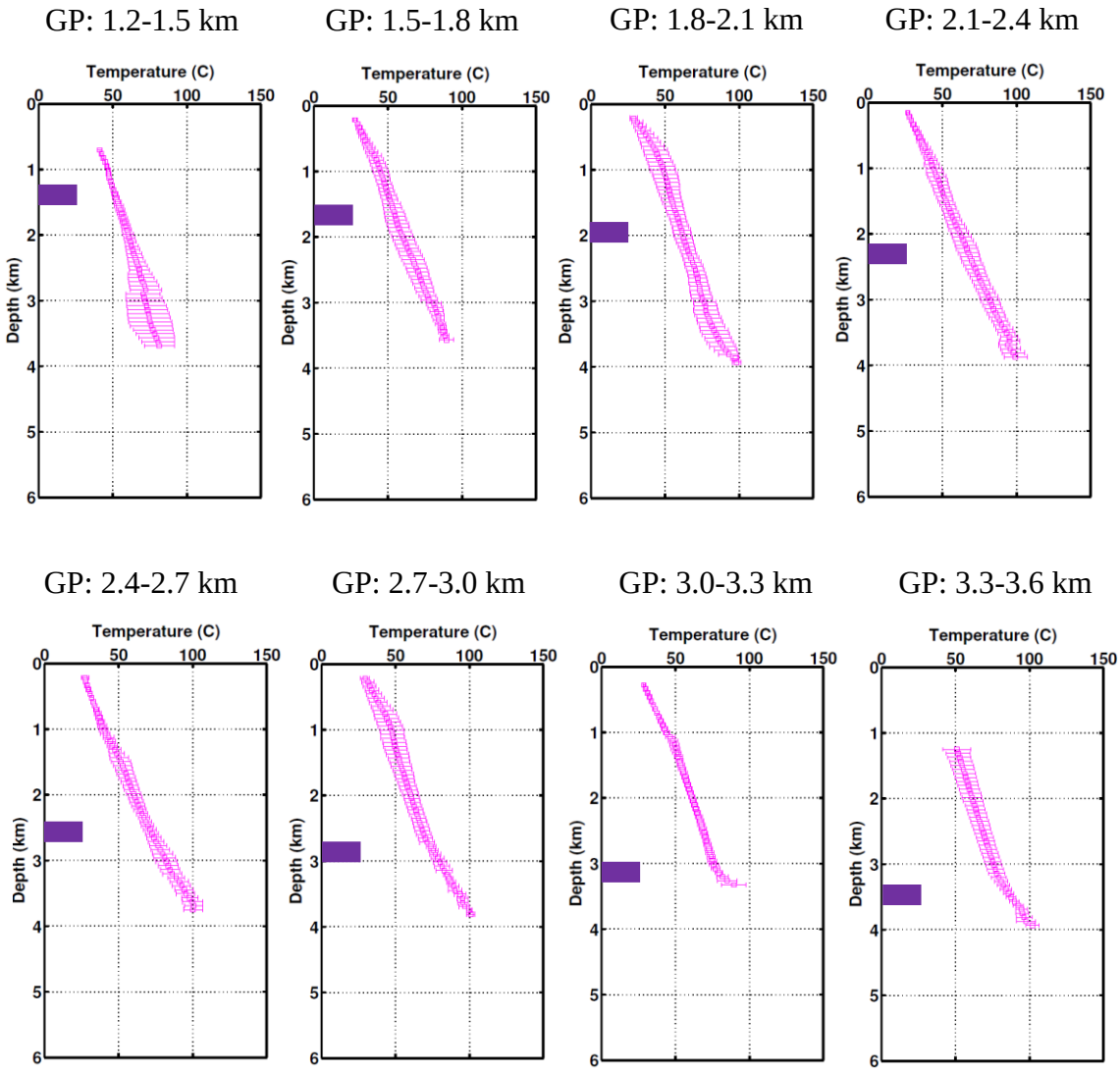

Figure 2-24: Mean temperature (open square) with standard deviation (horizontal bar) for different zones based on onset of GP in Tract 6.

A debate about elastic unloading or inelastic unloading associated with hard onset of GP exists for the GOM (Bowers, 1995; Katahara, 2006). Important evidence to support these two hypotheses is the relationship between sediment density and velocity. For the elastic unloading process, velocity decreases in GP zone while density is constant (Bowers, 1995). For inelastic unloading or smectite to illite transformation, velocity just decreases slightly or is constant but density increases instead (Lahann and Swarbrick, 2011).

The density-velocity trends in Tract 1 are plotted in Figure 2-25. In this plot there are three distinct trends. The red line is normal compaction trend where density linearly increases with velocity. In the blue trend, velocity decreases while density keeps increase, this is inelastic unloading process. The increase of density is assumed due to smectite transformation to illite based on previous observations. One study showed that as smectite starts to change into illite, the pallets collapse and rock frame becomes weaker (Lahann and Swarbrick, 2011), therefore pressure sustained by the rock structure decreases and velocity drops. It is an unloading process, where over pressure builds up in the pore space at the mean time. This process continues until fluid incompressibility is high enough to bear any addition of overburden pressure. It is like the undercompation process in which pressure in pore fluid increases at the same gradient as overburden pressure. Therefore the load on the rock frame is constant but density keeps increasing as more stable illite structure forms. This process is called load transfer based on Lahann and Swarbrick (2011) paper, in which velocity does not change. Variation of temperature

gradient with the density-velocity relationship in geopressure tends to support the inelastic unloading process dominates in the northern area.

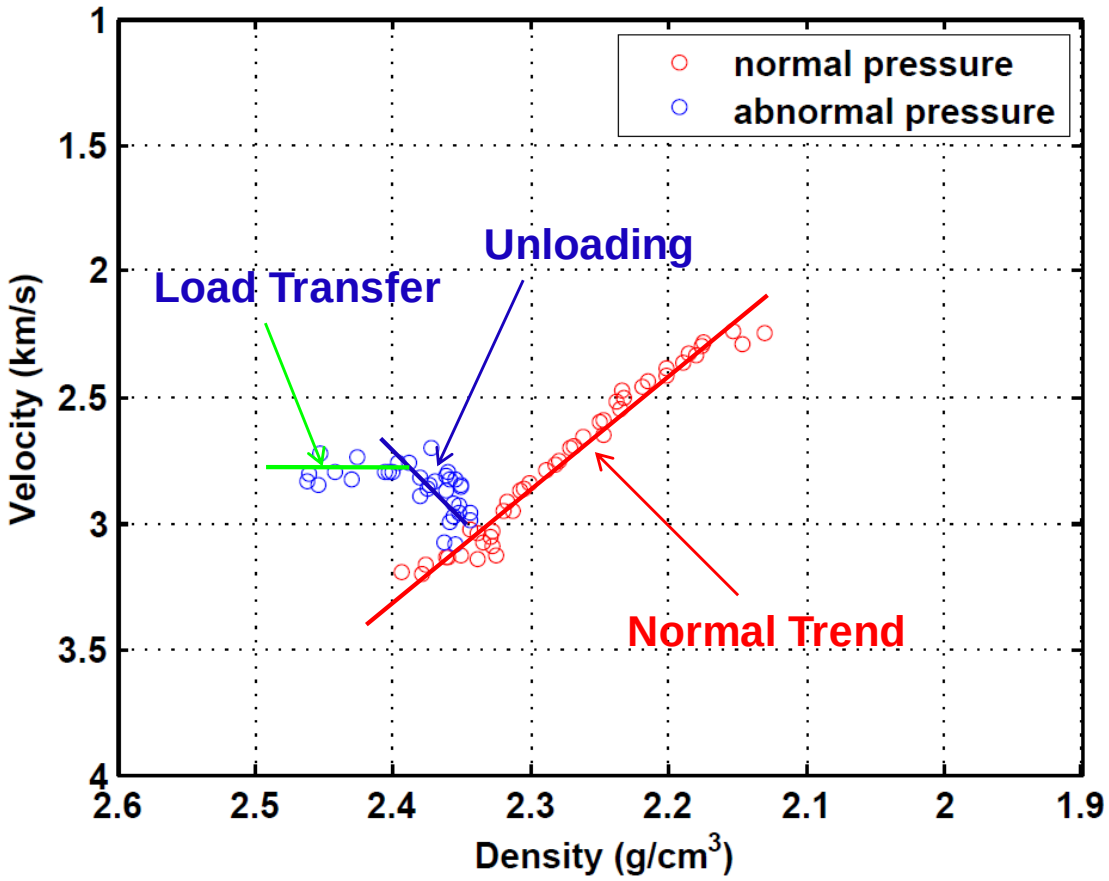

Figure 2-25: Density and velocity trends in Tract 1.

2.5 Summary

From north to south with the variation of geopressure, the shale density and velocity trends are quite different. In northern portion the density trend is not influenced by the pressure, while in southern area both density and velocity freeze beneath geopressure.

Sand percentage and temperature and are two key factors controlling the type of geopressure. In northern GOM there is hot detabe about the mechanism for geopressure, elastic unloading and/or smectite-illite transformation (Bower, 1995; Katahara, 2006). From our temperture analysis and velocity-density relation we prefer smectite-illite transformation as the major reason for overpressure generation in the northern area. In southern area, undercompaction is the dominant mechanism for geopressure build-up. Its effect on density trends need to be considered when an accurate overburden pressure model is desired.

3 EFFECTIVE PRESSURE COEFFICIENTS

3.1 Introduction

There are a significant number of empirical methods to predict pore pressure from seismic data or well-log data. Many of these algorithms are based on equation (1-9) which states that seismic velocity is governed by the effective stress law. Gutierrez et al. (2006) made a detailed review of these methods and compared their accuracy. But in current exploration and drilling practice, the effective pressure coefficient, n, is generally assumed as unity. In short, pore-pressure practitioners talk about differential pressure, not effective pressure. Most studies on the calibration of n are done in laboratories (Banthia et al., 1965; Wyllie et al., 1958; Christensen and Wang, 1985; Hornby, 1996; Hofmann et al., 2005; Sarker and Batzle, 2008). There are a few field data sets that show the dynamic variation of n. In one case study, Ebrom et al. (2004) pointed out that for highly unconsolidated shale n equals one, but for well-consolidated shale n approaches zero based on field observations of V_P. As a means of calibrating n in the GOM, they associated extremely pressured shale with a local minimum velocity as having a pore pressure gradient close to the formation fracture gradient and were then calculated a value of 0.88 for n. A challenge in their method is the establishment of the minimum velocity trend of shale, which means a large dataset is necessary. Sarker and Batzle (2008) discussed the application of n to Eaton's pore pressure equation and found that for P-wave velocity, n equals 0.7 when Eaton's exponent is set to one.

In this study, we expanded upon the Ebrom et al (2004) methodology to predict n from the minimum shale velocity. Our dataset includes 487 wells with shale volume curves and other shale properties for more than 20000 60 m intervals. Minimum velocity trends are established for the 6 tracts shown in Figure 2-1. With the minimum velocity and normal compaction trends established in each tract, trends for n are developed from the effective stress law.

3.2 Methods

In order to compute n, we developed methods to estimate the overburden pressure, effective pressure, and pore pressure which are needed in equation (1-9). The following sections show in detail how to compute these quantities.

3.2.1 Overburden pressure model

The first step to compute effective pressure coefficient is to quantify overburden pressure, which is usually determined by the density-depth trends. In chapter 2 we show the shale density trends for the six tracts (Figure 2-6). However, since the sediment section contains both sand and shale, average density trends are needed to establish the density-depth trends for overburden pressure rather than just shale trends. Figure 3-1 shows the average density trends in the six tracts. They are quite similar to the shale trends (Figure 2-6). We fit the average density trends with the same mathematical expressions as used in

Chapter 2 to quantify the shale trends. The average density parameters for equation (2-3) and the RMS errors for the six tracts in the normal pressure zone are listed in Table 3-1.

Table 3-1: Least-squares coefficients and RMS errors for average density trends in normal pressure for the 6 tracts.

	Normal trends of density			
Tract	ρ_0 (g/cm^3)	a (g/cm^3)	b (1/m)	Δ (g/cm^3)
1	2.82	0.84	1.67×10^{-4}	0.01
2	6.42	4.41	2.13×10^{-5}	0.01
3	2.58	0.67	3.05×10^{-4}	0.02
4	3.02	0.97	1.03×10^{-4}	0.01
5	2.32	0.45	9.11×10^{-4}	0.01
6	4.02	1.94	4.51×10^{-5}	0.01

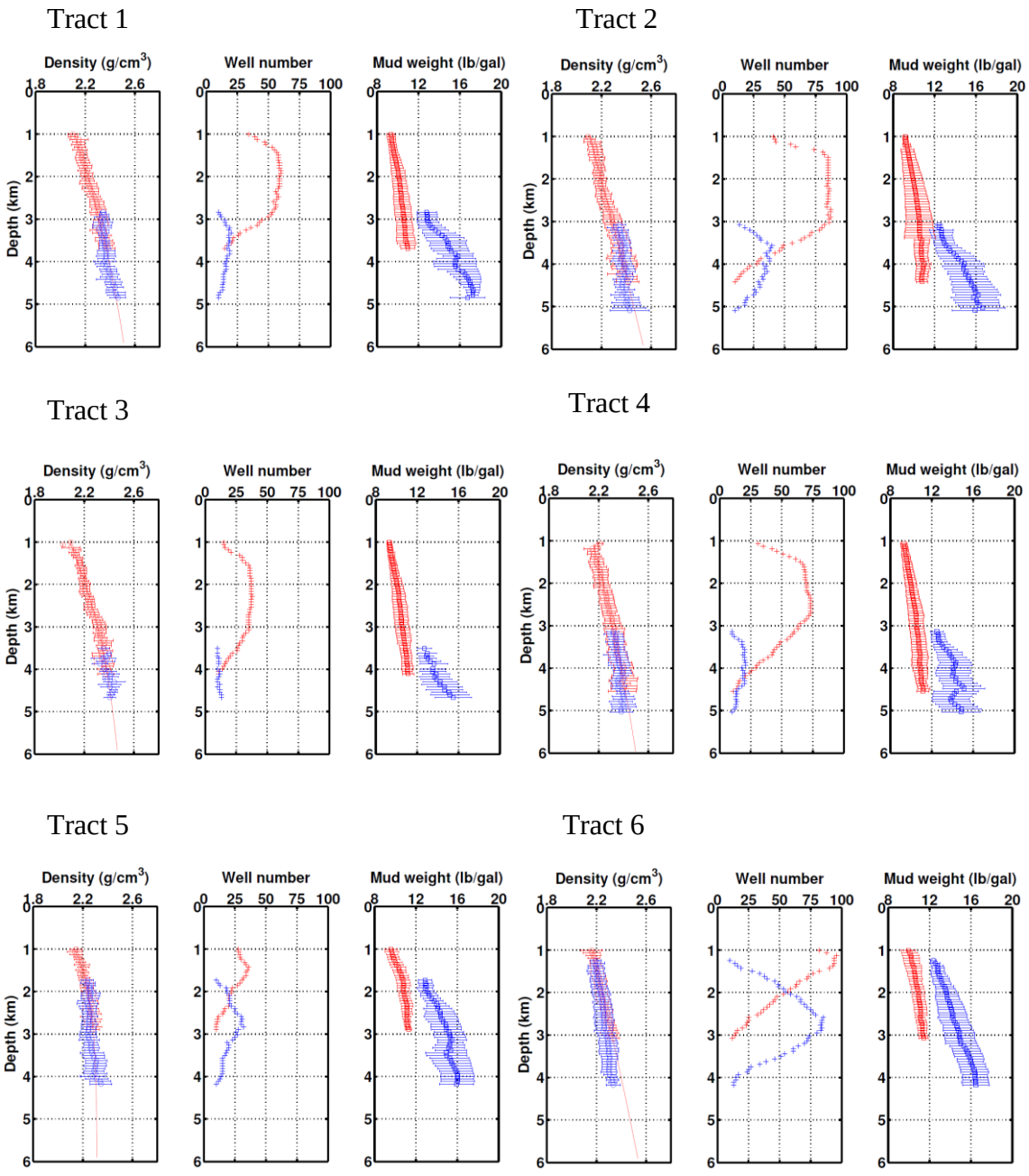

Figure 3-1: Mean average density (open circle) and mud weight (open square) with standard deviation (horizontal bar) for above (red) and below (blue) onset of geopressure for Tracts 1 to 6.

Overburden pressure (confining pressure) is computed from the integration of the appropriate density trend

$$P_C = g\rho_w z_w + g\int_0^z \rho_b(z)dz\,, \tag{3-1}$$

where g is the gravitational constant 9.8 m/s^2; z is the depth from ocean bottom in m; ρ_w is the seawater density, which is 1.07 g/cm^3 (Fertl et al., 1976); and z_w is the water depth, which is approximately 30 m in the northern Tracts 1 and 2, 60 m in the transitional Tracts 3 and 4, and 90 m in the southern Tracts 5 and 6. For Tracts 1 to 4 the overburden pressure is computed from equation (3-2) for the whole section where ρ_0, a and b are coefficients listed in Table 3-1. For Tracts 5 and 6 the depth is divided into two zones; one above geopressure, and the other below geopressure. The confining pressure is then computed with equation (3-3) where the onset depth of GP is z_{GP}. The density, ρ_{freeze}, is the density at the onset of geopressure and this density doesn't change significantly below z_{GP}.

$$\begin{aligned} P_C &= g\rho_w z_w + g\int_0^z \rho_b(z)dz \\ &= g\rho_w z_w + g\int_0^z (\rho_0 - ae^{-bz})dz \\ &= g[\rho_w z_w + \rho_0 z + \frac{a}{b}(e^{-bz} - 1)]. \end{aligned} \tag{3-2}$$

$$
\begin{aligned}
P_C &= g\rho_w z_w + g\int_0^{z_{GP}} \rho_b(z)dz + g\int_{z_{GP}}^{z} \rho_{freeze}dz \\
&= g\rho_w z_w + g\int_0^{z_{GP}} (\rho_0 - ae^{-bz})dz + g\rho_{freeze}(z - z_{GP}) \\
&= g[\rho_w z_w + \rho_0 z_{GP} + \frac{a}{b}(e^{-bz_{GP}} - 1) + \rho_{freeze}(z - z_{GP})].
\end{aligned}
\tag{3-3}
$$

3.2.2 Depth adjusted normal compaction trend

In order to compute effective pressure, a normal compaction trend for V_P is required. As discussed in Chapter 2, when shale is subjected to overburden pressure and normal pore pressure, its porosity usually reduces exponentially with depth (e.g. Athy, 1930; Swarbrick et al., 1998; Mondol et al., 2007). Many pore pressure prediction methods primarily rely on the establishment of NCT of porosity, or porosity-sensitive properties such as resistivity, density, or velocity (e.g. Gutierrez et al., 2006; Sayers 2010). But the challenge is that it is difficult to define a definitive normal compaction trend in some basins (Shaker, 2007; Dutta et al., 2009). For example, in the deep-water GOM, abnormal pressure starts to occur shortly beneath ocean bottom which is most likely associated with the lack of sand bed continuity to the ocean floor. This start of abnormal pressure occurs around 1500 m beneath the mud line, thus making it difficult to define a "real" normal compaction curve. In many of the pore-pressure prediction methods, an accurate normal compaction trend for shale velocity is crucial. In our study there are consistent linear velocity trends above geopressure as shown in Figure 2-9. But if these trends are checked in detail, there is a kink or knee on each velocity trend at about 1000 m. And the

corresponding mud weight profiles show a kink at the same depth. The kink in the mud weights might be caused by the interpolation technique applied from ocean bottom to 1000 m. The depth of 1000 m is close to the end of the first logging run and thus the first reported mud weight. This mud weight is interpolated with an assumed surface mud weight of 8.6 lb/gal. Below 1000 m, the mud weight is greater than hydrostatic gradient, 8.96 lb/gal in GOM (Fertl et al., 1976). This suggests that the sediment beneath 1000 m is already slightly overpressured. In order to compensate for this transitional overpressure effect on V_P in the 'normal' pressure zone, we use a depth-adjusted method (or equilibrium depth) to correct the observed NCT model. Referring to Figure 3-2, we treat the observed shale velocity NCT model as the initial NCT. A depth adjustment is applied to the initial NCT by moving the observed velocity at the depth of Z_{OBS} to the depth Z_{ADJ} according to

$$Z_{ADJ} = Z_{OBS}\left(\frac{19.2\text{-}Mud_{OBS}}{19.2\text{-}Mud_{HYD}}\right), \tag{3-4}$$

where Mud_{OBS} is the measured mud weight and Mud_{HYD} is the hydrostatic pressure gradient, which is 8.96 lb/gal (0.465 psi/ft) when the salt water density is 1.07 g/cm^3. Overburden pressure gradient is approximately 19.2 lb/gal (1.0 psi/ft) in the GOM assuming an average rock density of 2.3 g/cm^3 (Fertl et al., 1976; Gretener, 1976). Average mud weights in the 60 m intervals were applied in equation (3-4).

An observed velocity V_{OBS} in the slightly overpressured original NCT is moved vertically until the differential pressure of the original NCT model, P_{D_ORG}, at Z_{OBS} matches the differential pressure at the adjusted NCT model, P_{D_NCT}, at Z_{ADJ} (Figure 3-2). The depth

adjusted shale NCTs are shown in Figures 3-3 and 3-4 accompanied by the initial NCTs. The amount of overpressure is depicted in the mud weight profiles in the figures. By adjusting the velocity curve upward, the new NCT represents velocity readings from normally pressured shale. The adjusted shale velocity NCT is faster than the initial NCT. By combining all 6 normal compaction trends in Figure 3-5, we observe that Tracts 1 to 4 have a consistent NCT, while Tracts 5 and 6 have a slightly different one. The least-squares coefficients for equation 3-5 for the adjusted velocity trends in the six Tracts are listed in Table 3-2.

Velocity (m/s) $=v_0 + az$ (m). (3-5)

The RMS velocity errors as defined in equation (2-5) are also shown in Table 3-2. As equation (3-5) was fit with field data to a depth of 6000 m, caution has to be taken when extending this trend beyond 6000 m.

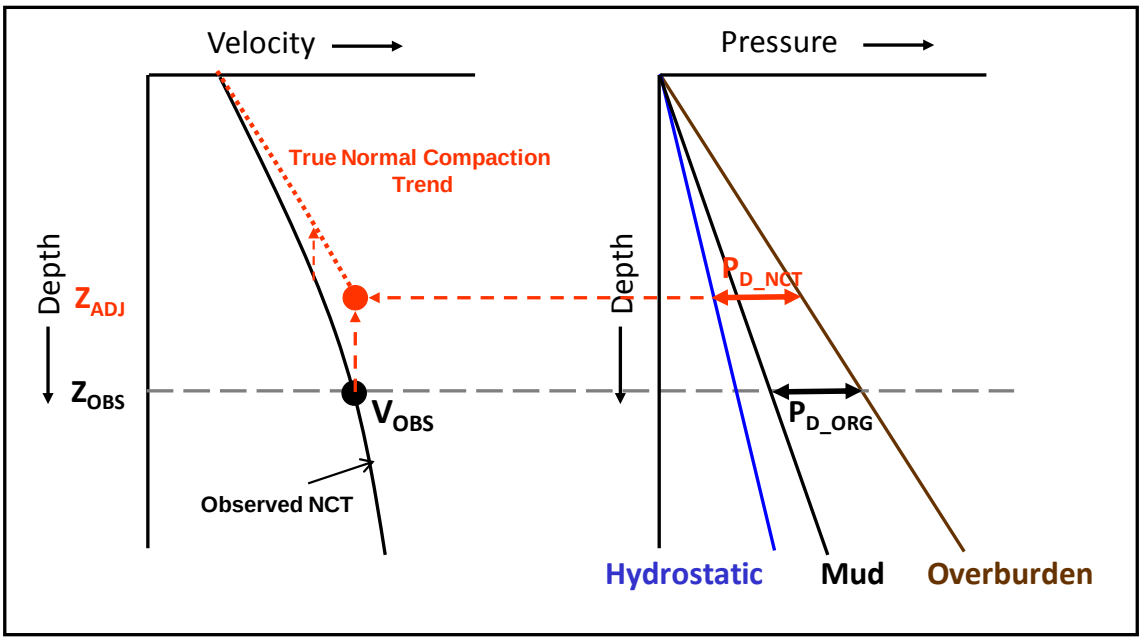

Figure 3-2: Illustration of depth adjustment method to establish normal compaction trend at hydrostatic pore pressure.

Tract 1

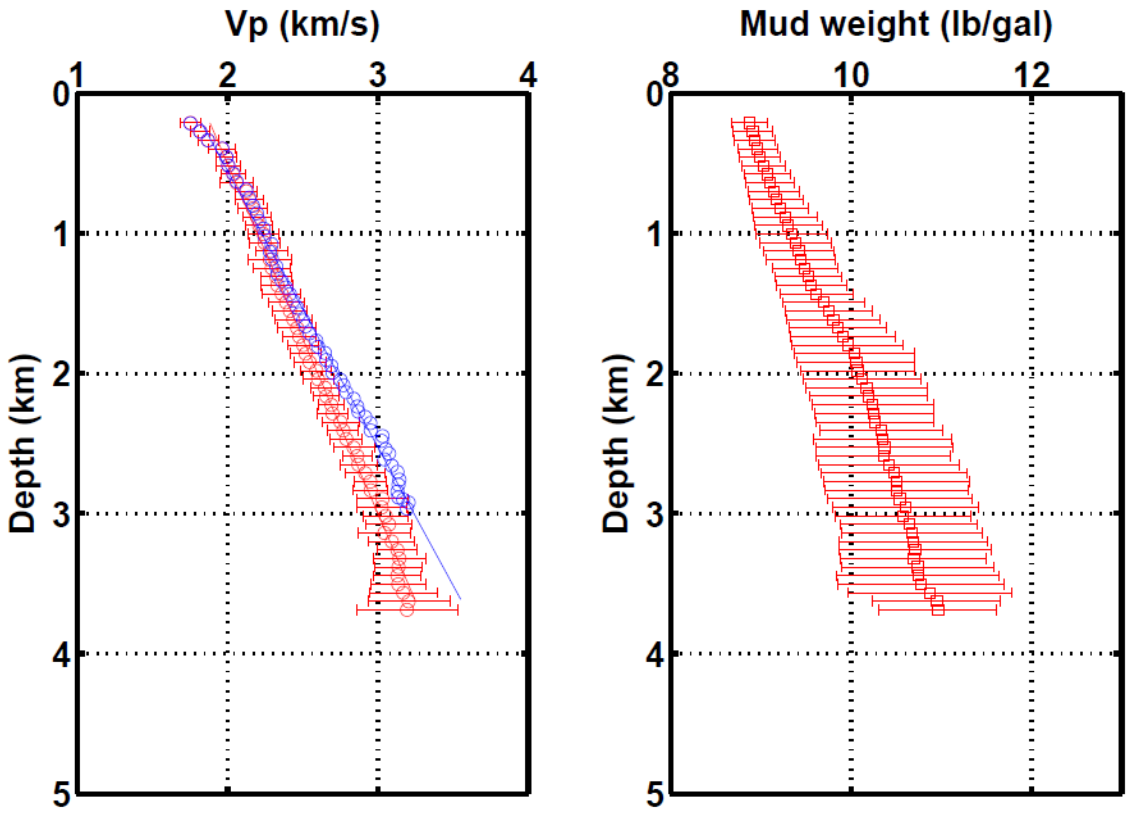

Figure 3-3: Original shale velocity NCT (red circles) and the depth-adjusted NCT (blue circles) for Tract 1.

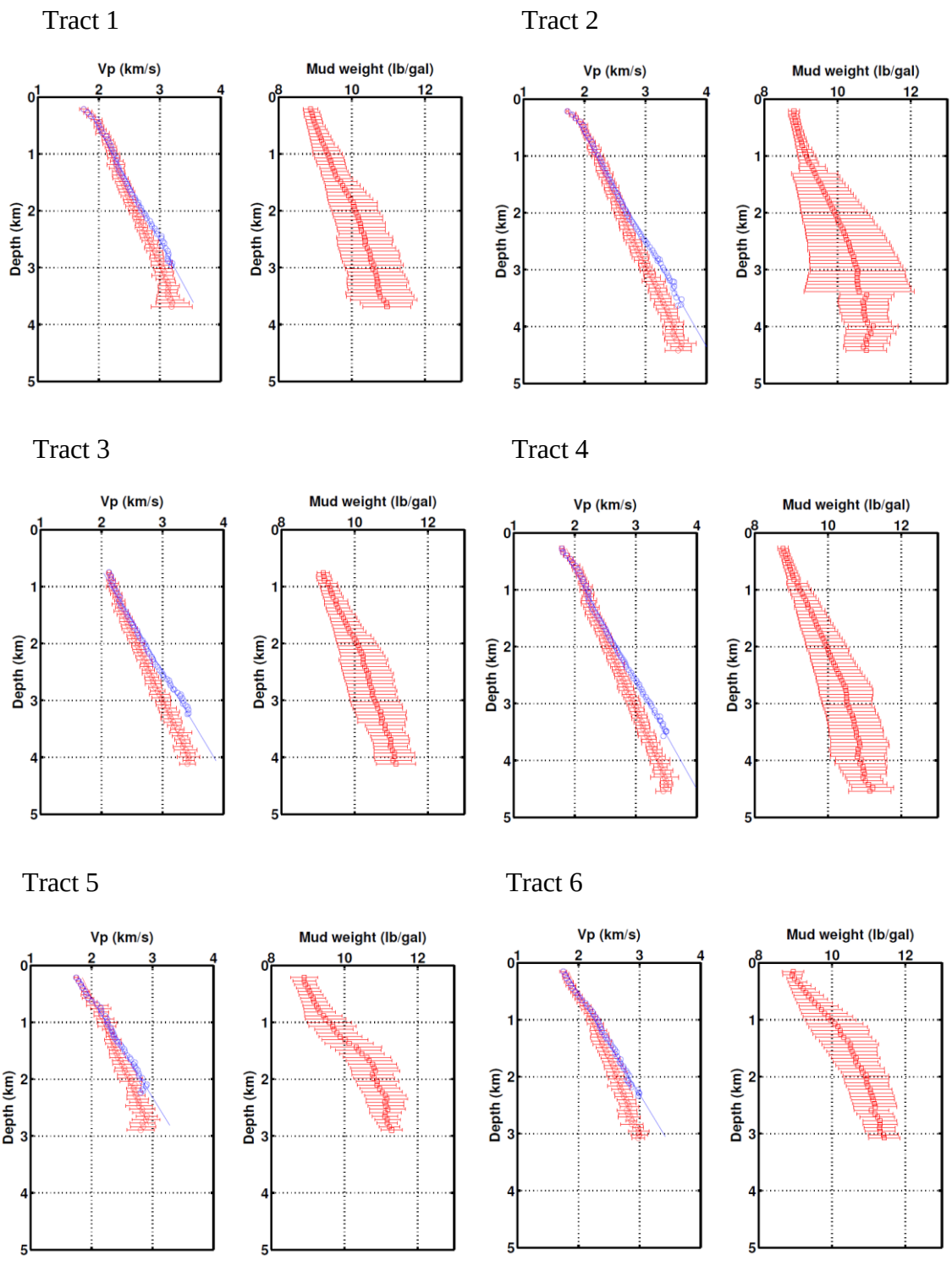

Figure 3-4: Original shale velocity NCTs (red circles) and the depth-adjusted NCTs (blue circles) for Tracts 1 to 6.

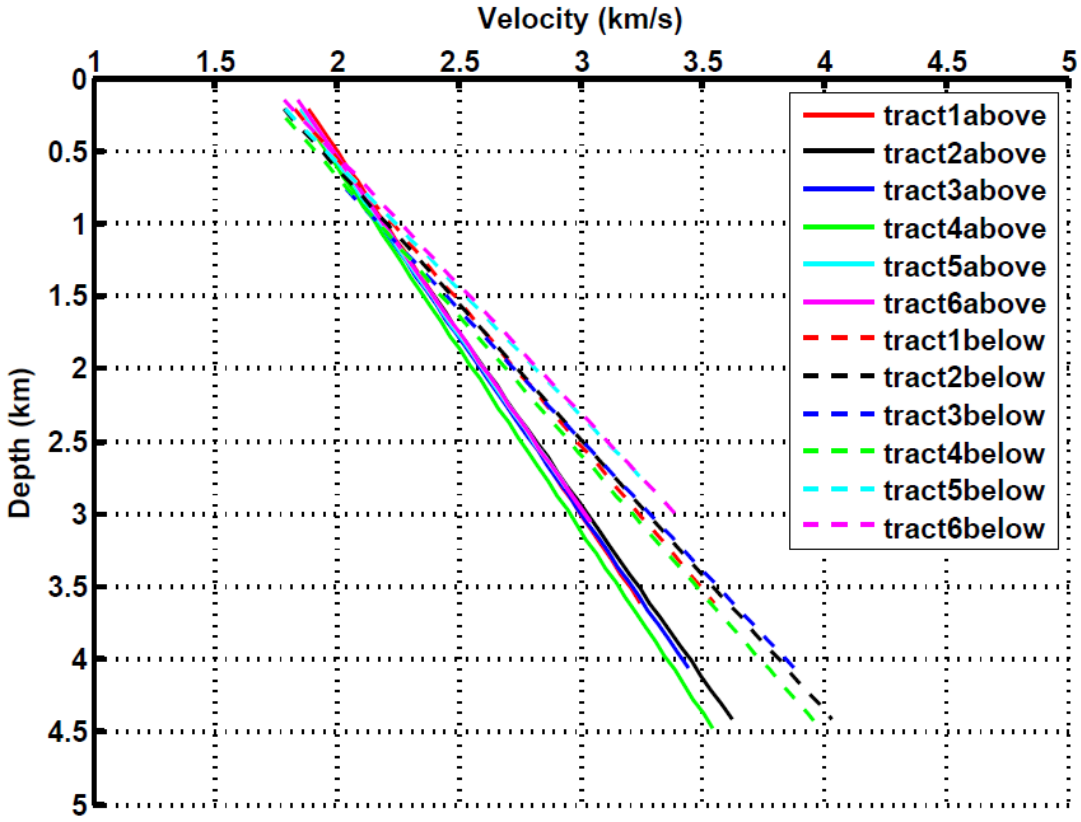

Figure 3-5: Comparison between the original NCT and adjusted NCT for the 6 Tracts.

Table 3-2: Least-squares coefficients and RMS errors for adjusted shale velocity NCT (equation 3-5).

	Above Geopressure		
Tract	V_0 (m/s)	a (m^2/s)	Δ (m/s)
1	1719	0.51	33.87
2	1668	0.54	35.26
3	1609	0.56	40.05
4	1648	0.52	34.28
5	1665	0.58	39.54
6	1697	0.56	32.60

3.2.3 Minimum velocity model

Instead of using Eaton or Bower's empirical equations to predict the effective pressure, we extended Ebrom's et al. (2004) minimum velocity model to compute n and then predict pore pressure. The key issue of this method is to define a minimum velocity trend, which represents the lowest expected velocity for extremely overpressured shale (Hilterman, et al., 1998). Numerous log statistics show shale with resistivity values less than 0.35 ohm-m indicate that the pore pressure is extremely high, approaching the

fracture gradient (Hottman et al., 1965; Hilterman et al., 1998). In the current study, we first established the minimum velocity based on the data with mud weights greater than 12 lb/gal and resistivity values less than 0.35. For those shale points under an extremely large abnormal pressure, we further assume when pore pressure approximates the fracture gradient the pore pressure approaches the overburden pressure. Referring to Figure 3-6, n is computed as

1. Establish the minimum velocity trend for each tract; identify the minimum velocity V_{MIN} and depth Z_{MIN} for each data point on the trend.

2. Vertically extend V_{MIN} to intercept the NCT curve at V_{NORM}, and find the corresponding normal compaction depth Z_{NORM}. That is:

$$V_{MIN}=V_{NORM}=V_0+aZ_{NORM}, \quad (3\text{-}6)$$

where V_0, a and V_{MIN} are known values. Z_{NORM} is derived from equation (3-6).

3. Compute the overburden pressures, P_C (Z_{MIN}) and P_C (Z_{NORM}), at the depths of Z_{MIN} and Z_{NORM} respectively by using equations (3-2) or (3-3).

4. At depth Z_{NORM}, compute the normal effective pressure as

$$P_E (Z_{NORM}) = P_D (Z_{NORM}) = P_C (Z_{NORM}) - P_{HYDRO} (Z_{NORM})$$

$$= P_C (Z_{NORM}) - 0.01*Z_{NORM}, \quad (3\text{-}7)$$

where P_{HYDRO} is the hydrostatic pressure, which has a gradient in the GOM of 0.465 psi/ft (0.01 MPa/m) (Fertl et al., 1976; Bowers, 1995). Here we make the assumption that n equals one for normally pressured shale.

5. At depth Z_{MIN}, V_{MIN} is on the minimum shale velocity trend such that the pore pressure P_P (Z_{MIN}) approaches the overburden pressure P_C (Z_{MIN}). Since V_{MIN} = V_{NORM}, the effective pressure at the depths Z_{NORM} and Z_{MIN} are the same. P_E (Z_{NORM}) is plotted from the P_C (Z_{MIN}) point as shown in Figure 3-6 and the remaining distance is labeled nP_P. n must be less than 1 since $P_C(Z_{MIN}) \approx P_P$.

6. In abnormal pressure, n is computed from equation (3-8)

$$n=\frac{P_C(Z_{MIN})-P_E(Z_{NORM})}{P_P(Z_{MIN})}=1-\frac{P_E(Z_{NORM})}{P_C(Z_{MIN})}, \tag{3-8}$$

as pore pressure P_P (Z_{MIN}) approximates the confining pressure $P_C(Z_{MIN})$ at depth Z_{MIN}.

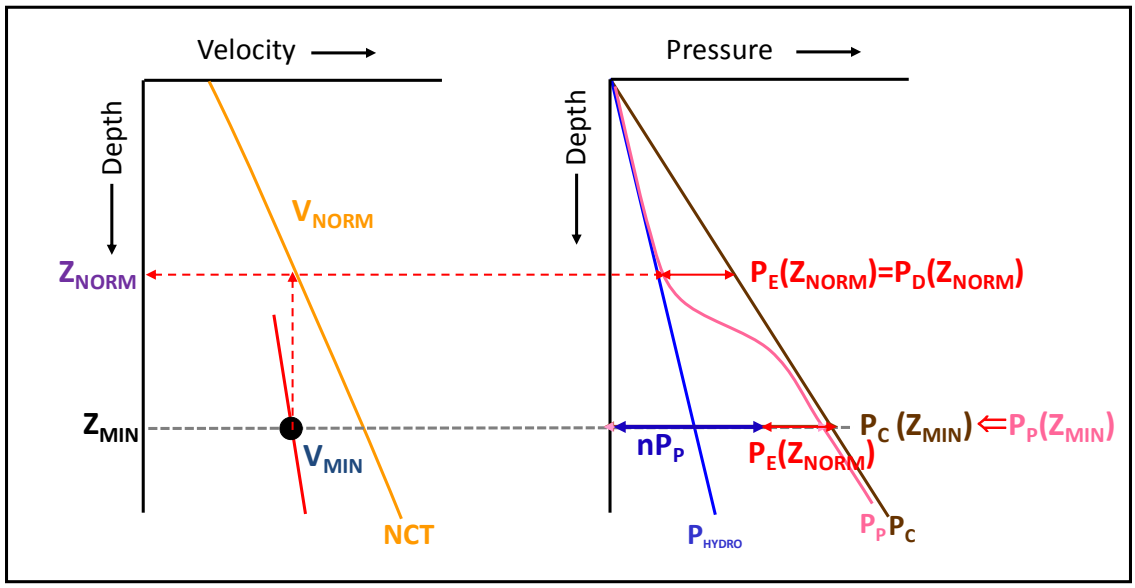

Figure 3-6: Velocity and pressure trends illustrating the method to estimate n.

3.3 Results

3.3.1 Effective pressure coefficient in the six Tracts

The minimum velocity trends and computed effective pressure coefficients in the six different tracts are plotted in Figure 3-7 based on the methodology illustrated in Figure 3-6. In these figures from left to right the first panel is shale minimum velocity, the second panel is effective pressure coefficient n, and the third panel is mud weight, which is shown to indicate the extreme overpressure in the sediment. For these three panels the value is mean value of each 60 m depth, standard deviations are shown on the velocity and mud weight panel. The fourth panel is well numbers to get the average value. The red line in n panel is the average n for each 200 m interval.

The n values in Tracts 1 to 5 are quite close to 0.83. The n values in Tract 6 are more scattered, but most of the values cluster around 0.8. Ebrom et al. (2004) reported n value of 0.88 +/- 0.02 in GOM from 1000 to 6000 m. Our results are consistent with theirs.

Tract 1

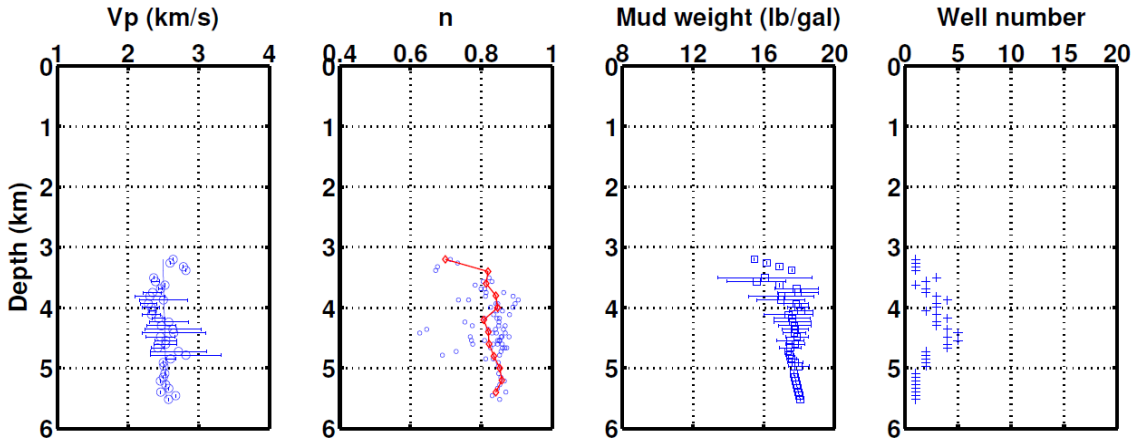

Tract 2

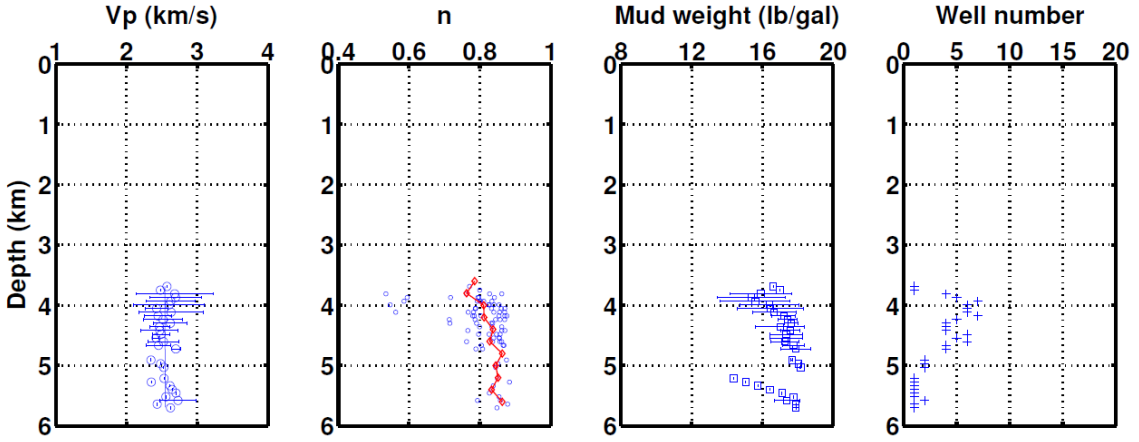

Figure 3-7: Illustration of shale minimum velocity and computed effective pressure coefficients in Tracts 1 to 6. Mud weight trends are indicating the extreme overpressure encountered. The mean and standard deviation for each 60 m depth interval are shown too. The number of well samples used at each depth interval is plotted in the right panel. The red line in n panel is the average n for each 200 m interval.

Tract 3

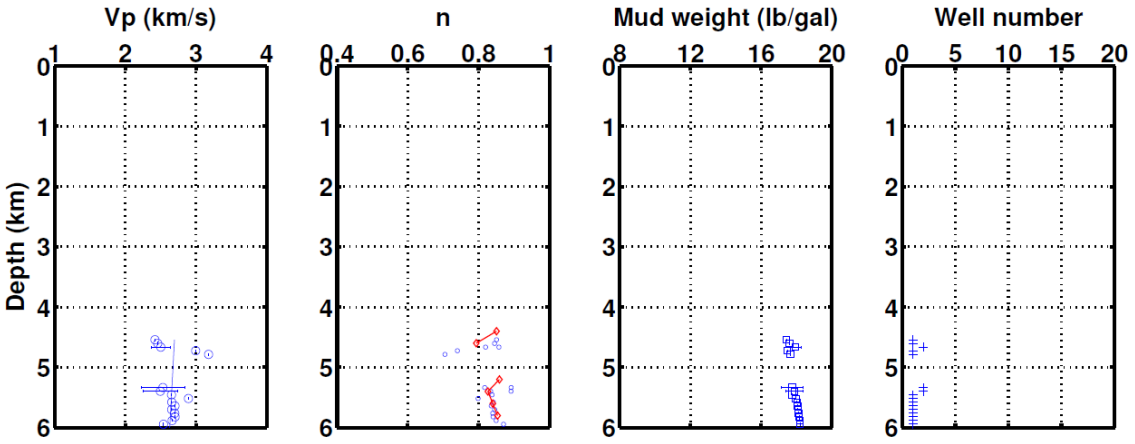

Tract 4

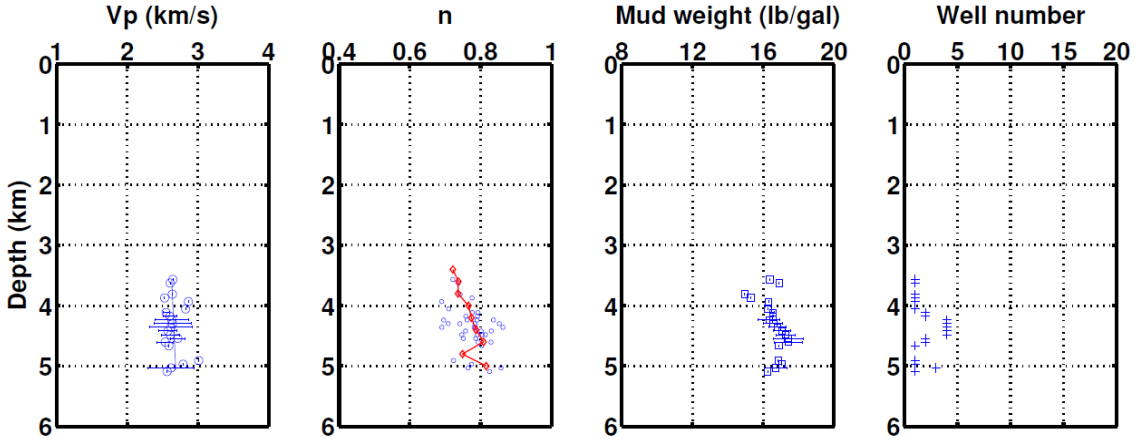

Figure 3-7: (continued) Illustration of shale minimum velocity and computed effective pressure coefficients in Tracts 1 to 6. Mud weight trends are indicating the extreme overpressure encountered. The mean and standard deviation for each 60 m depth interval are shown too. The number of well samples used at each depth interval is plotted in the right panel. The red line in n panel is the average n for each 200 m interval.

Tract 5

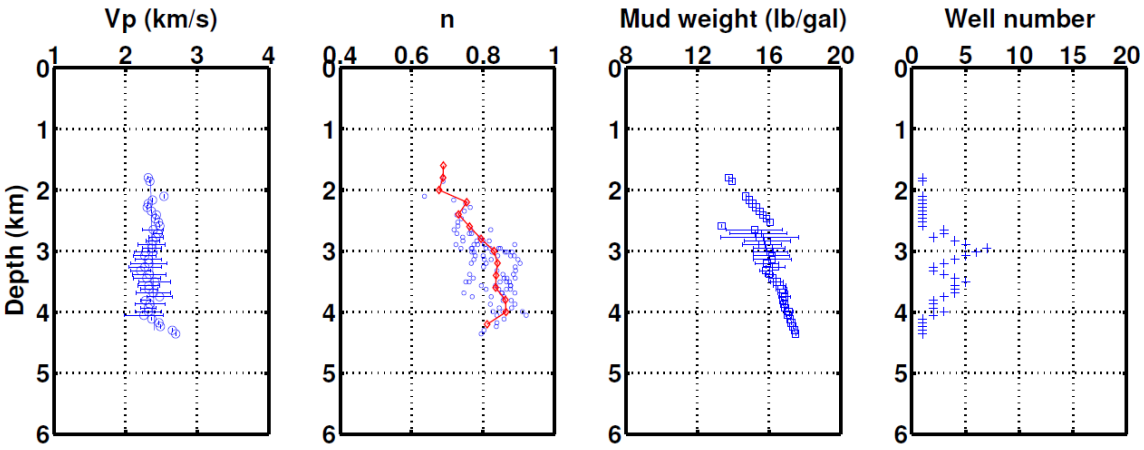

Tract 6

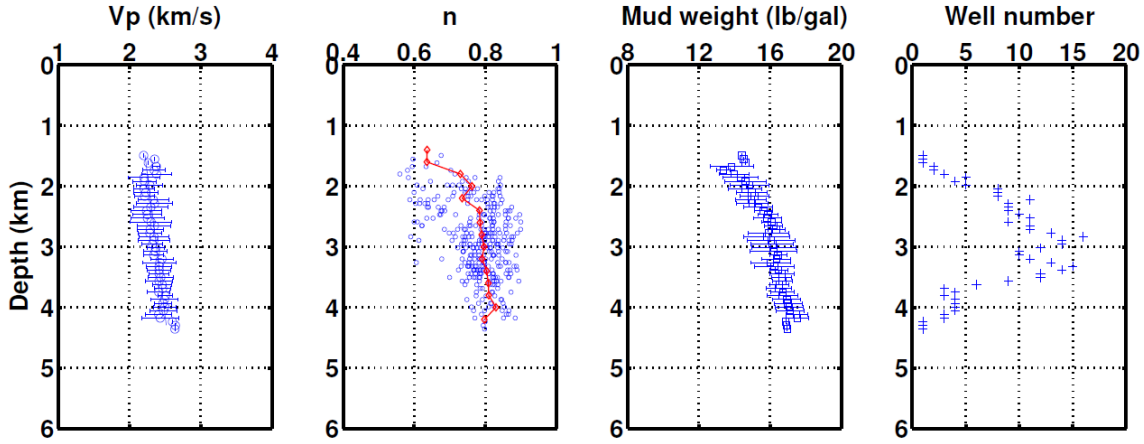

Figure 3-7: (continued) Illustration of shale minimum velocity and computed effective pressure coefficients in Tracts 1 to 6. Mud weight trends are indicating the extreme overpressure encountered. The mean and standard deviation for each 60 m depth interval are shown too. The number of well samples used at each depth interval is plotted in the right panel. The red line in n panel is the average n for each 200 m interval.

3.3.2 Application of n in pore pressure prediction

Using V_P to predict pore pressure is currently an acceptable practice. A key issue in this method is to establish the relationship between velocity and effective pressure of which there are several empirical relations (e.g. Eaton, 1975; Bowers, 1995; Gutierrez et al., 2006). But one shortcoming of empirical methods is the necessity to adjust the parameters for new well locations and usually there is no physical meaning for these adjustments. In this study, we try to avoid empirical methods, and use a theoretical approach that is based on regional and local physical measurements to do pore pressure prediction. The regional measurement of the minimum shale velocity trend has been presented as a method to predict the effective pressure coefficient n. Now, the local shale velocity measurements will be associated with pore pressure predictions.

Referring to Figure 3-8, for an observed velocity in abnormal pressure, V_{OBS}, the corresponding depth Z_{NORM} on the shale velocity NCT is derived from equation (3-9),

$$V_{OBS}=V_0+aZ_{NORM}. \quad (3\text{-}9)$$

The parameters V_0 and a depend on the specific tract where the proposed well is located. See Table 3-2.

After Z_{NORM} is found, the effective pressure $P_E(Z_{NORM})$ at depth Z_{NORM} is computed from equation (3-7). Finally pore pressure P_P can be computed given n in equation (3-10).

$$P_C(Z_{OBS}) = P_E(Z_{NORM})+nP_P(Z_{OBS}). \quad (3\text{-}10)$$

As mentioned, n is often assumed as 1 from surface to total depth. This assumption holds for shallow GOM depths with low vertical stress, where effective pressure P_E equals differential pressure P_D. At greater depths as the sediment becomes cemented and more consolidated, this assumption becomes questionable (Ebrom et al., 2004). As shown in Figure 3-8, at depths in abnormal pressure, P_E is larger than P_D. If P_E is directly subtracted from P_C at observed depth Z_{OBS} and we treat this quantity as pore pressure like most of current empirical pore pressure prediction methods do, pore pressure P_P is underestimated at this depth because the difference between P_C and P_E is actually the quantity of nP_P. At shallow depths, sediment is under hydrostatic pressure, P_E is quite close to P_D. So an n value of one is not a bad assumption in the normal pressure regime (Terzaghi, 1936; Ebrom et al., 2004). But at deeper depths, the P_E and P_D difference is not negligible (Figure 3-8). The parameter n needs to be taken into account to get the real pore pressure, which is higher than the value of P_C-P_E.

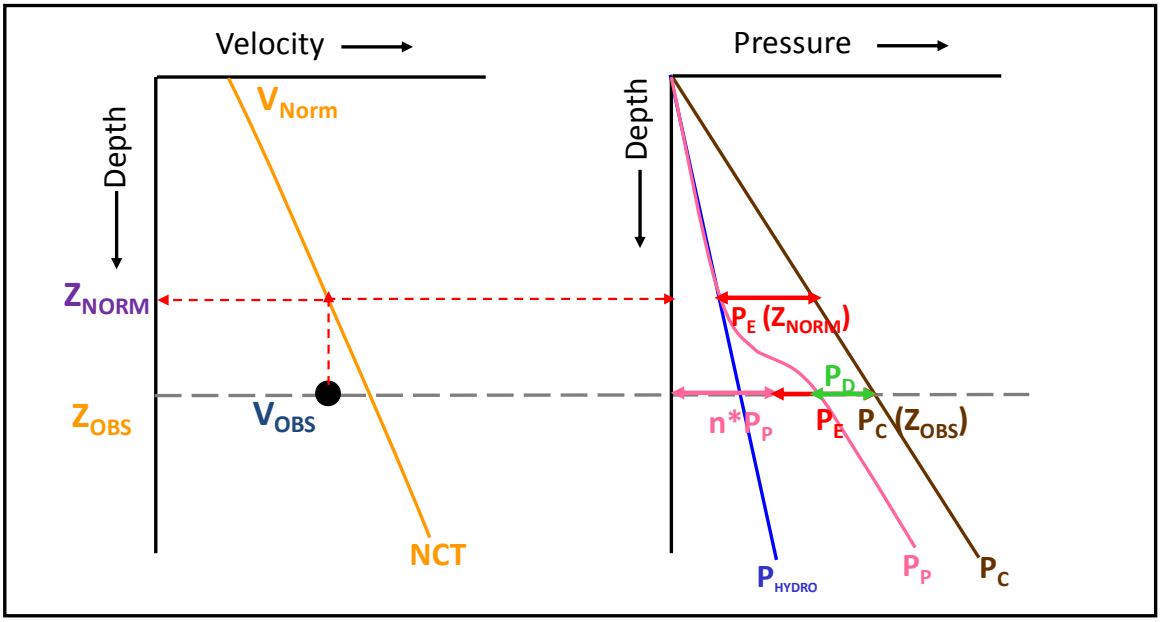

Figure 3-8: Illustration of n importance for pore pressure prediction.

In order to check the pore pressure error caused by a variation in n, we compute the pore pressure by using the method illustrated in Figure 3-8 and compare it with measured pore pressure which is converted from mud weight by equation (3-11):

$$P(MPa)=\text{mud weight } (g/cm^3)\times 0.01\times z\ (m). \quad (3\text{-}11)$$

The left panels in Figure 3-9a show that if we don't consider the variation of n and use the assumption n equals one for all depths, we will get a large discrepancy between predicted pore pressure (green marks) and measured pore pressure (red marks), especially in the overpressure section. But if we take the calibrated n, which is 0.83 from section 3.3.1, into the pore pressure computation, we get a nice match (right panels in Figure 3-9a). The results as illustrated in Figure 3-9a are basically duplicated in Figures 3-9b and 3-9c. In short, our results show the necessity to include a calibrated n when predicting pore pressure in the GOM, especially in geopressure zones. In Figures 3-9a, b, and c, the following holds:

- Blue solid line is overburden pressure $P_{C.}$
- Cyan solid line is hydrostatic pressure P_{HYDRO}.
- Red circle is mud weight converted pore pressure in normal pressure zone called observed pore pressure, P_P-obs-normal; while, red square is mud weight converted pore pressure in abnormal pressure regime, P_P-obs-abnormal.

- Green circle is predicted pore pressure from this study in normal pressure zone, P_P-pred-normal; while green square is predicted pore pressure in abnormal pressure zone, P_P-pred-abnormal.
- The pressure plots in the left panel assume n equals one at all depths. The pore pressure plots in the right panel assume n equals one in normal pressure zone and n equals 0.83 in abnormal.

Tract 1

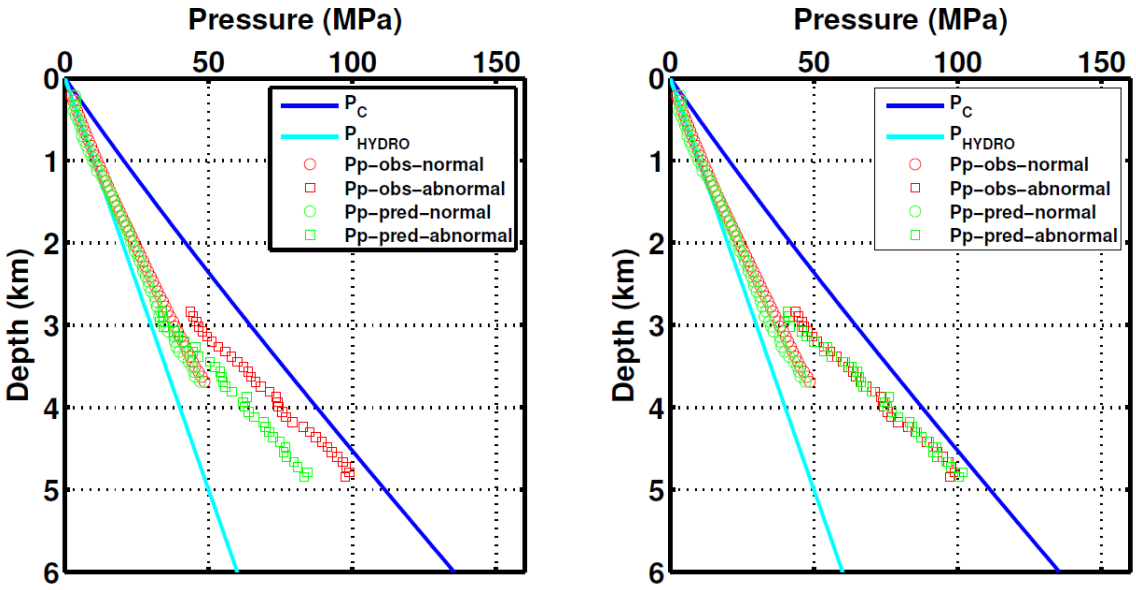

Tract 2

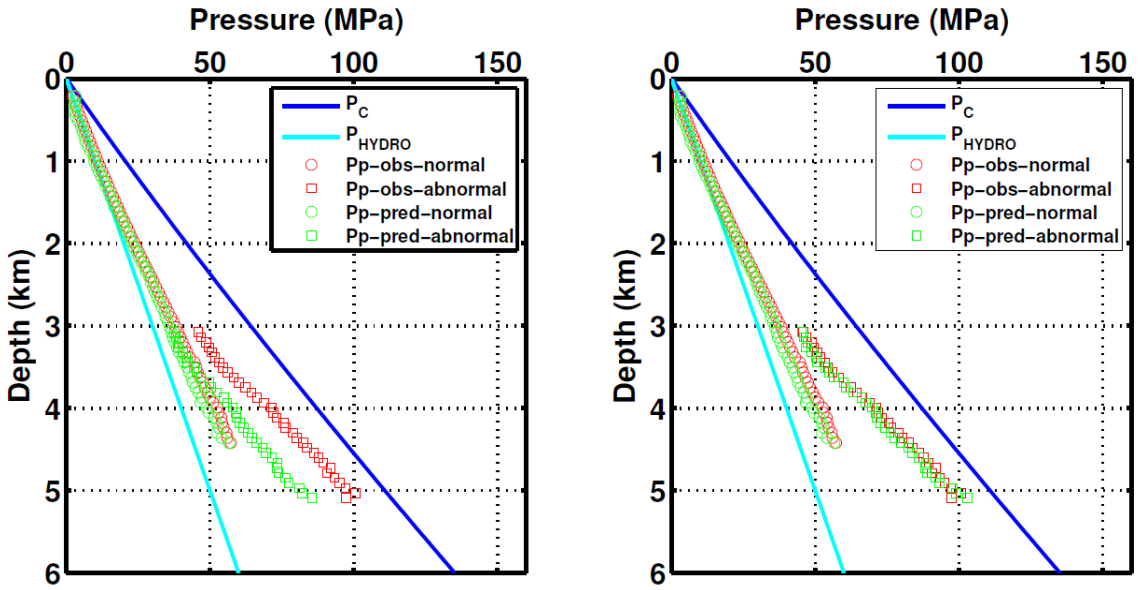

Figure 3-9a: Comparison of pore pressure prediction without (left panels) and with (right panels) calibration of n in Tracts 1 and 2.

Tract 3

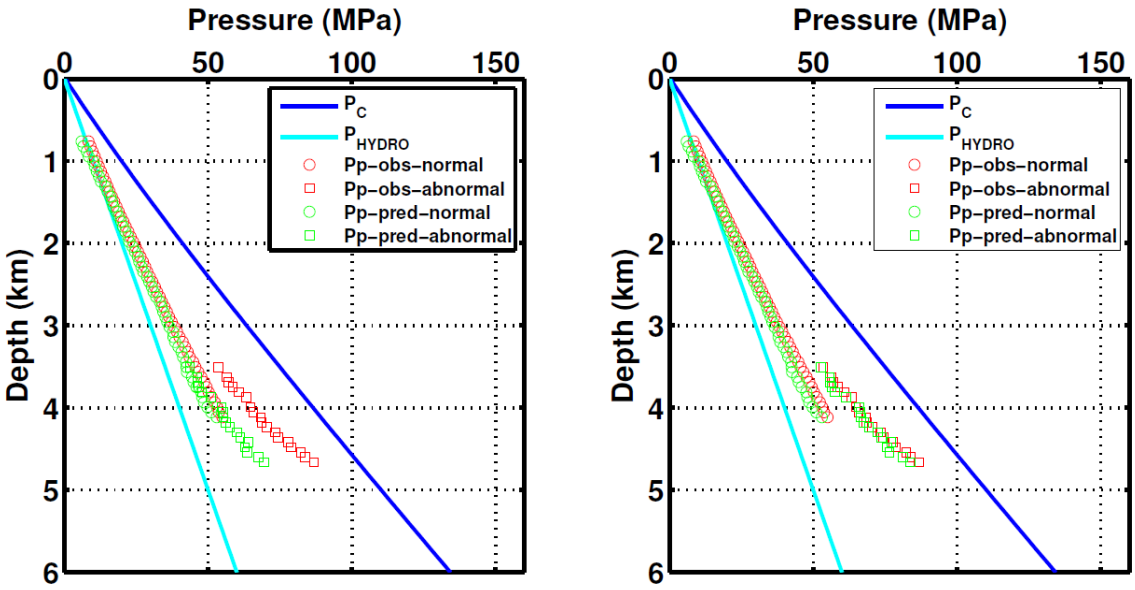

Tract 4

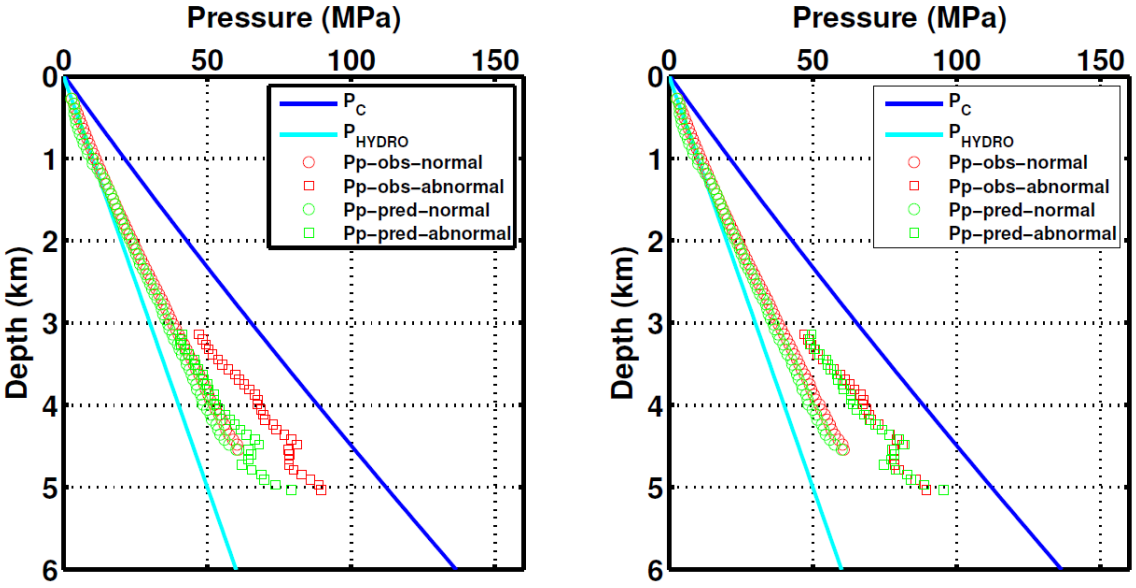

Figure 3-9b: Comparison of pore pressure prediction without (left panels) and with (right panels) calibration of n in Tracts 3 and 4.

Tract 5

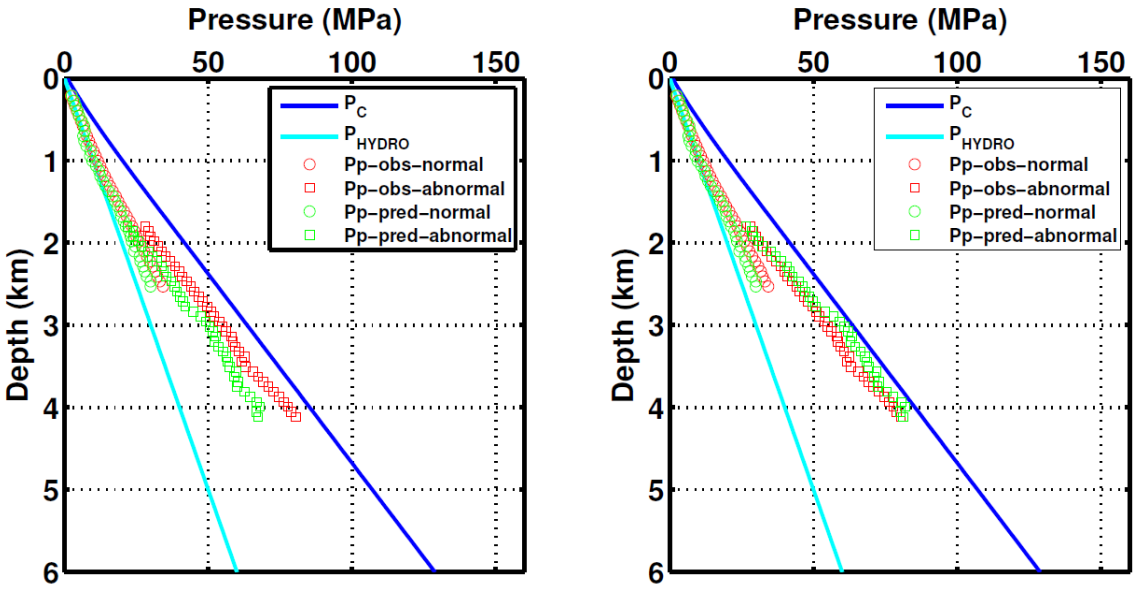

Tract 6

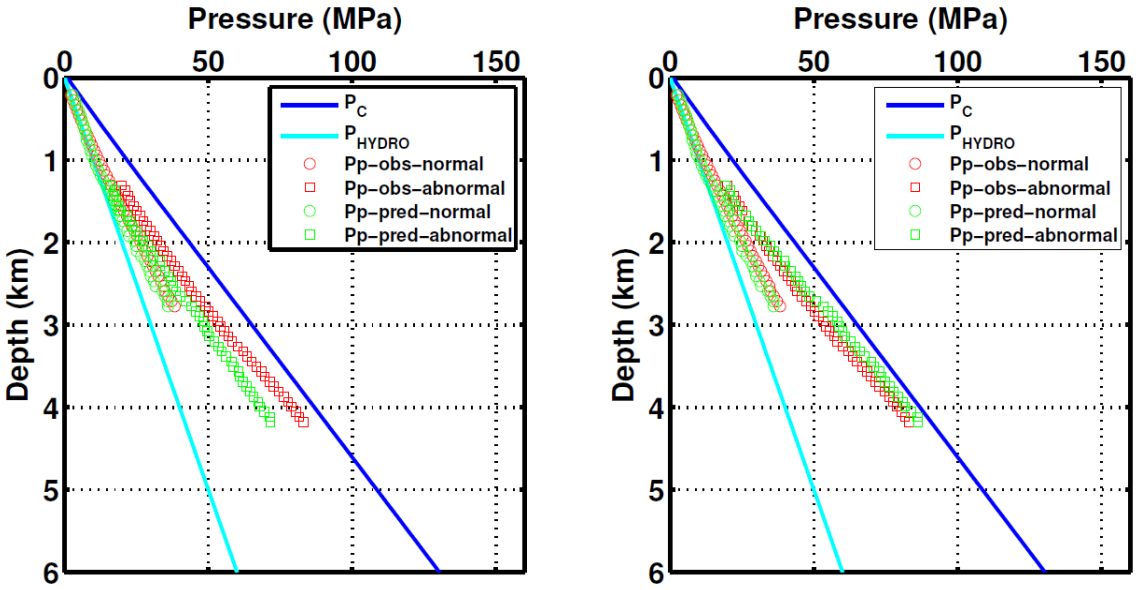

Figure 3-9c: Comparison of pore pressure prediction without (left panels) and with (right panels) calibration of n in Tracts 5 and 6.

3.4 Discussion

3.4.1 Comparison between normal compaction trends

As NCT plays an important role in deriving n in this study, it is necessary to compare our established NCT with the global NCT. Eberhart-Phillips et al. (1989) established a relationship between seismic velocity and porosity, clay content, and effective pressure (or differential pressure in their study P_D), which is widely used as a normal compaction trend for many basins. From their research, P-wave velocity is predicted from porosity, clay volume, and differential pressure as

$$\text{Vp}=5.77-6.94\phi-1.73\sqrt{C}+0.446(\text{P}_E-e^{-16.7P_E}), \tag{3-12}$$

where V_P is P-wave velocity in km/s, ϕ is porosity (fraction), P_E is effective pressure or differential pressure in Kbar, which is calculated from equation (3-7). Porosity is computed from the mass balance equation as

$$\phi=\frac{\rho_b-\rho_m}{\rho_w-\rho_m}, \tag{3-13}$$

where ρ_b is bulk density; ρ_m, matrix density; and ρ_w, water density. The densities of 2.65 g/cm^{3}and 1.07 g/cm^{3}were used for ρ_m and ρ_w respectively.

We compare our normal compaction trend with the Eberhart-Phillips et al. (1989) empirical velocity from differential pressure relationship, which are taken as global NCT for the 6 tracts. Results are shown in Figure 3-10. We see an interesting feature. At

shallow depths, the predicted V_P by Eberhart-Phillips et al. model matches very well with our adjusted NCT, but beyond 2000 m V_P predicted by Eberhart-Phillips et al. model is much closer to the original NCT. As we discussed early, in GOM where rock samples in Eberhart-Phillips et al. model are from, overpressure actually builds up at approximately 2000 m (Shaker, 2007). We conjecture that is why their predicted V_P matched our original measured V_P.

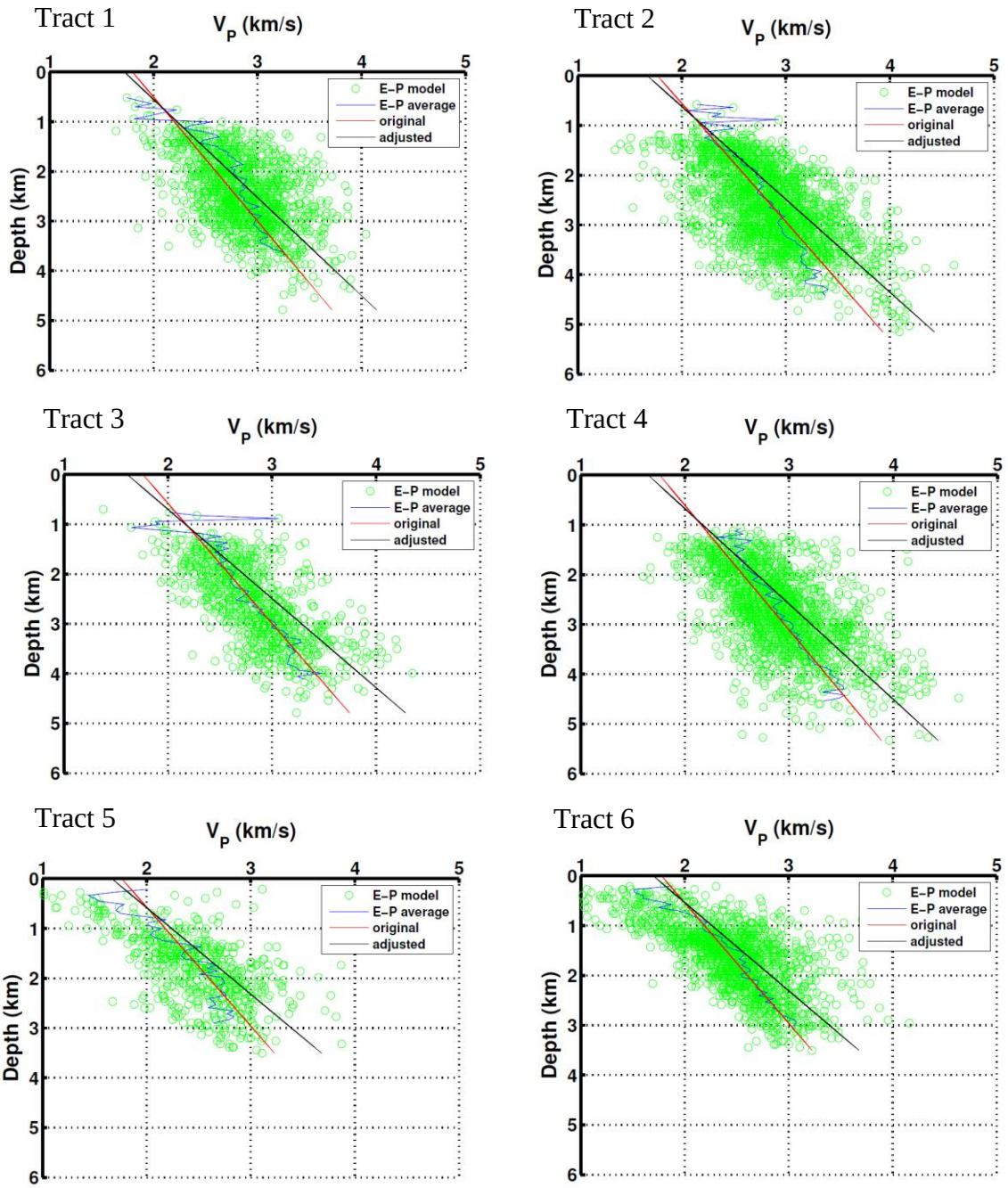

Figure 3-10: Comparison of adjusted normal compaction trend (black) and original NCT (red) with Eberhart-Phillips et al. (1989) computed NCT (E-P model in the figure). The green dots are Eberhart-Phillips et al. velocity predictions for individual 60 m samples, while the blue line represents average values.

3.4.2 Mud weight error

In Section 3.3.2, mud weight is used as an approximation for pore pressure, because it is the only parameter which provides a continuous pore pressure profile. However, Dutta and Khazanehdari (2006) noted that the mud weight used during drilling is typically about 0.5 lb/gal higher than the true formation pressure. In this mud weight error analysis, we subtract 0.5 lb/gal from the interpolated mud weight for pore pressure calculation and compare our predicted pore pressure with mud weight converted pore pressure again. Results are shown in Figure 3-11. In these figures, the following holds:

- Blue solid line is overburden pressure $P_{C.}$
- Cyan solid line is hydrostatic pressure P_{HYDRO}.
- Red circle is mud weight (with 0.5 lb/gal subtracted) converted pore pressure in normal pressure zone (P_P-obs-normal); while, red square is mud weight converted pore pressure in abnormal pressure regime (P_P-obs-abnormal).
- Green circle is predicted pore pressure from this study in normal pressure zone (P_P-pred-normal); while green square is predicted pore pressure in abnormal pressure zone (P_P-pred-abnormal).
- Left panel assumes n equals one for all depths; while right panel assumes n equals one in normal pressure zone and n equals 0.83 in abnormal.

In Tracts 1-4 (northern) with subtracted mud weight of 0.5 lb/gal, there is still a need to include n into pore pressure prediction for the abnormal pressure zones. In Tracts 5 and 6

(southern), the prediction is better, but we still notice in deeper depths, the discrepancy starts to increase, which means as the sediments get more and more compacted and consolidated, the influence of n becomes more critical.

Tract 1

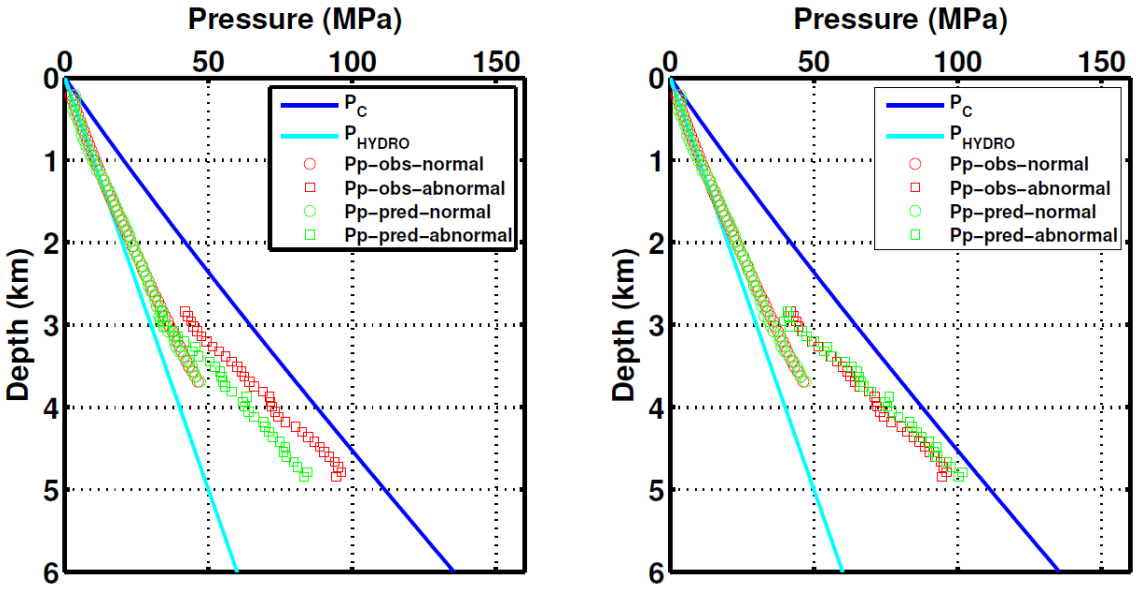

Tract 2

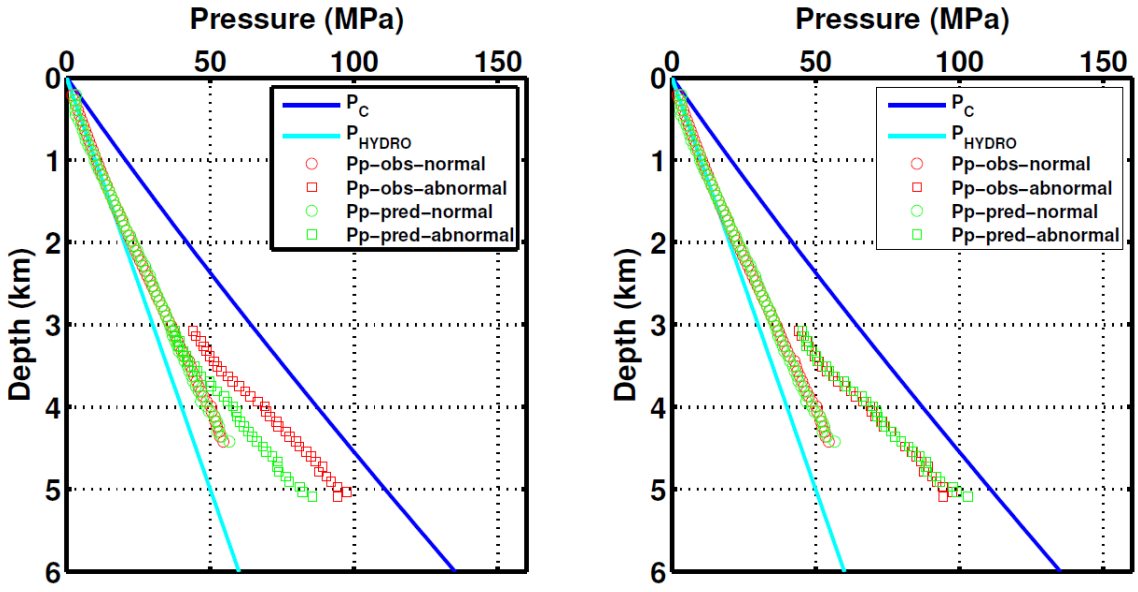

Figure 3-11a: Comparison of pore pressure prediction without (left panels) and with (right panels) calibration of n in Tracts 1 and 2.

Tract 3

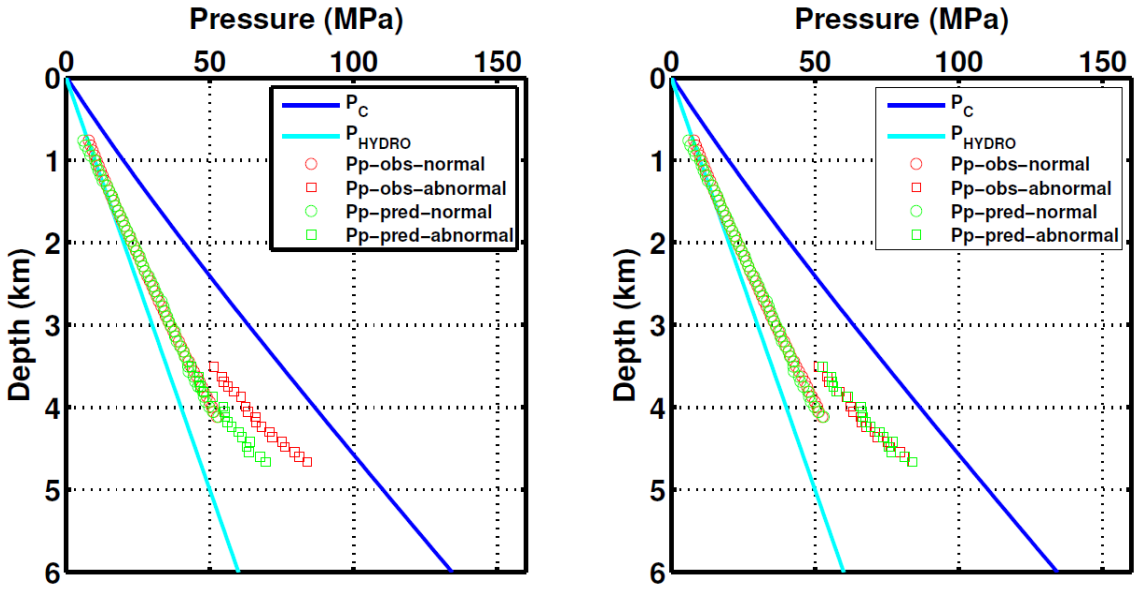

Tract 4

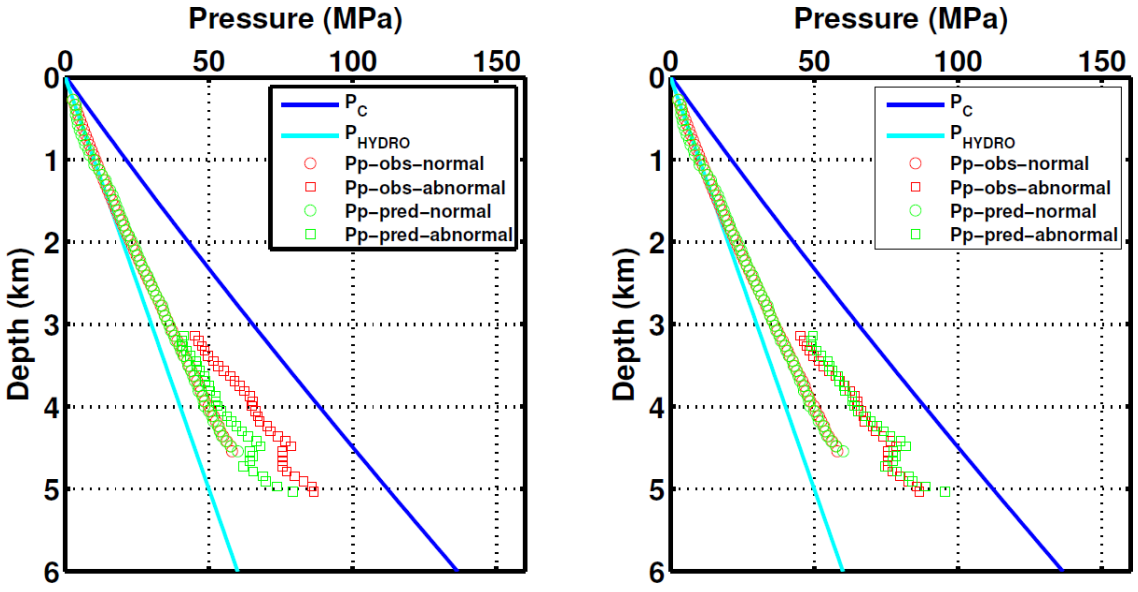

Figure 3-11b: Comparison of pore pressure prediction without (left panels) and with (right panels) calibration of n in Tracts 3 and 4.

Tract 5

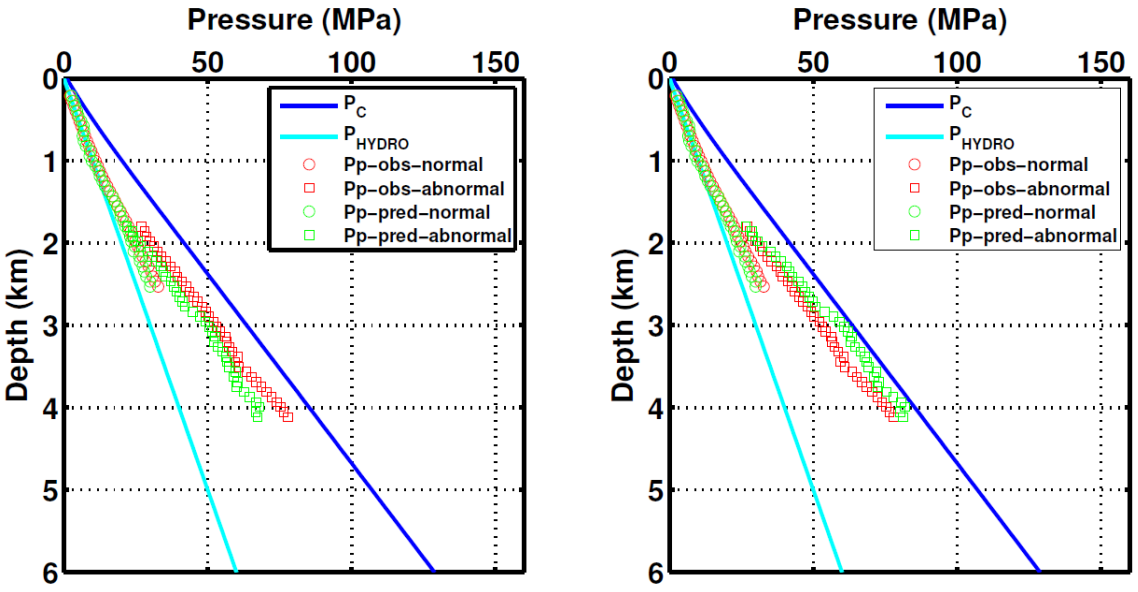

Tract 6

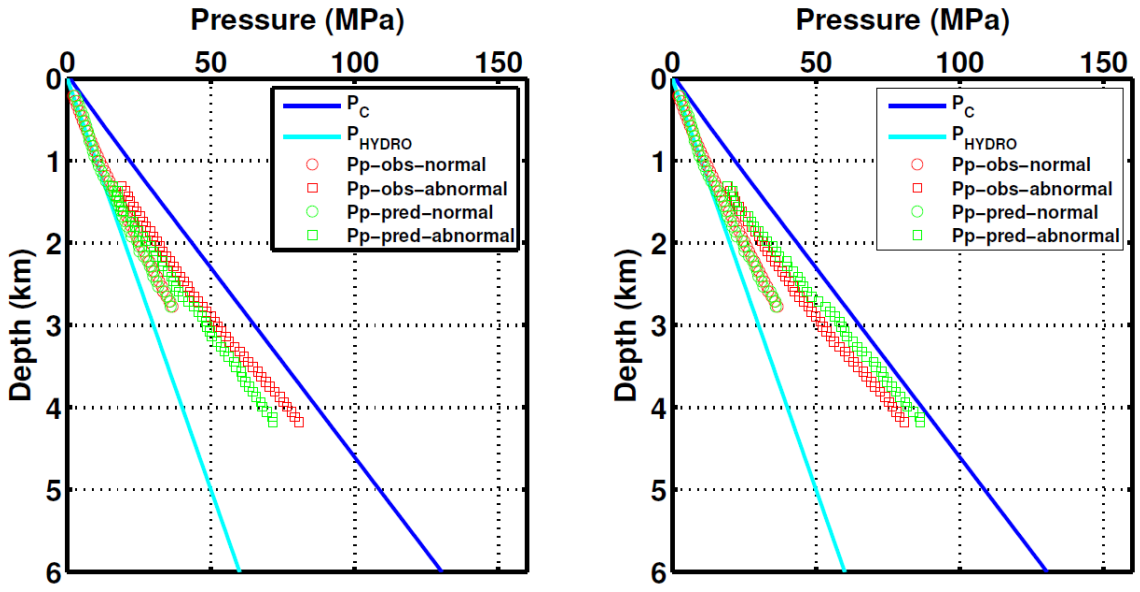

Figure 3-11c: Comparison of pore pressure prediction without (left panels) and with (right panels) calibration of n in Tracts 5 and 6.

3.4.3 Dilemma of empirical coefficient adjustment

In the current industry, there are several different ways to predict pore pressure. Gutierrez et al. (2006) made a detailed review of those methods and compared their accuracy. One general category of empirical transforms relates a geophysical property, such as seismic interval velocity, resistivity, or impedance to pore pressure. Eaton's (1975) method expressed in equation 3-14 and illustrated in Figure 3-8 belongs in this category. In this equation, exponent E represents the sensitivity of velocity to effective pressure. Adjustment of E, based on an offset well, is often done to seek a good match between predicted and measured pore pressure.

$$\frac{P_E(Z_{OBS})}{P_{E\_NORM}(Z_{OBS})} = \left(\frac{V_{OBS}}{V_{NORM}(Z_{OBS})} \right)^E . \tag{3-14}$$

P_E (Z_{OBS}) is the effective pore pressure corresponding to the observed velocity V_{OBS} at depth Z_{OBS}. This is the desired quantity for pore pressure prediction.

Unfortunately, shale velocity even above the onset of GP as shown in Figures 3-3, and 3-4 is slightly overpressured (Shaker, 2007). This complication, however, has been addressed by a correction factor introduced earlier, which is the NCT adjusted depth. The exponent E describes the sensitivity of velocity to effective pressure and is normally calibrated to specific study areas. Katahara (2003) refined Eaton's formula by introducing the shale P-wave velocity at the mud line, V_{MUD}, to yield

$$\frac{P_E(Z_{OBS})}{P_{E\_NORM}(Z_{OBS})} = \left(\frac{V_{OBS}-V_{MUD}}{V_{NORM}(Z_{OBS})-V_{MUD}} \right)^K , \tag{3-15}$$

where the exponent K requires local calibration similar to Eaton's exponent. A schematic of Katahara's equation is shown in Figure 3-12. The K value has a significant impact on the results of $P_E(Z_{OBS})$, which equals $P_E(Z_{NORM})$ in the plot.

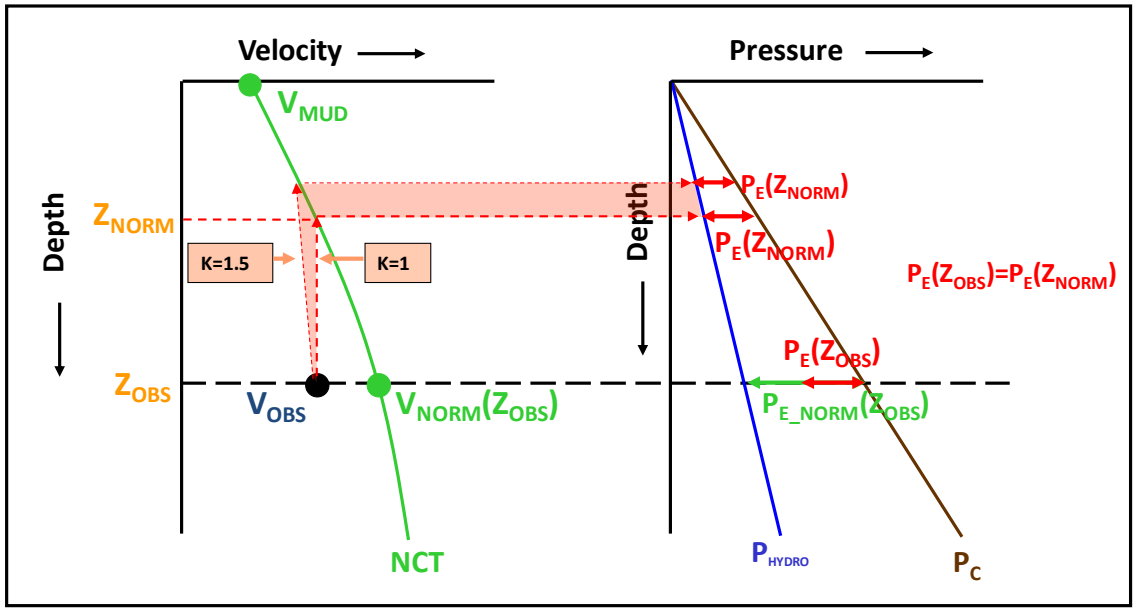

Figure 3-12: Illustration of Katahara's velocity-effective pressure transform.

In this study, two models are tested, one assumes K=1, the other assumes K=1.5. For Tract 1, a K=1 was employed and a linear relationship exists between effective pressure and V_P in the normal pressure zone (see Figure 3-13). Since effective pressure is linear with depth and our observations are that velocity in normal pressure is linear with depth, then a K=1 is a reasonable mathematical setting. But the predicted pore pressure has obvious discrepancy from measured pore pressure in abnormal pressure without considering n.

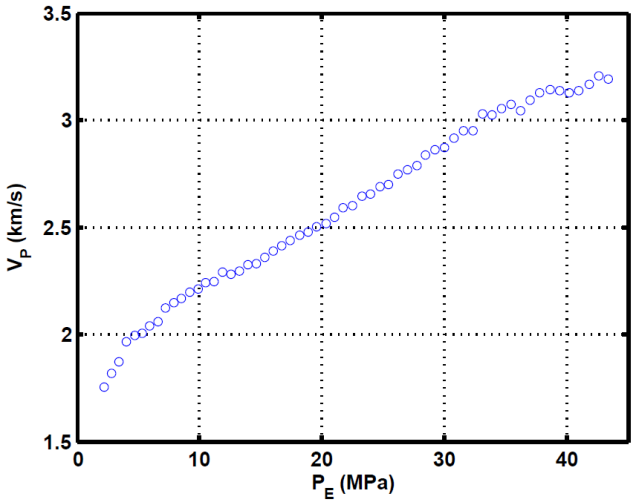

Figure 3-13: Effective pressure and V_P in normal pressure zone of Tract 1.

Figure 3-14 shows that if we don't consider the variation of n when Katahara's exponent, K=1, and the assumption n=1 for all the depths is employed, then a large discrepancy between predicted pore pressure and measured pore pressure results, especially in the overpressure section. But if we take the calibrated n, which is 0.83, into the pore pressure computation, a better match is obtained. Again, our results show the necessity to include calibrated n in the pore pressure predictions in the GOM. The data annotation is similar to that used in Figures 3-9 and 3-11.

Tract 1

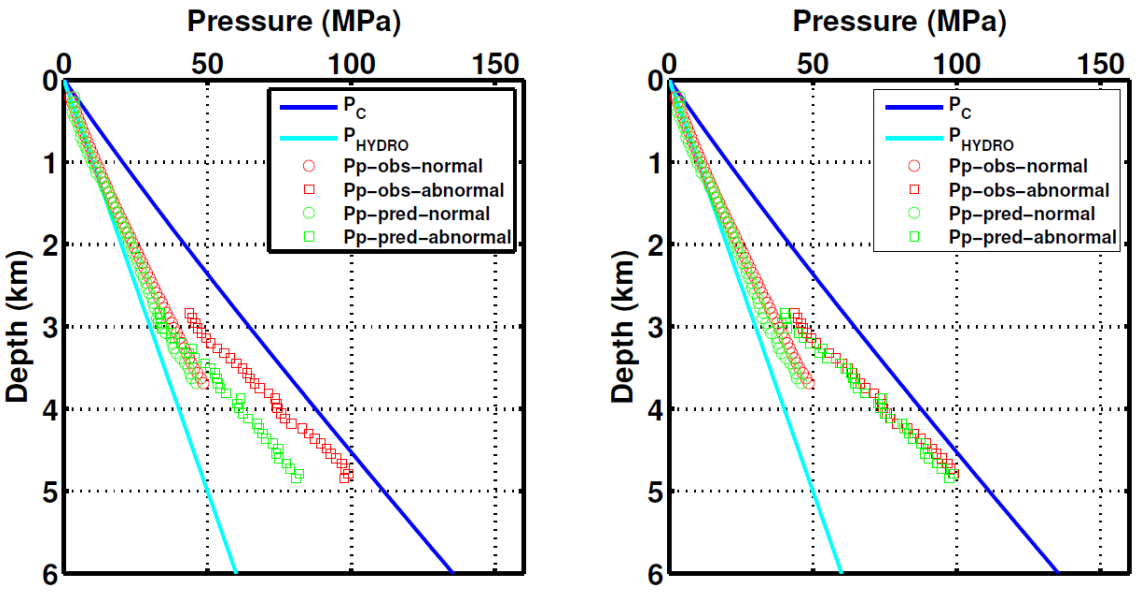

Tract 2

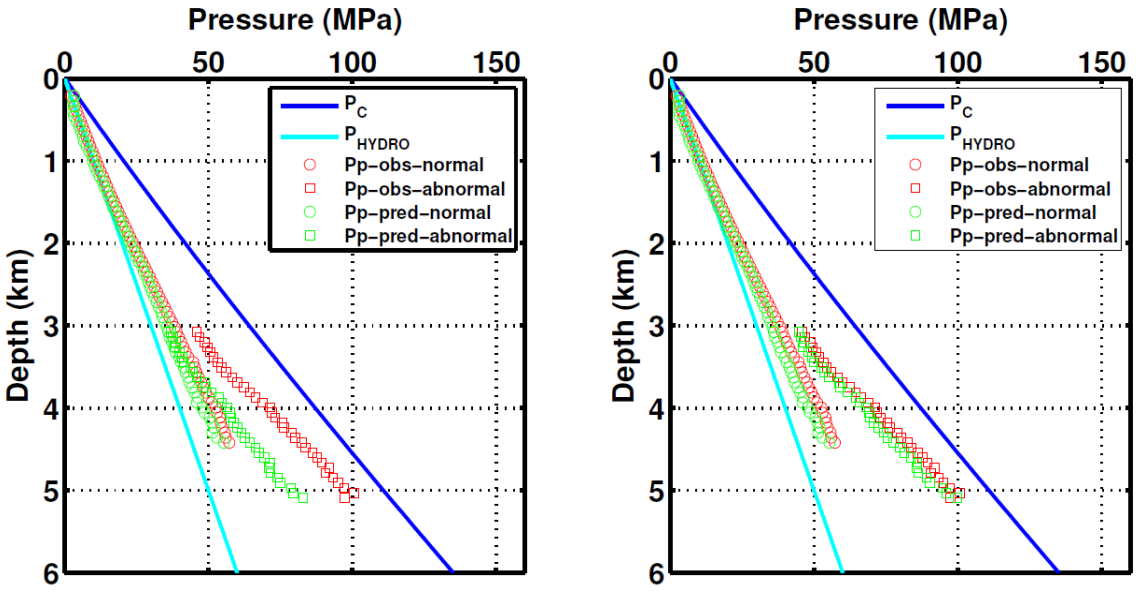

Figure 3-14a: Katahara exponent K=1 comparison of pore pressure prediction without (left panels) and with (right panels) calibration of n in Tracts 1 and 2.

Tract 3

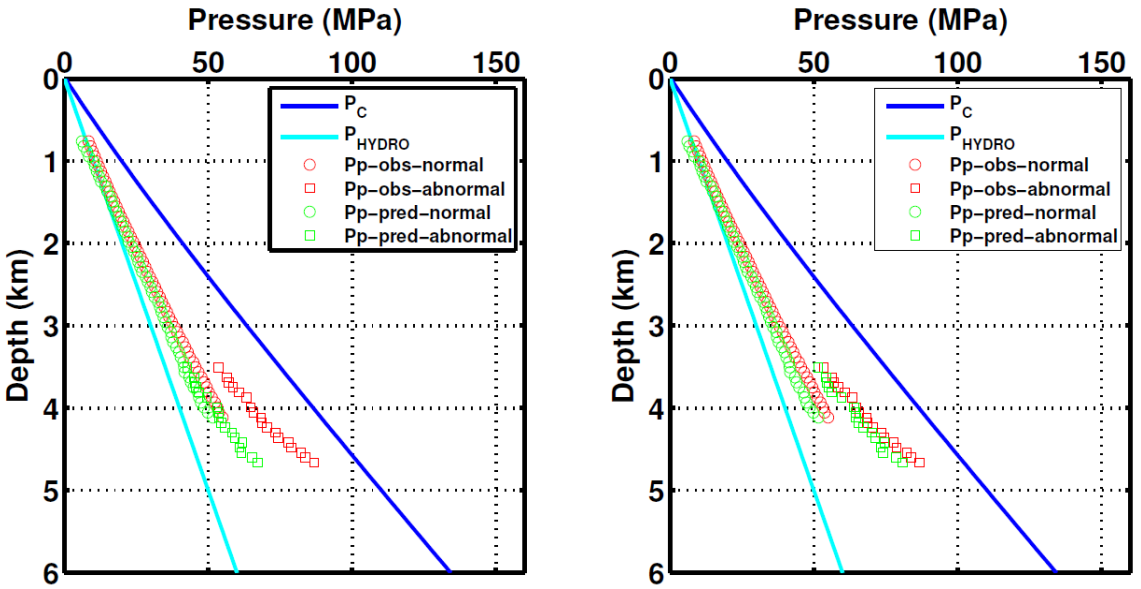

Tract 4

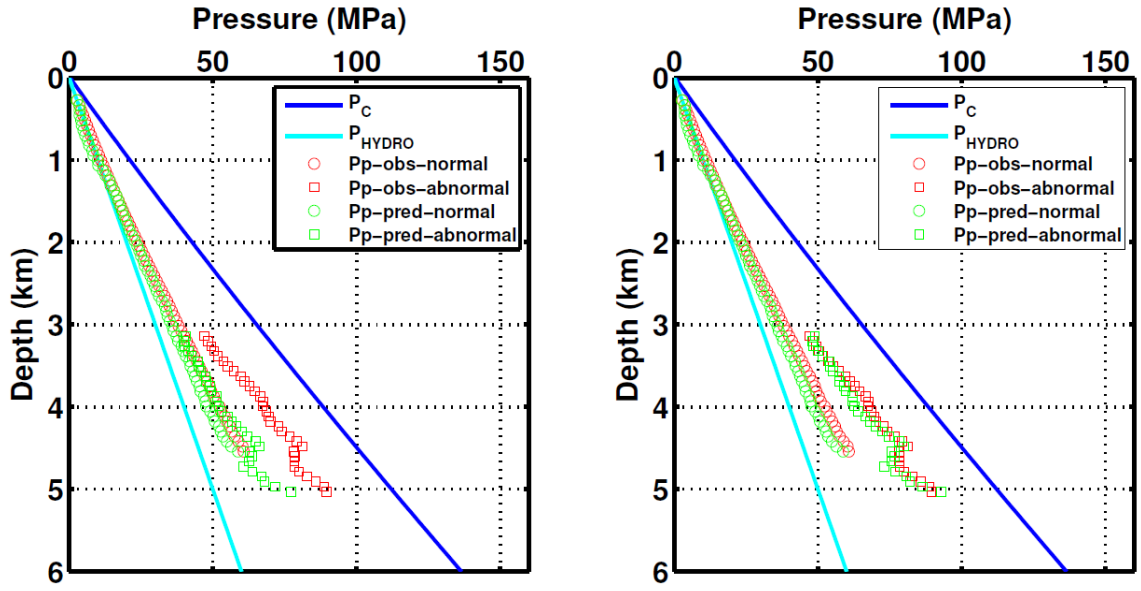

Figure 3-14b: Katahara exponent K=1 comparison of pore pressure prediction without (left panels) and with (right panels) calibration of n in Tracts 3 and 4.

Tract 5

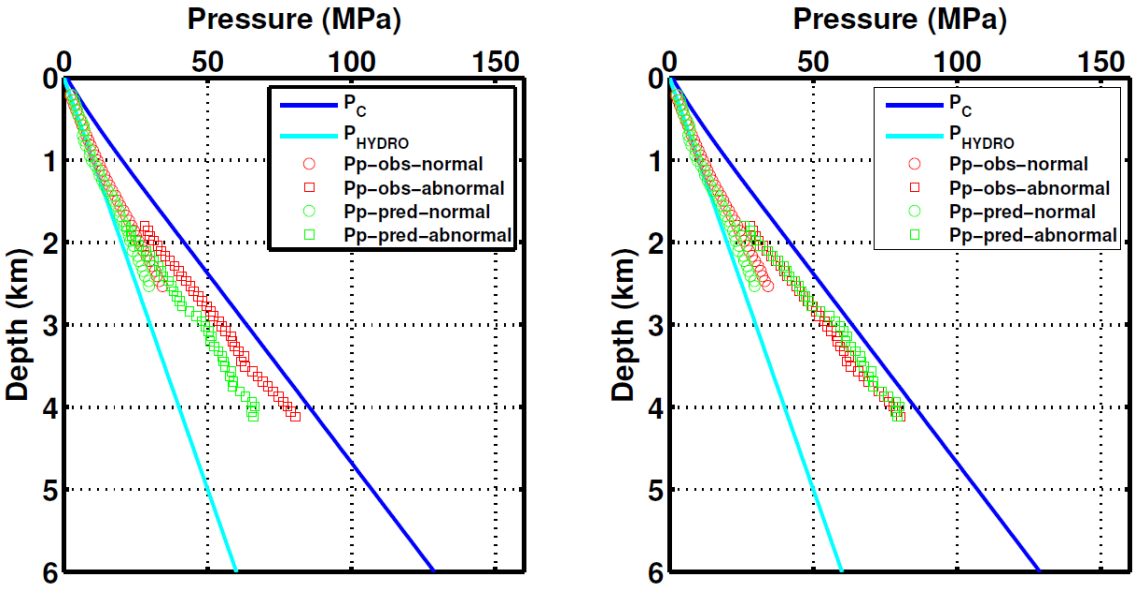

Tract 6

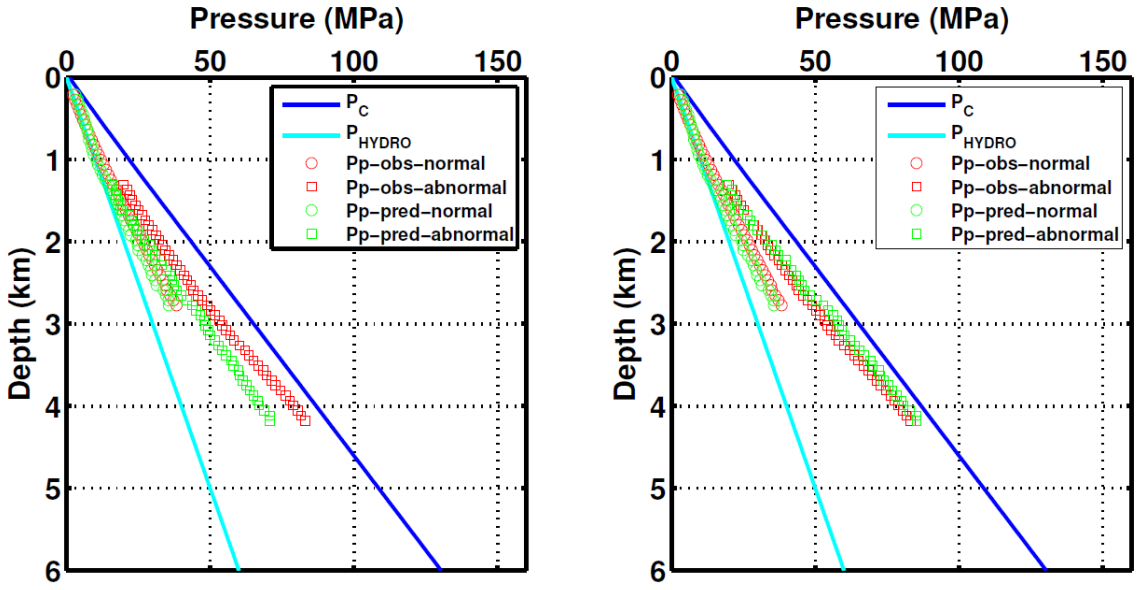

Figure 3-14c: Katahara exponent K=1 comparison of pore pressure prediction without (left panels) and with (right panels) calibration of n in Tracts 5 and 6.

We did one more test on the value for the empirical exponent K. The exponent K in equation (3-15) is changed to 1.5, which is often used (by personal communication with Keith Katahara) and compared to the predicted pore pressure and pore pressure from mud weight. The simulated results are shown in Figures 3-15a, b, and c. Again, the data annotation is similar to that used in Figures 3-9a, b, and c. With K=1.5, a reasonable match between predicted pore pressure and converted mud weight exists without considering the influence of n especially in southern area, Tracts 5 and 6. So here is the dilemma, should empirical parameters be adjusted to get reasonable results or should the physical meaning behind empirical coefficients be sought? The key issue here is to decide what is the more robust parameter to carry the sensitivity property of velocity to pore pressure prediction? In Eaton's or Katahara's equation, the sensitivity is placed on the exponent E or K, but in this study we keep E or K constant, and put the sensitivity to n. Which makes more sense? In order to answer this question, we look at the relationship between effective pressure and velocity in the normal pressure zone. The effective pressure is computed from equation (3-7) in normal pressure section of Tract 1, which is shown in Figure 3-13. It is apparent from this figure that the effective pressure has a linear relationship with V_P in normal pressure zone, so assuming K equals one makes sense physically. Sometimes adjustments of E in different basins can go unbelievable high up to 12 in order to match the field data.

Tract 1

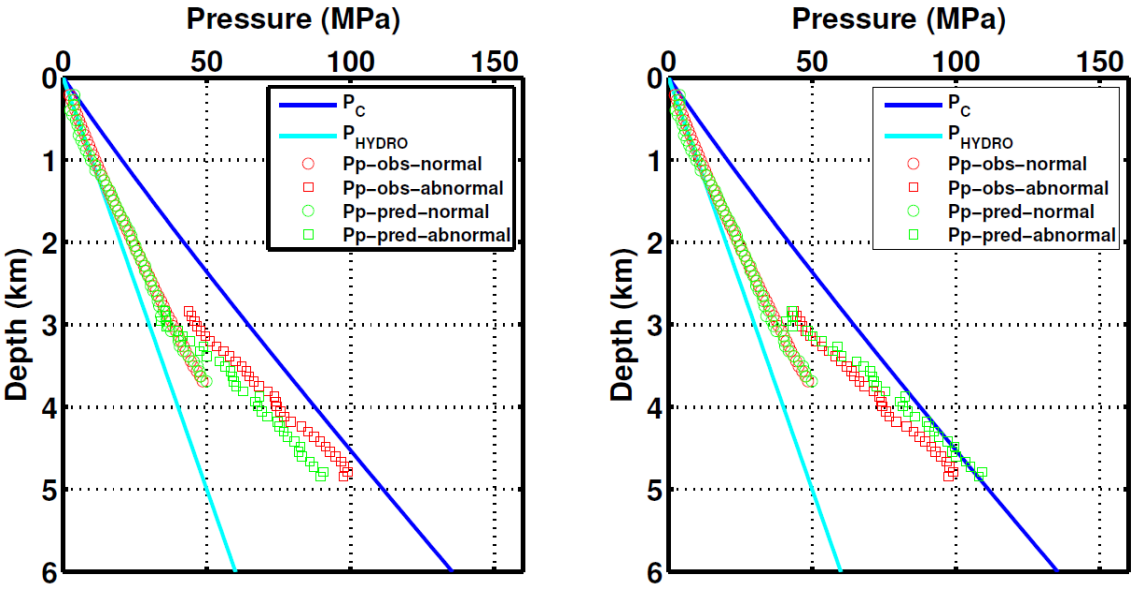

Tract 2

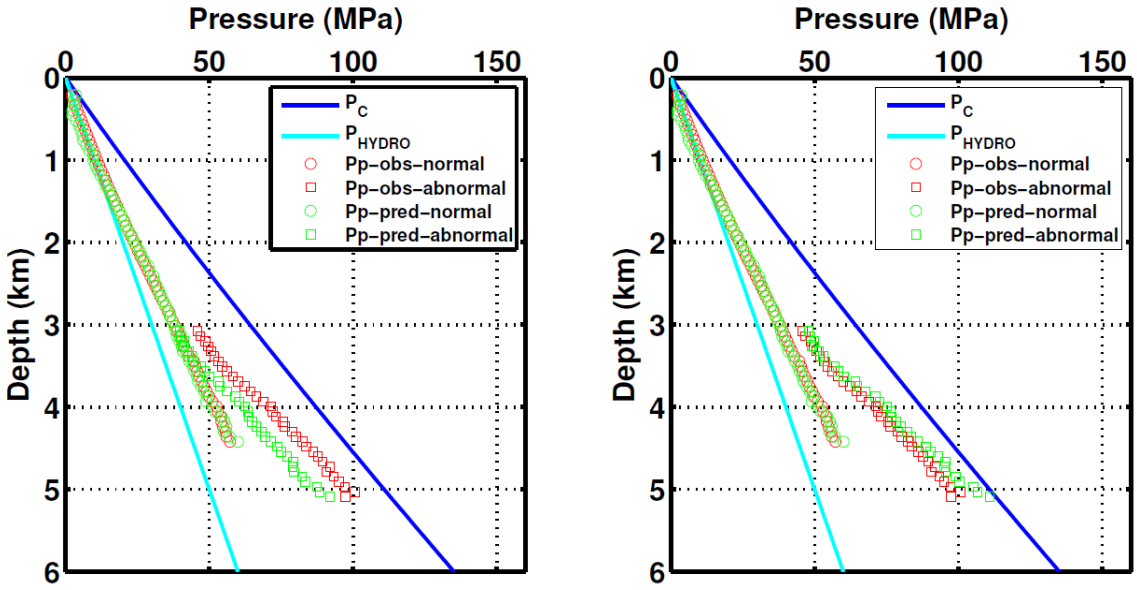

Figure 3-15a: Katahara exponent K=1.5 comparison of pore pressure prediction without (left panels) and with (right panels) calibration of n in Tracts 1 and 2.

Tract 3

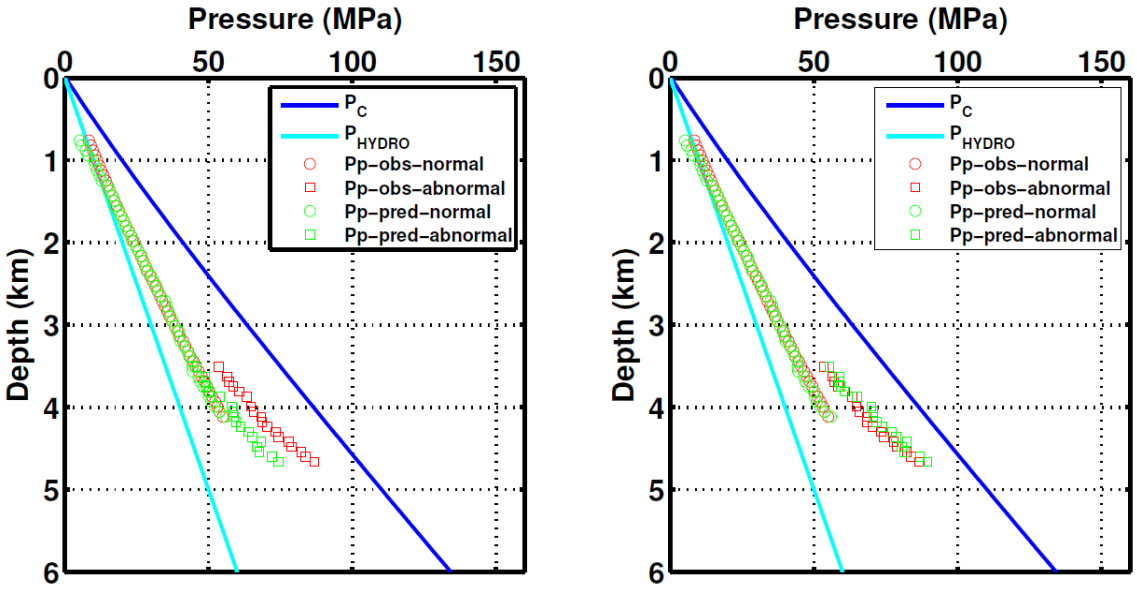

Tract 4

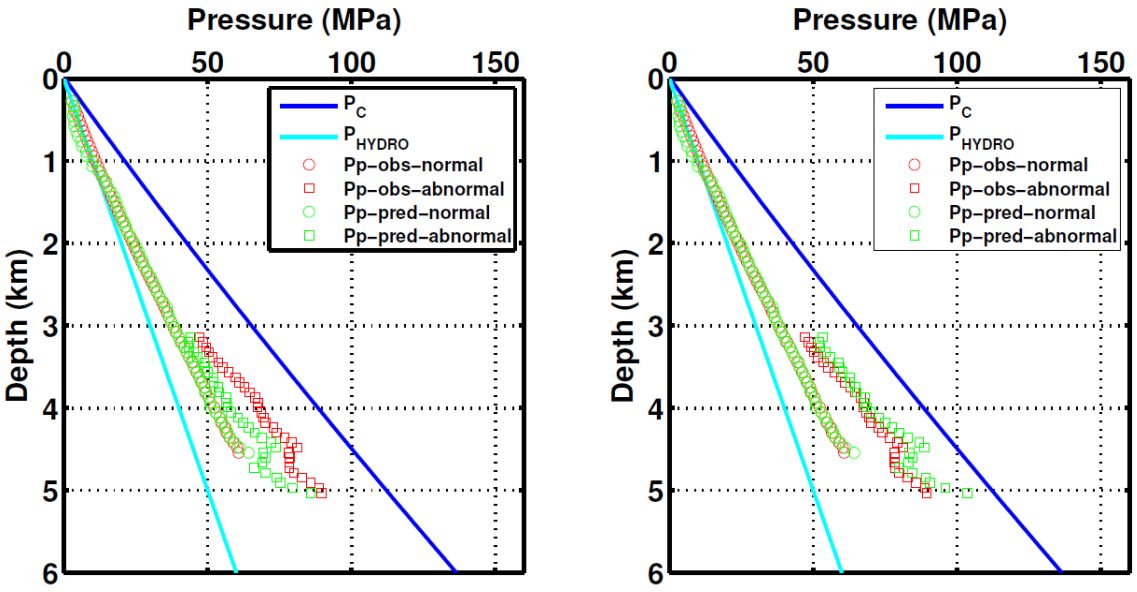

Figure 3-15b: Katahara exponent K=1.5 comparison of pore pressure prediction without (left panels) and with (right panels) calibration of n in Tracts 3 and 4.

Tract 5

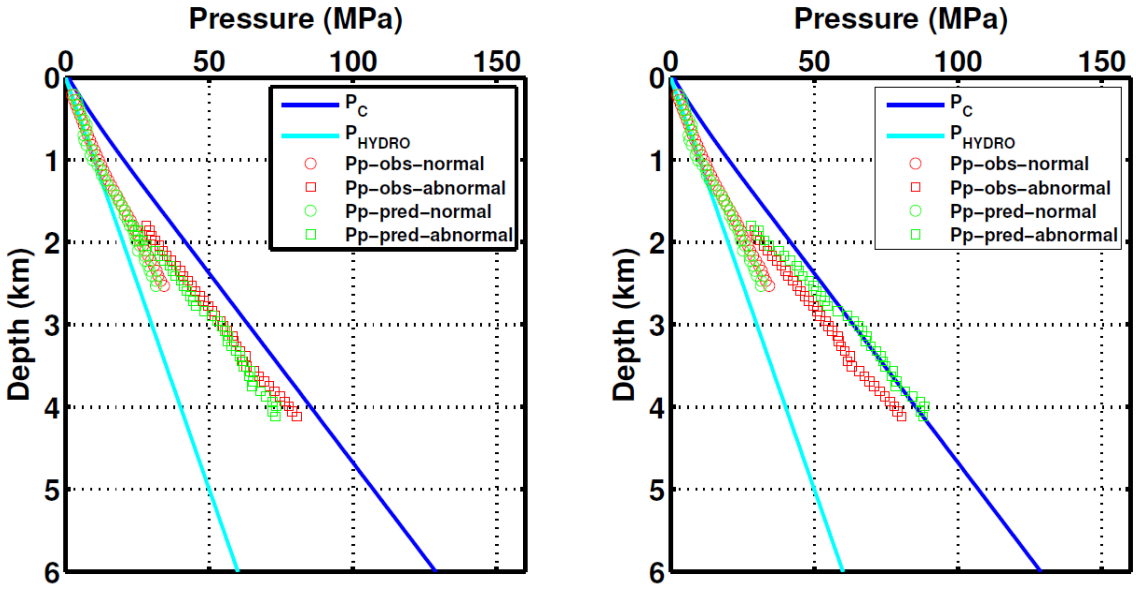

Tract 6

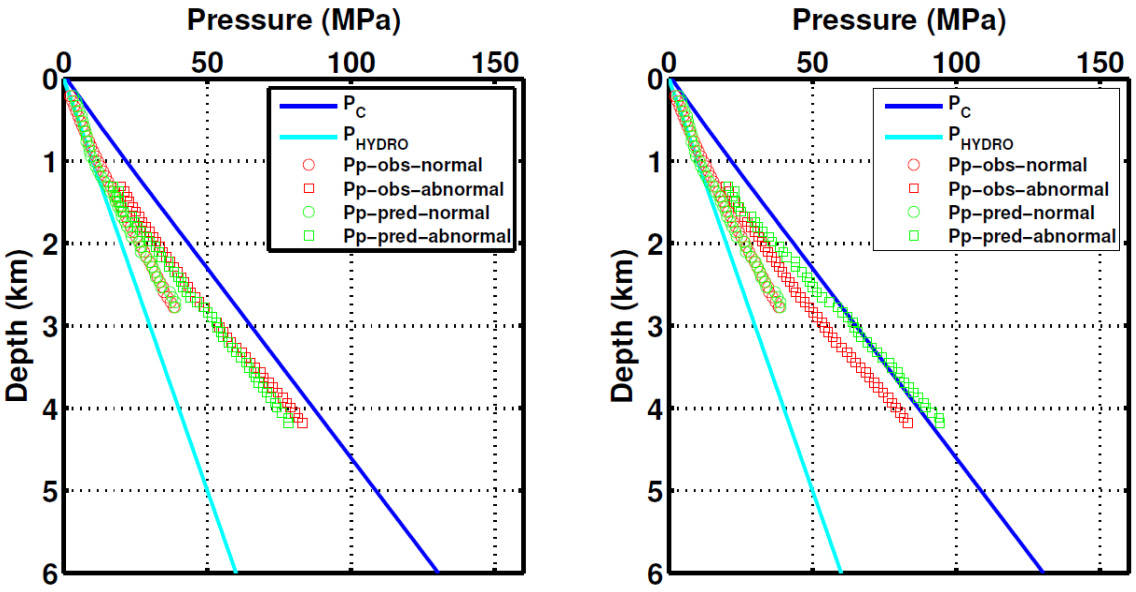

Figure 3-15c: Katahara exponent K=1.5 comparison of pore pressure prediction without (left panels) and with (right panels) calibration of n in Tracts 5 and 6.

3.5 Summary

Corresponding to different pressure regimes, density displays different trends, which directly influences the estimation of both the overburden pressure and effective pressure computation. So when we use seismic data to predict pore pressure, we need to determine where the onset of abnormal pressure is, then use suitable trends for above and below geopresure. By adjusting the NCT we computed n for six tracts based on Ebrom's minimum velocity method. All six tracts show a relatively consistent n value of 0.83, which should be taken into account when an accurate pore pressure prediction is wanted, especially in depths below 3000 m. With our method to predict pore pressure we limit the need to adjustment the exponent in the Eaton or Katahara equation.

4 SHEAR-WAVE SENSITIVITY TO PORE PRESSURE

4.1 Introduction

Recent research has shown that shear-wave velocity (V_S) and V_P/V_S ratio are more sensitive to pore pressure in mud rocks than the typical P-wave velocity (V_P) (Ebrom et al., 2003, 2006; Hofmann et al., 2005). For sands, V_P/V_S ratios are observed to increase with increases in pore pressure (Huffman and Castagna, 2001; Prasad, 2002). It suggests a greater decrease of V_S than V_P in abnormal pressure zones due to the loss of rigidity in the high pore pressure (lower effective pressure) regime. Lab experiments show that shear moduli are more sensitive to differential pressure variations than bulk moduli (Hornby, 1996; Hofmann et al., 2005) (Figure 4-1). It appears V_S is a good candidate for pore pressure prediction. There are few published V_S-depth trends and V_P/V_S ratio plots for the GOM in abnormal pressure. In addition, the dipping trends in Figue 4-1 suggest that $n \neq 1$ for the bulk modulus but $n=1$ for the shear modulus.

Besides pore pressure prediction, V_P/V_S ratio is also a key parameter for seismic AVO modeling, especially for lithology and fluid prediction. Model results show that large changes in V_S and V_P/V_S ratio in abnormal preesure area result in significant changes in the AVO response (Duffaut and Landrø, 2007). So calibration of V_P/V_S trends in different pressure regimes are also needed for AVO modeling.

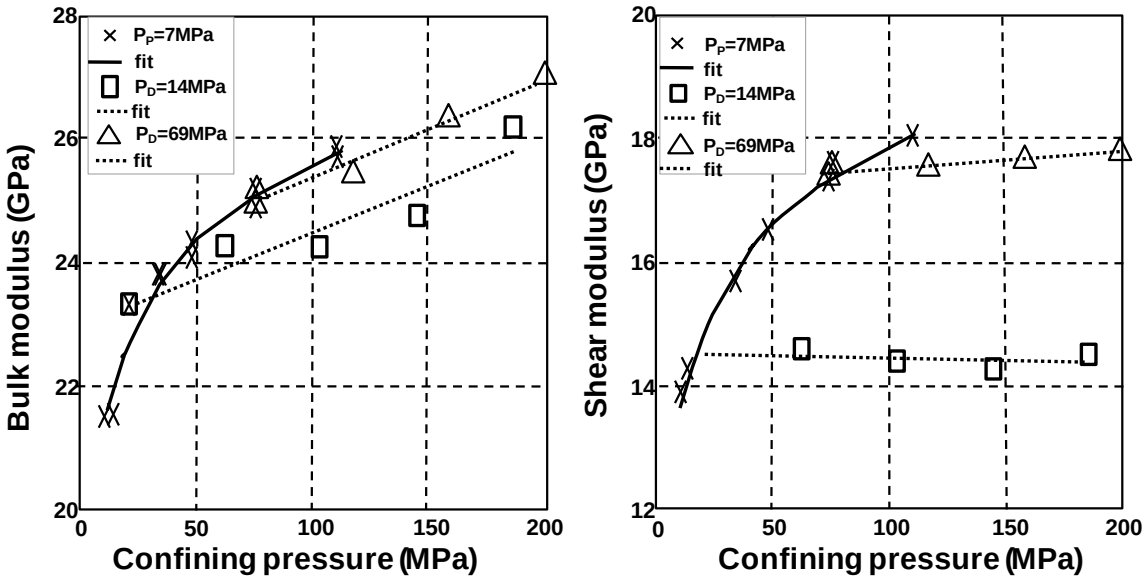

Figure 4-1: Sensitivity of bulk and shear moduli to differential pressure (Hornby, 1996).

In this chapter we examined dipole sonic data from the northern and southern regimes in GOM, and established V_P-V_S relationships for above and below geopressure. More importantly, by using Gassmann's inversion for the dry-rock bulk modulus, K_{dry}, we found a similar relationship between the effective pressure coefficient, n, and K_{dry} derived from P-wave velocity.

4.2 Method

For the purpose of this study, TGS loaned 27 wells in northern South Marsh Island and Eugene Island, mainly in Tracts 1 and 2, and 24 wells in the south, mainly in Tracts 5 and 6. Figure 4-2 is a representative suite of well-log curves selected for this study. Normally the suite of logs include: P-wave slowness, shear-wave slowness, resistivity, gamma ray,

SP, caliper, density, and neutron porosity. In this well, the response of the P-wave, S-wave, and resistivity curves to geopressure is very obvious at the depth interval from 13000-15000 ft (4000-5000 m).

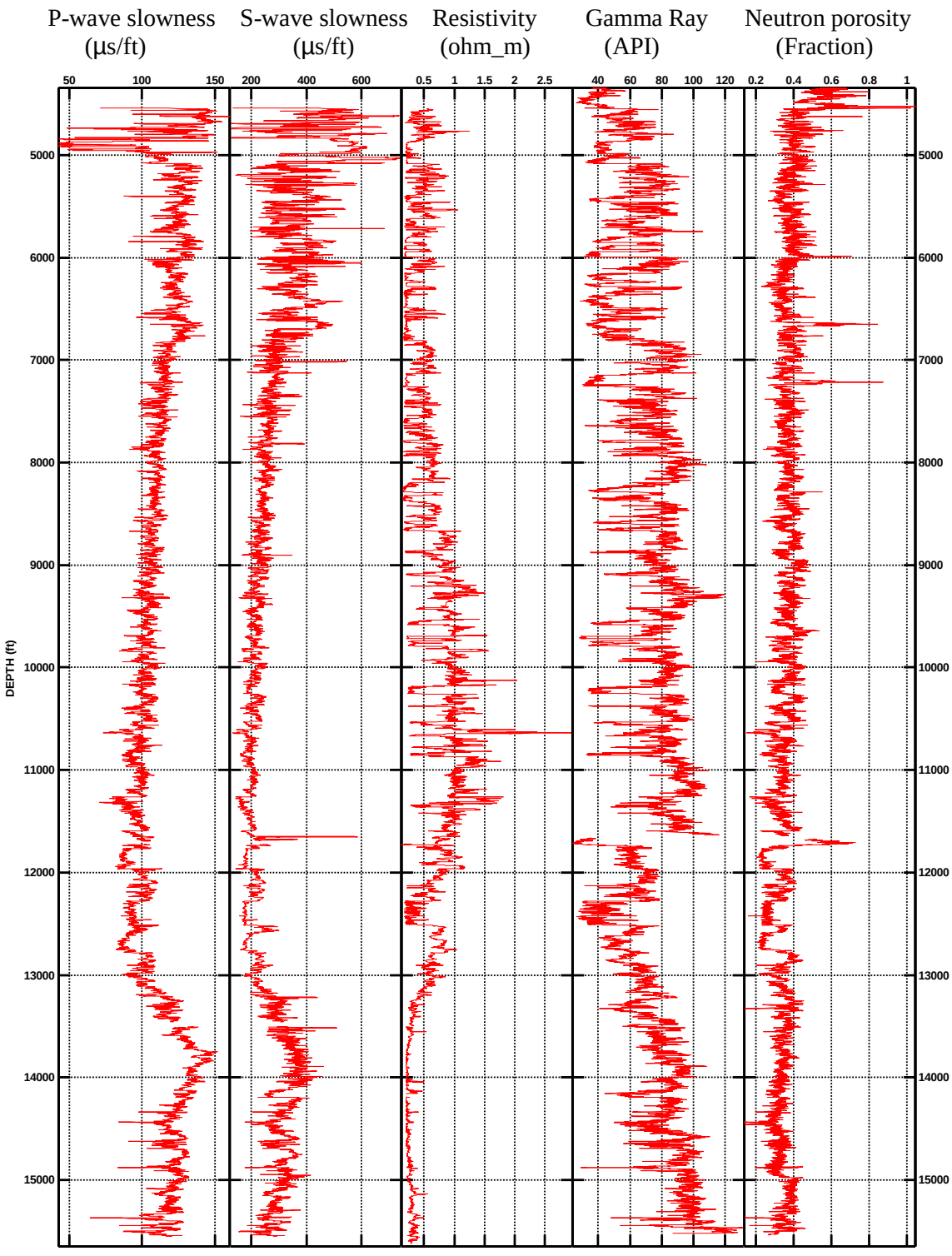

Figure 4-2: Typical well-log suite selected for study.

By carefully examining the available S-wave curves along with the other logged curves, we found 15 wells in the northern area and 11 wells in the southern part that are applicable for this research. Conditioning and analyzing the well-log data are important aspects of this study. All log curves for each well are explicitly checked and a library is built for each well which contains the original log file, mud weights recorded on the log-run header, temperature, hole effect file and matlab processed subdata file. The main data processing steps are:

1. Analyze 400 well reports to generate mud weight and temperature database for each well from log run headers;
2. Quality control the log suites for each well and select the appropriate P-wave slowness, shear-wave slowness, gamma ray, resistivity and porosity curves for subsequent statistical analyses;
3. Generate a “hole effect” text file which controls those portions of the well to be skipped during subsequent statisitical analyses. These zones include questionable log-quality intervals in the sonic and density curves, hydrocarbon intervals, salt intervals, pure sand intervals, and large caliper intervals;
4. Compute V_P, and V_S from P-wave slowness and shear-wave slowness;
5. Generate shale volume V_{clay} curve for each well from gamma log (G) as

if G>=100, V_{clay}=1, it is pure shale;

if G<=50, V_{clay}=0, it is pure sand ;

if 50<G<100, V_{clay}=1-(100-G)/(100-50).

6. Average V_P, V_S, mud weight and temperature for each 60 m (200 ft) interval for shale from the top of the log to TD. The sediment is defined as shale if V_{clay} is greater than 50%.

7. Establish a linear relationship between V_P-V_S in the northern and southern areas; and

8. Establish a relationship between V_P/V_S ratio and pore pressure.

4.3 Results

4.3.1 V_P and V_S depth trends in the northern and southern areas

In the northern and southern areas, the V_P and V_S respond in a similar manner to pore pressure variations as that discussed in Chapter 2. Both the V_P and V_S values stop increasing at the onset of geopressure (Figure 4-3). Similar to what is discussed in Chapters 2 and 3, a mud weight of 12 lb/gal is selected to delimit above and below geopressure. If the mud weight is less than 12 lb/gal, the interval is treated as a normal pressure zone; if the mud weight is more than 12 lb/gal, it is treated as an abnormal pressure zone.

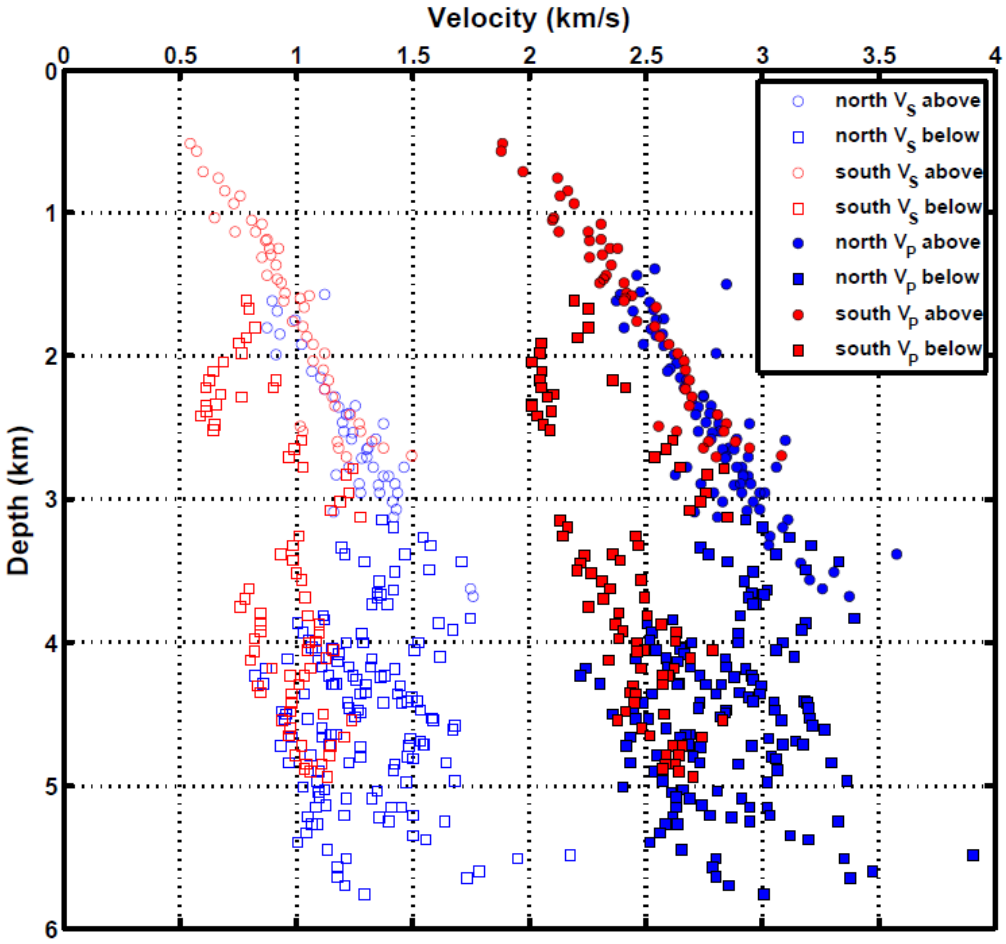

Figure 4-3: Average V_P and V_S velocity in 60 m zones for all 26 wells.

4.3.2 V_P-V_S relationship in the northern and southern areas

In Figure 4-4, the shale V_P-V_S linear relationships for normal and abnormal pressure zones in the northern portion are displayed. For above geopressure, the linear relationship between V_P and V_S is

$$V_S=-1.272+0.902V_P, \quad (4\text{-}1)$$

and for below geopressure

V_S=-1.003+0.811V_P. (4-2)

From Figure 4-5, the V_P-V_S relationships in the southern area are quite similar for above and below geopressure; for above geopressure

V_S=-0.850+0.745V_P, (4-3)

and, for below geopressure

V_S=-0.839+0.730V_P. (4-4)

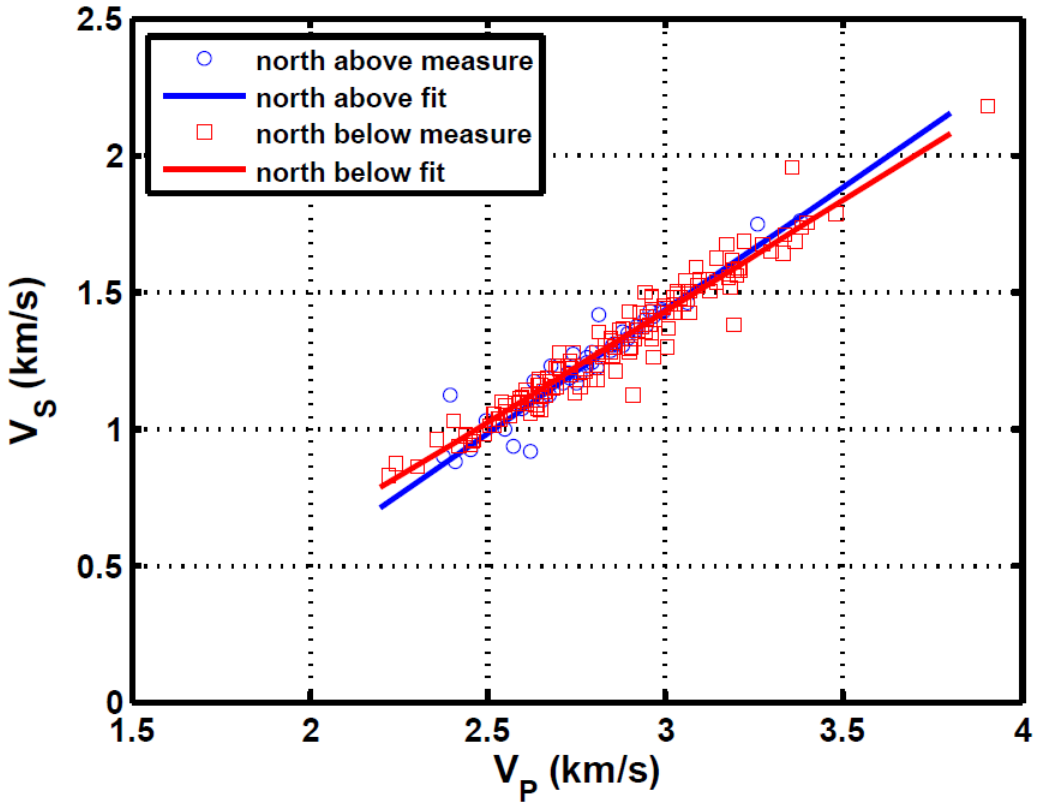

Figure 4-4: V_P-V_S relation for normal and abnormal pressure zones in the northern area.

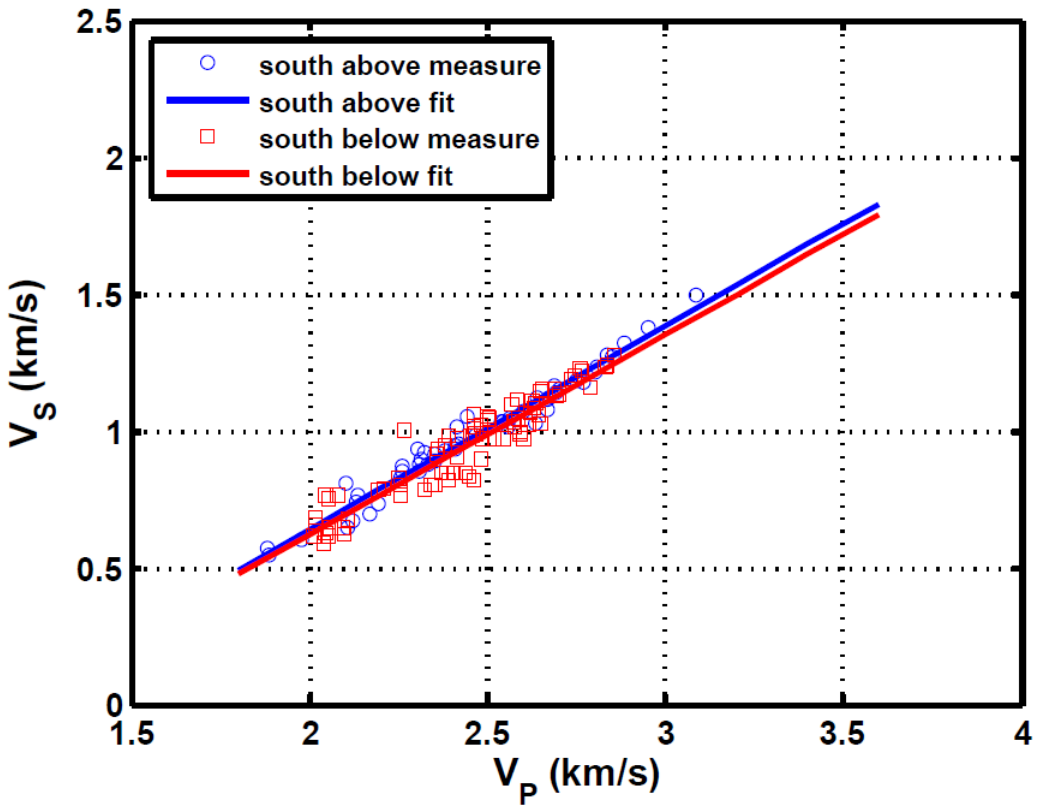

Figure 4-5: V_P-V_S relation for normal and abnormal pressure zones in the southern area.

In order to compare the V_P-V_S relationships, all four trends are overplotted in Figure 4-6 along with the Greenberg-Castagna (1992) V_P-V_S transform for shale. Basically, the northern V_P-V_S trend below geopressure, southern above and below have similar V_P-V_S trends. But the measured V_S is systematically less than the Greenberg-Castagna (1992) estimation, especially in the southern area. The V_P-V_S trend curve for normal pressure in the northern area remains an enigma. We tried to obtain VSP data that could be analyzed for downward traveling V_P and V_S waves to obtain an independent method of measuring V_P-V_S relationships. Unfortunately, no data were made available for this study.

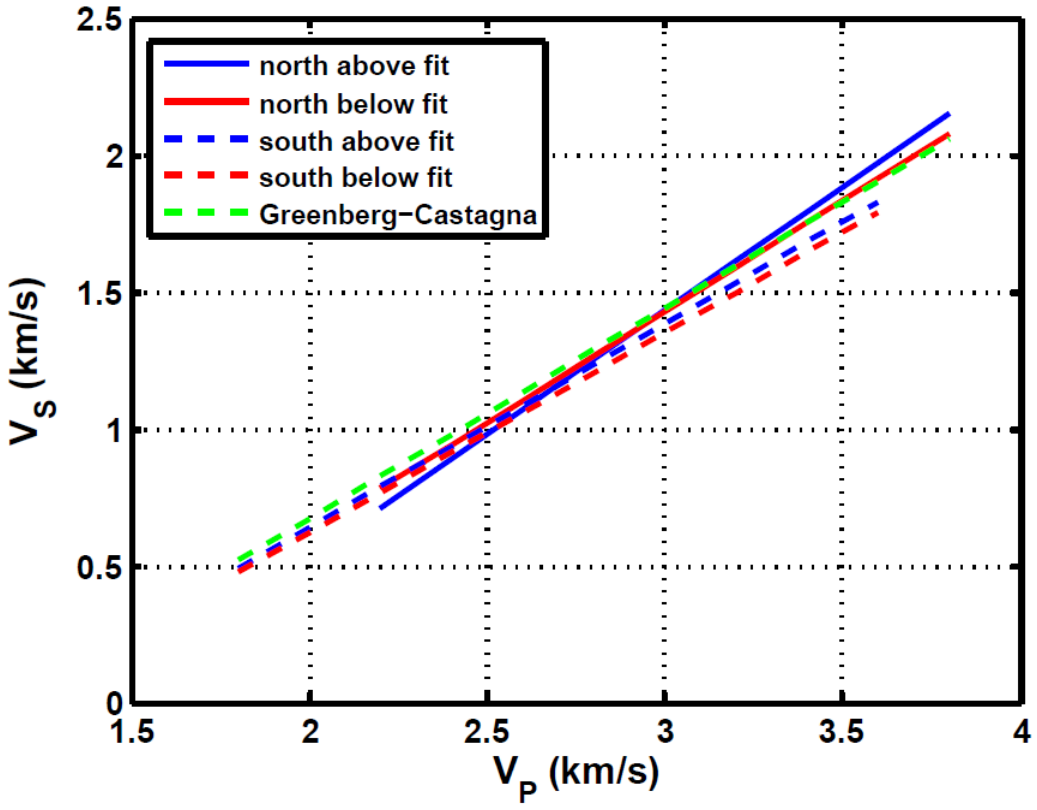

Figure 4-6: V_P-V_S trends in the northern and southern areas above and below geopressure along with Greenberg-Castagna (1992) shale line.

4.3.3 V_P-V_S ratio and pore pressure prediction

The V_P/V_S ratios in the northern and southern areas are shown in Figure 4-7. The V_P/V_S ratios above geopressure in both the northern and southern areas are fitted by a normal compaction trend which has similar format as Athy's normal density trend discussed in Chapter 2 and is expressed as

$$\frac{V_P}{V_S} = \left(\frac{V_P}{V_S}\right)_o + ae^{-bz}, \tag{4-5}$$

where $\left(\frac{V_P}{V_S}\right)_o$ is the minimum V_P/V_S at infinite depth, a and b are empirically derived coefficients, z is depth in meters. The least-squares coefficients are listed in Table 4-1 and the trends are overplotted in Figure 4-7.

Table 4-1: Least-squares coefficients for V_P/V_S normal trends.

Area	$(V_P/V_S)_0$	a	b(1/m)
north	1.22	2.49	3.51×10^{-4}
south	1.40	2.21	3.97×10^{-4}

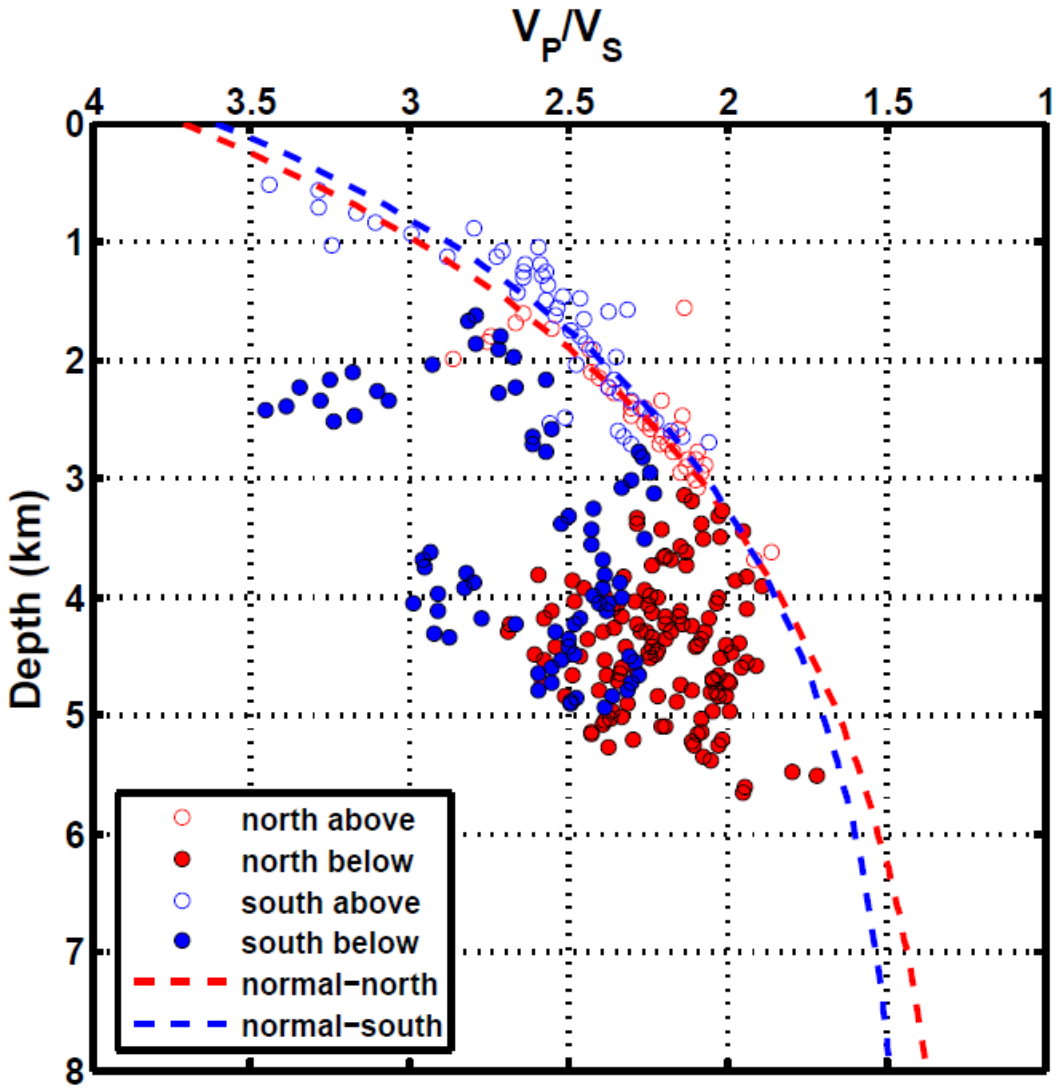

Figure 4-7: V_P/V_S data for the northern and southern areas. Normal compaction type trends are represented by dashed line.

A V_P to pore pressure transform was established in previous chapters, now a V_P/V_S-pore pressure transform is established. A method suggested by Ebrom et al. (2006) is

$$P_P = P_C - P_{E\_NCT}\left(\frac{(V_P/V_S)_{NCT}}{(V_P/V_S)_{OBS}}\right)^Y = P_C - (P_C - P_{HYDRO})\left(\frac{(V_P/V_S)_{NCT}}{(V_P/V_S)_{OBS}}\right)^Y, \quad (4\text{-}6)$$

where $(V_P/V_S)_{OBS}$ is the observed V_P/V_S ratio in abnormal pressure and $(V_P/V_S)_{NCT}$ is the expected V_P/V_S ratio at hydrostatic pore pressure, which can be predicted from equation (4-5). The exponent Y describes the sensitivity of the velocity ratio to effective pressure and is calibrated to specific study areas.

In this study, with the calibrated Y set to 6, the comparison between measured pore pressure by mud weight and predicted pore pressure is shown in Figure 4-8. Green dashed line is overburden pressure P_C. Cyan dashed line is hydrostatic pressure P_{HYDRO}. Red open circle represents mud weight converted pore pressure in normal pressure zone called observed pore pressure, P_P-obs-normal; while, blue open circle represents mud weight converted pore pressure in abnormal pressure regime, P_P-obs-abnormal. Red solid circle is predicted pore pressure from equation (4-6) in normal pressure zone called observed pore pressure, P_P-pred-normal; while, blue solid circle is predicted pore pressure in abnormal pressure regime, P_P-pred-abnormal. Reasonable match between measured and predicted pore pressure is obtained in both northern and southern areas.

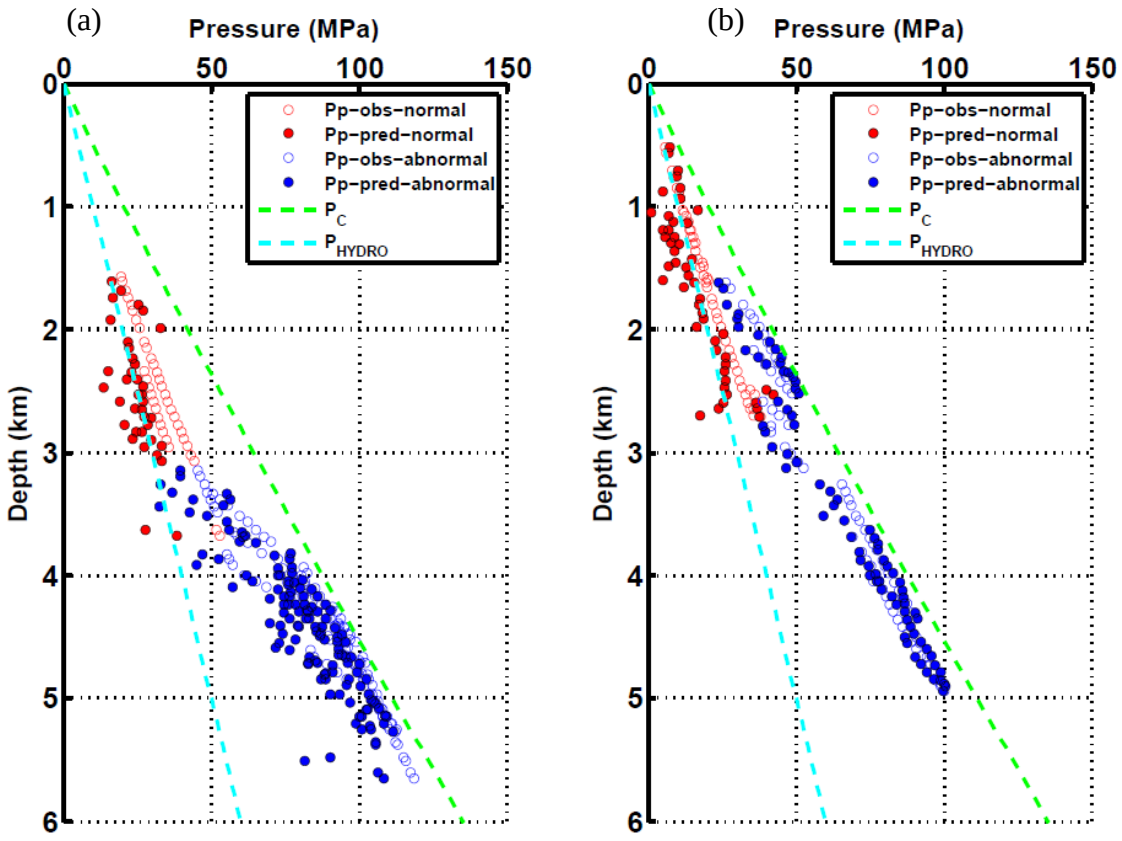

Figure 4-8: Comparison between predicted and measured pore pressure in the northern (a) and southern (b) areas using V_P/V_S ratios.

4.3.4 Effective pressure coefficient from Gassmann inversion

Nur and Byerlee (1971) demonstrated theoretically that the effective pressure coefficient for strain equals the Biot-Willis coefficient (Biot and Willis, 1957), equation (1-5). However they warned this relationship is not applicable to seismic velocity. In this section we want to test this statement by inverting Gassmann's equation using the dipole sonic data. Even though shale doesn't satisfy Gassmann's assumptions, it's mathematical

form does provide insight into the sensitivity of various rock properties to pore pressure variations.

In selecting the parameters for Gassmann's equation, the shale porosity ϕ, V_P, and V_S were taken from the 60 m interval rock-properties. In order to transform the porosity into bulk rock density ρ_b, a rock matrix density of 2.65 g/cm^3 is assumed (equation 4-7). The dry shear modulus (μ_{dry}), wet shear modulus (μ_{sat}) and wet bulk modulus (k_{sat}) are computed as shown in equations 4-8 and 4-9.

$$\rho_b = (1-\phi)\rho_m + \phi\rho_w. \tag{4-7}$$

$$\mu_{dry}=\mu_{sat}=\rho_b V_s^2. \tag{4-8}$$

$$k_{sat}=\rho_b(V_p^2 - 4/3V_s^2). \tag{4-9}$$

The dry rock bulk modulus, $K_{dry,}$ is then calculated from the expression (Smith et al., 2003)

$$K_{dry} = \frac{K_{sat}\left[\left(\phi\frac{K_{ma}}{K_{fl}}\right)+1-\phi\right]-K_{ma}}{\left[\left(\phi\frac{K_{ma}}{K_{fl}}\right)+\left(\frac{K_{sat}}{K_{ma}}\right)-1-\phi\right]}. \tag{4-10}$$

A grain bulk modulus K_{ma} of 37 GPa is assumed for shale. The brine density and bulk modulus was computed with the Batzle-Wang (1992) equations.

Once K_{dry} is computed for each 60 m sample, the Biot coefficient is computed as $\beta=(1-K_{dry}/K_{ma})$. The computed Biot coefficients, β, and average values of 200 m are plotted in Figure 4-9. It ranges from 0.92 to 0.6. In both northern and southern areas above geopressure, an obvious linearly decreasing trends for β are observed. However, in abnormal pressure the trends have a constant value of approximatly 0.8, which is close to our computed effective pressure coefficent n, in Chapter 3.

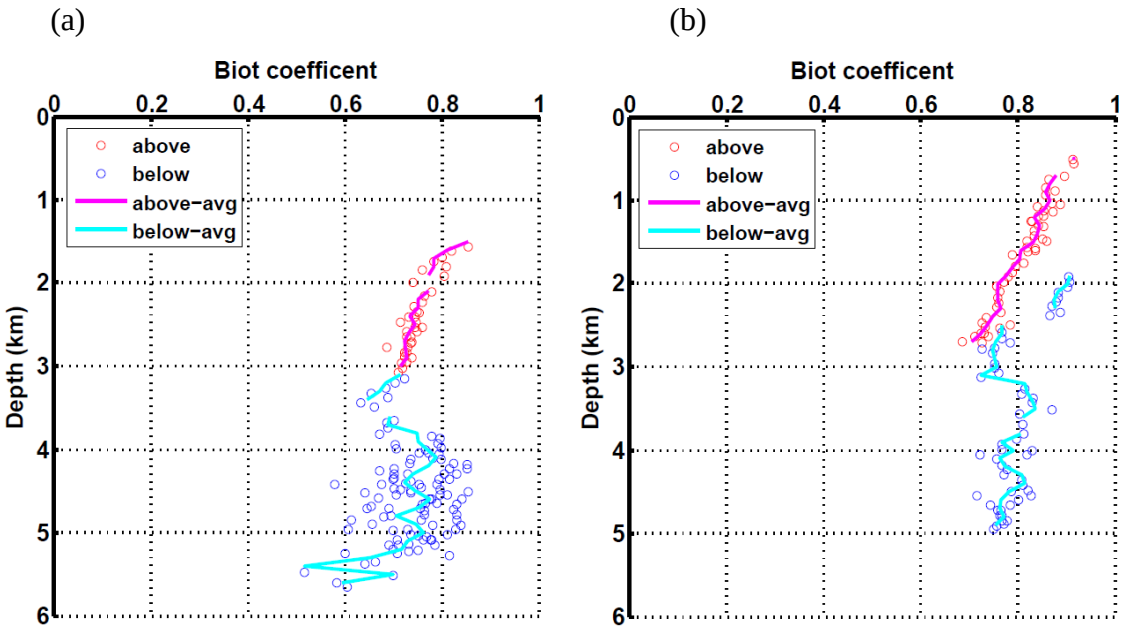

Figure 4-9: Biot coefficient from Gassmann's equation in the northern (a) and southern (b) areas above and below geopressure.

The northern area has appreciable scatter for the Biot coefficient in the abnormal pressure zone. As discussed in Chapter 2, in the northern area below geopressure, smectite possibly changes into illite, which has a higher density and bulk modulus than smectite.

Therefore, the Biot coefficient should be re-computed with more suitable maxtix properties. This is done by setting the bulk modulus K_{ma} to 50 GPa and ρ_{ma} to 3.0 g/cm^3, which represent illite in geopressure (Fleet, 2003). Results are shown in Figure 4-10. The scatter in abnormal pressure is reduced and the average value of Biot coefficient is around 0.8.

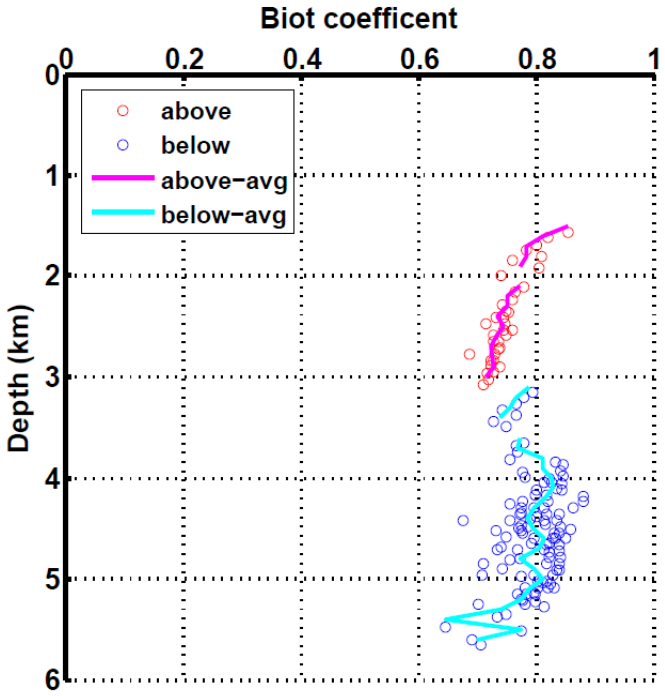

Figure 4-10: Biot coefficient from Gassmann's equation in the northern area with different rock properties below geopressure.

4.4 Discussion

4.4.1 Expression of effective pressure coefficient n for elastic velocity

Gassmann's theory is routinely used for fluid substitution (Smith et al., 2003; Mavko et al., 2009). V_P of saturated rock can be computed from Gassmann's equation (Hilterman, 1998, 2001) as

$$\rho_b V_P^{\,2} = K_{dry} + 4/3\mu + \frac{\left(1-\frac{K_{dry}}{K_{ma}}\right)^2}{\frac{\left(1-\frac{K_{dry}}{K_{ma}}-\phi\right)}{K_{ma}} + \frac{\phi}{K_{fl}}}. \qquad (4\text{-}11)$$

In the third term on the right side of equation (4-11), there is an expression $1-K_{dry}/K_{ma}$. By comparing Figures 4-9, 4-10 and 3-7 we propose for elastic wave velocity, effective pressure coefficient n can be expressed in the same form as Biot coefficient for static compressibility, which is

$$n = 1-\frac{K_{dry}}{K_{ma}}. \qquad (4\text{-}12)$$

From the term $(1-K_{dry}/K_{ma}-\phi)$ which is $(n-\phi)$ in the denominator, a lower bound for n is suggested which is n should be greater than ϕ because the term $(n-\phi)/K_{ma}$ represents a compressibility which is always positive. This conclusion is the same constraint for the effective pressure coefficient for volume strain (Berryman, 1992, 1993). In short, the parameter n is embedded in Gassmann's equation. In wildcat areas where there are no

offset wells to calibrate the classical empirical equations for predicting pore pressure or n as developed in Chapter 3, we can use Gassmann's equation along with either a multi-component survey or a V_S transform from V_P to invert for K_{dry} to get an approximation of n.

4.4.2 Quantification of difference between measured and predicted Vs for shale

The Greenberg-Castagana (1992) V_S-V_P transforms are widely used and are considered to be rather robust from one region to the next. The sandstone transform, in terms of km/s, is

$$V_S=-0.856+0.804V_P, \quad (4\text{-}13)$$

and the shale transform is

$$V_S=-0.867+0.770V_P. \quad (4\text{-}14)$$

In this study, we computed the Greenberg-Castagna Vs (equation 4-15) by incorporating the sonic and the shale volume logs in the normal and abnormal pressure zone.

$$V_{S\_predict} = (-0.867+0.770V_P)V_{clay}+(-0.856+0.804V_P)(1-V_{clay}). \quad (4\text{-}15)$$

The predicted shear-wave velocities are compared to the measured in Figures 4-11 and 4-12. For normal pressure in the northern area (Figure 4-11a), the predicted V_S trend appears to cross the measured V_S trend. These data were previously examined by analyzing the best fit transform in Figure 4-4 and it was difficult to explain the sharp

difference between this single transform and the others that were measured. This still remains questionable.

In Figure 4-12, for data in abnormal pressure, the measured V_S are systematically less than the predicted V_S. In the southern area the abnormal pressure zone is just and an extension of the normal pressure zone and at the onset of pressure, the properties “freeze”. There is no change in the basic grain properties, so the V_P-V_S relationship is quite similar for above and below geopressure. This is not the case for the northern area where there is a smectite to illite transformation and thus different grain properties above versus below which is displayed in Figure 4-11.

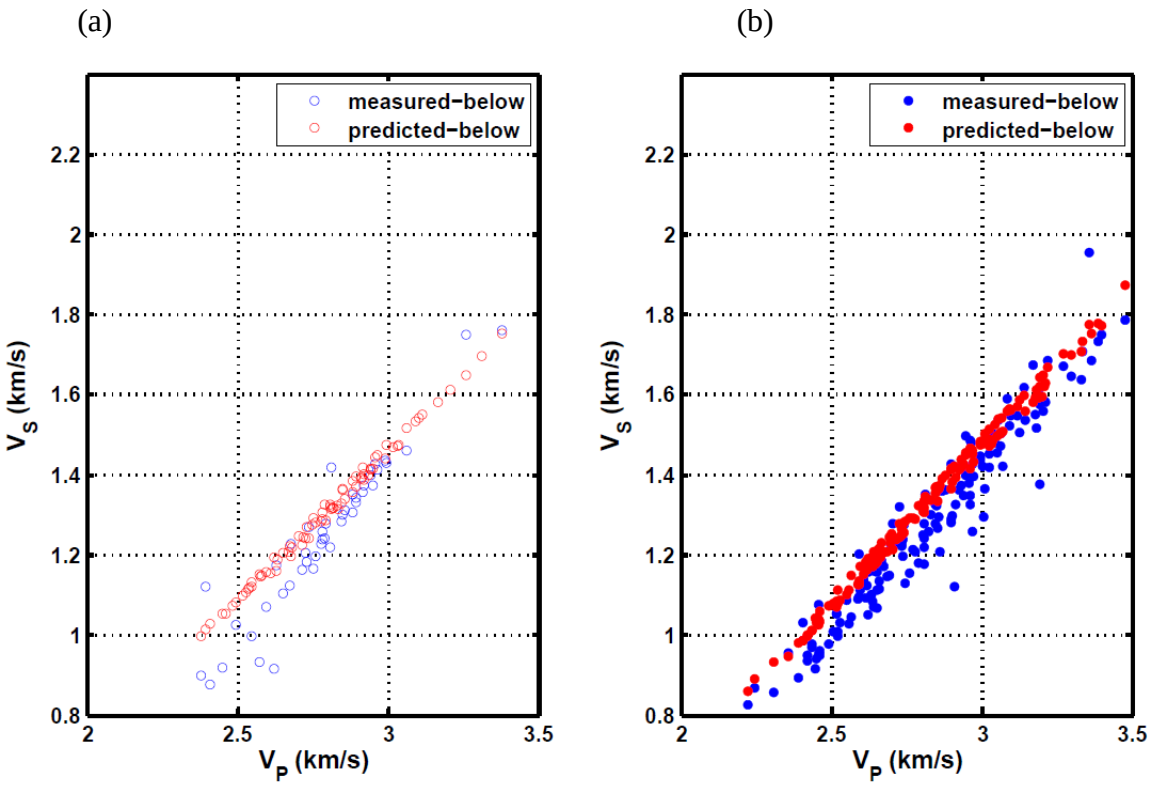

Figure 4-11: Measured V_S values versus Greenberg-Castagna predicted V_S values for the northern area for above (a) and below (b) geopressure.

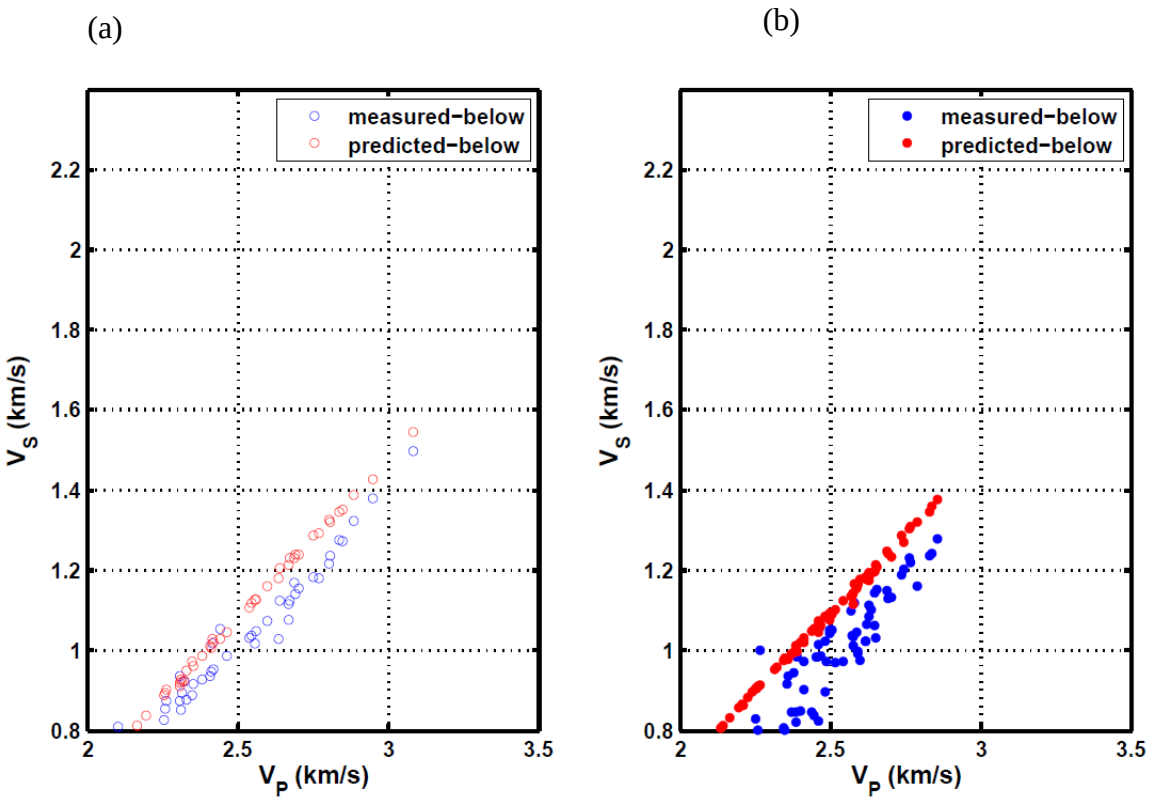

Figure 4-12: Measured V_S values versus Greenberg-Castagna predicted V_S values for the southern area for above (a) and below (b) geopressure.

In order to assist future predictions of Vs in abnormal pressure zones and for AVO analysis, it is necessary to quantify the magnitude difference between measured V_S and predicted V_S. We compute the ratio M between the measured and estimated V_S for all logging depth (equation 4-16) in abnormal pressure for each well. Listed in Table 4-2 are the correlation coefficients R between measured and predicted V_S for each well, the mean <M> and standard deviation δ of M, for each well. The measured Vs is around 90% that of the predicted Vs (Figure 4-13).

$$M = (V_{s\_measure}/V_{s\_predict}). \quad (4\text{-}16)$$

Table 4-2: Comparison between measured and predicted V_S in geopressure zone for 25 wells.

well sequence	R	<M>	δ
1	0.91	0.89	0.04
2	0.96	0.98	0.05
3	0.93	1.00	0.05
4	0.93	0.95	0.06
5	0.98	1.03	0.04
6	0.83	0.97	0.06
7	0.91	0.96	0.05
8	0.87	0.95	0.07
9	0.87	0.91	0.12
10	0.91	0.96	0.04
11	0.87	0.95	0.06
12	0.91	0.97	0.04
13	0.81	0.96	0.06
14	0.90	0.98	0.06
15	0.84	0.91	0.04
16	0.88	0.93	0.09
17	0.68	0.92	0.07
18	0.46	0.86	0.07
19	0.72	0.89	0.14
20	0.77	0.93	0.11
21	0.68	0.92	0.11
22	0.69	0.94	0.05
23	0.77	0.82	0.05
24	0.43	0.97	0.11
25	0.87	0.91	0.05

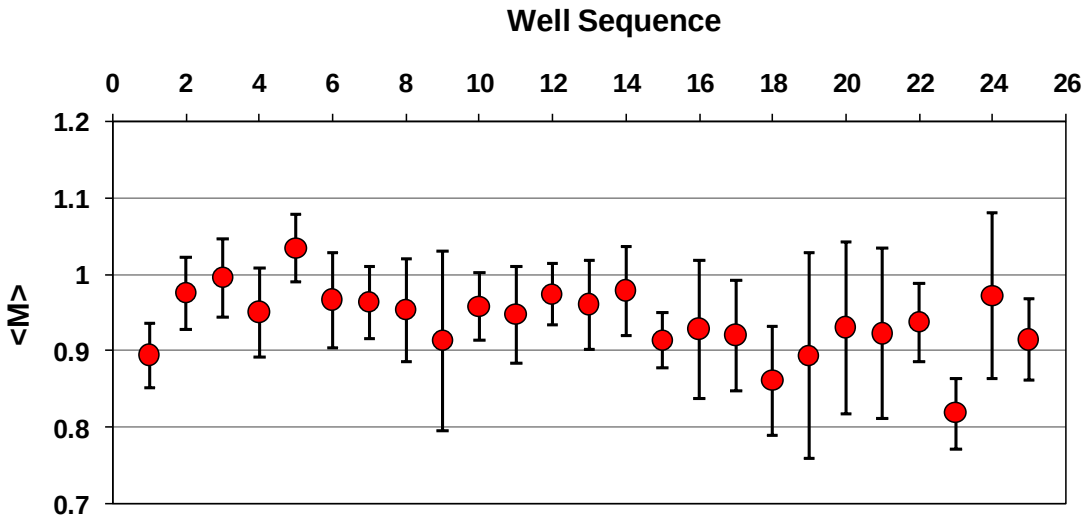

Figure 4-13: Comparison between measured V_S value to Greenberg-Castagna predicted V_S. Well sequence numbers from 1-14 are from north, and 15-25 are from south.

Published research has shown that the S-wave velocity is sensitive to pore pressure variations and its percentage decrease is larger than that exhibited by the P-wave velocity (Hornby, 1996; Ebrom et al., 2003; Hofmann et al., 2005). Ebrom et al. (2006) found in abnormal pore-pressure intervals the V_P/V_S ratio increased significantly over the normal pore-pressure intervals (Figure 4-14). Their measured S-wave velocity from shear dipole sonic was 75% the estimated S-wave velocity from the Greenberg-Castagna equation (1992). Our study confirmed this and we suggested in geopressure zone, an adjusting factor should be adapted before the Greenberg-Castagna (1992) mud rock line prediction when one wants to compute the shear wave velocity. A factor of 0.9 would be a reasonable value to use from our observation.

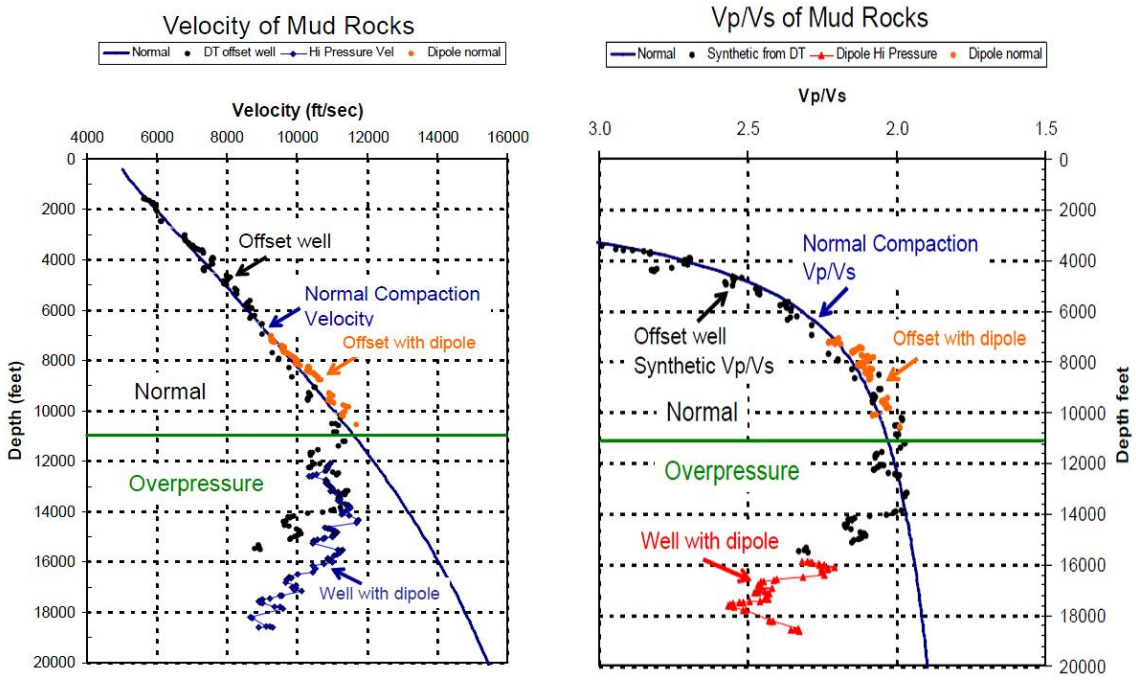

Figure 4-14: Measured V_P/V_S ratio from Ebrom et al. (2006).

4.4.3 AVO test on shear wave sensitivity to abnormal pressure

The different V_P/V_S relationships in abnormal pressure zones will influence AVO analyses. Tests on the AVO response to different V_P-V_S relationships are conducted. It is assumed that all rock properties remain the same except for the V_P/V_S change in abnormal pressure zones. In order to quantify the AVO response, the intercept A, and gradient, B, are calculated from Shuey's (1985) linear approximation of the Zoeppritz equation,

$$RC(\theta) = A + B\sin^2(\phi), \tag{4-17}$$

where θ is the incident angle, and ϕ is the average of the incident and transmitted angles.

$$A = \frac{\rho_2\alpha_2 - \rho_1\alpha_1}{\rho_2\alpha_2 + \rho_1\alpha_1}, \tag{4-18}$$

$$B = \frac{1}{2}\frac{\Delta\alpha}{\alpha} - 2\left(\frac{\beta}{\alpha}\right)^2\left(\frac{2\Delta\beta}{\beta} + \frac{\Delta\rho}{\rho}\right), \tag{4-19}$$

where

$$\alpha = \frac{\alpha_1 + \alpha_2}{2} \quad \beta = \frac{\beta_1 + \beta_2}{2} \quad \rho = \frac{\rho_1 + \rho_2}{2},$$

$$\Delta\alpha = \alpha_2 - \alpha_1 \quad \Delta\beta = \beta_2 - \beta_1 \quad \Delta\rho = \rho_2 - \rho_1,$$

where α_1, β_1, and ρ_1 are the V_P, V_S, and ρ_b of the overlying shale layer, and α_2, β_2, and ρ_2 are V_P, V_S, and ρ_b of the underlying sand layer. Greenberg and Castagna et al. (1992) equations were employed to estimate shear-wave velocity for brine-saturated sand and shale. Gassmann's fluid substitution (Smith et al., 2003) is used to calculate the oil- and gas-saturated reservoir sand responses. The grain bulk modulus for sand and shale are 37 MPa and 25 MPa (Sayers et al., 2011) and densities are 2.65 g/cm^3 and 2.60 g/cm^3. In the first model, we use the original Greenberg-Castagna shear-wave transformation; the results are shown in Figure 4-15. In the second model, we put the scaling factor 0.9 in the Greenberg-Castagna shear-wave transformation and the AVO results are shown in Figure 4-16. The AVO response is quite different from the previous in Figure 4-15. With a reduced shear-wave velocity in GP, a more negative AVO gradient is expected. In this study AVO simulations with different bulk moduli and densities for sand and shale have also been tested, but these results were not as significant as the changes observed in Figure 4-16 due to shear-wave velocity changes.

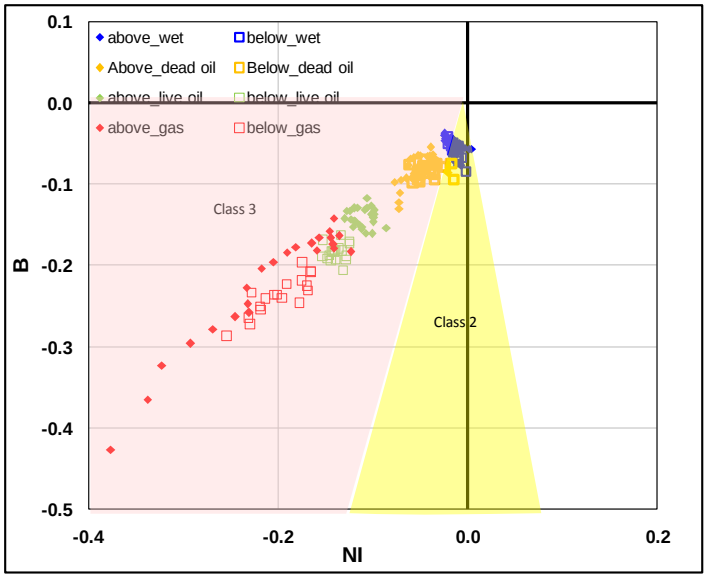

Figure 4-15: AVO response of southern GOM with Greenberg-Castagna V_P-V_S relationship for shale below GP.

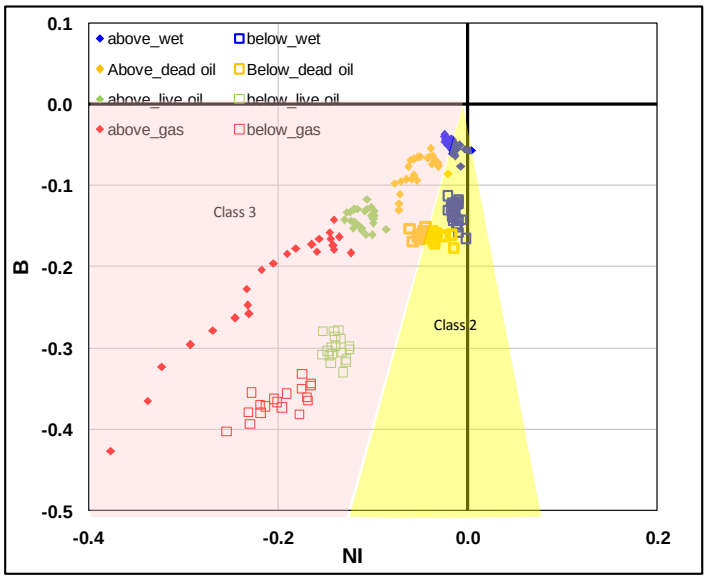

Figure 4-16: AVO response of southern GOM with a scaling factor 0.9 in Greenberg - Castagna (1992) V_P-V_S relationship for shale below GP.

4.5 Summary

By examining dipole sonic data from 26 wells we establish different V_P-V_S relationships in the northern and southern GOM above and below geopressure. Our results show in overpressure zones, V_S drops more significantly than V_P, the measured V_S is only 90% of the estimation by the Greenberg-Castagna (1992) equations. By inverting K_{dry} from the Gassmann's equation we found that the effective pressure coefficient is expressed in the same form as Biot coefficient. This sheds light on n calibrations in wildcat exploration areas. Our research indicates if multicomponent seismic data are available, we can run Gassmann inversion to get n, and then apply it for pore pressure prediction.

5 CONCLUSIONS

In the exploration and production of oil and gas, pore pressure prediction is very important. However, instead of using the classical empirical methods to predict pore pressure we propose a different methodology based on the effective stress law. Our research in the Louisiana GOM found:

1. On the continental shelf of the GOM there are two types of abnormal pressure regimes: unloading and undercompaction. Detailed statistical analyses of density and velocity trends reveal that in the northern area of GOM, unloading is the major mechanism of geopressure. GP occurs at depths around 3000 m with temperatures as high as 100 °C. The correspondence of the temperature gradient increase with the illite-smectite transformation and the transitional responses at the onset of GP for both the velocity and density trends make us believe inelastic unloading is the major mechanism for overpressure. Comparatively in the southern continental shelf, undercompaction is the dominant mechanism. Compaction stops at the onset of GP; both shale density and velocity freeze at the onset of abnormal pressure. The density response to different pressure mechanisms suggests different overburden pressure models need to be established when accurate pore pressure prediction is desired.

2. Instead of assuming the effective pressure coefficient equals one for all depths in the GOM, we revealed the variation of n with depth and pressure regimes by calibrating over 400 wells in the South Marsh Island and Eugene Island Areas. In abnormal pressure

intervals, n decreases to 0.83. Our observation is consistent with the effective stress law, which indicates as the value of porosity decreases, n also deceases from unity.

3. In wildcat areas where no offset wells are available to calibrate n, we illustrate how Gassmann's inversion for K_{dry} is a feasible method to calibrate n. Reliable V_S measurements from multi-component seismic and reasonable K_{ma} values for shale are two key issues for the success of this method.

4. Dipole sonic data from 25 wells have an unexpected decrease of V_S in abnormal pressure intervals. The measured V_S values are about 90% of those predicted by the Greenberg-Castagna equation. This suggests that V_S is more sensitive to abnormal pore pressure than V_P. We established the relationship between V_P/V_S ratio and pore pressure prediction in this study.

REFERENCES

Athy, L. F., 1930, Density, porosity, and compaction of sedimentary rocks: AAPG Bulletin, **14**, 1-22.

Banthia, B. S., M. S. King, and I. Fatt, 1965, Ultasonic shear-wave velocities in rocks rocks subjected to simulated overburden pressure and internal pore pressure: Geophysics, **30**, #1, 117-121.

Barker, C., 1972, Aquathermal pressuring-role of temperature in development of abnormal-pressure zones: AAPG Bulletin, **56**, #10, 2068-2071.

Batzle, M., and Z. Wang, 1992, Seismic properties of pore fluids: Geophysics, **57**, 1396-1408.

Berryman, J. G., 1992, Effective stress for transport properties of inhomogeneous porous rock: Journal of Geophysical Research, **97**, 17409-17424.

Berryman, J. G., 1993, Effective-stress rules for pore-fluid transport in rocks containing two minerals: Int. J. Rock Mech. Min. Sci. & Geomech Abstract, **30**, 1165-1168.

Bethke, C. M., 1986, Inverse hydrologic analysis of the distribution of origin of Gulf Coast-type geopressured zones: Journal of Geophysical Research, **91**, #B6, 6535-6545.

Biot, M. A., 1941, General theory of three-dimentional consolidation: Journal of Applied Physics, **12**, #2, 155-164.

Biot, M. A., and D. G. Willis, 1957, The elastic coefficients of the theory of consolidation: Journal of Applied Mechanics, **24**, #4, 594-601.

Bjerrum, L., A. Casagrande, R. B. Peck, and A. W. Skempton, 1960, From theory to practice in soil mechanics: selections from the writings of Karl Terzaghi, with bibliography and contributions on his life and achievements. New York, London, John Wiley and Sons.

Bowers, G. L., 1995, Pore pressure estimation from velocity data: Accounting for pore pressure mechanisms besides undercompaction: SPE Drilling and Completion, **10**, #2, 89-95.

Bowers, G. L., 2002, Detecting high overpressure: The Leading Edge, **21**, #2, 174-177.

Brandt, H., 1955, A study of the speed of sound in porous granular media: Journal of Applied Mechanics, **22**, 479-486.

Bruce, B., and G. Bowers, 2002, Pore pressure terminology: The Leading Edge, **21**, #2, 170-173.

Bruce, C. H., 1984, Smectite dehydration – its relation to structural development and hydrocarbon accumulation in Northern Gulf of Mexico basin: AAPG Bulletin, **68**, #6, 673-683.

Carcione, J. M., A. F. Gangi, 2000, Gas generation and overpressure: Effects on seismic attributes: Geophysics, **65**, #6, 1769-1779.

Christensen, N. I., and H. F. Wang, 1985, The influence of pore and confining pressure on dynamic elastic properties of Berea sandstone: Geophysics, **50**, 207-213.

Colton-Bradley, V. A. C., 1987, Role of pressure in smectite dehydration-effects on geopressure and smectite-to-illite transition: AAPG Bulletin, **71**, 1414-1427.

Dickinson, G., 1953, Geological aspects of abnormal reservoir pressures in Gulf coast Louisiana: AAPG Bulletin, **37**, #2, 410-432.

Duffaut, K, and M. Landrø, 2007, V_P-V_S ratio versus differential stress and rock consolidation- A comparison between rock models and time-lapse AVO data: Geophysics, **72**, #5, 81-94.

Dugan, B., and T. C. Sheahan, 2012, Offshore sediment overpressures of passive margins: Mechanisms, measurement, and models: Reviews of Geophysics, **50**, RG3001.

Dutta, N., and J. Khazanehdari, 2006, Estimation of formation fluid pressure using high-resolution velocity from inversion of seismic data and a rock physics model based on compaction and burial diagenesis of shales: The Leading Edge, **12**, 1528-1539.

Dutta, N., T. Mukerji, M. Prasad, and J. Dvorkin, 2002a, Seismic detection and estimation of overpressure Part I: The rock physics basis: CSEG Recorder, **27**, #7, 34-57.

Dutta, N., T. Mukerji, M., Prasad, J., and Dvorkin, 2002b, Seismic detection and estimation of overpressure Part II: Field applications: CSEG Recorder, **27**, #7, 58-73.

Dutta, N.C., 2002, Geopressure prediction using seismic data: Current status and the road ahead: Geophysics, **67**, 2012-2041.

Dutta, T., G. Mavko, T. Mukerji, T. Lane, 2009, Compaction trends for shale and clean sandstone in shallow sediments, Gulf of Mexico: The Leading Edge, **5**, 590-596.

Eaton, B. A., 1975, The equation for geopressure prediction from well logs: SPE 50th Annual Fall Meeting, SPE paper 5544, 11pp.

Eberhart-Phillips, D., D. Han, and M. D. Zoback, 1989, Empirical relationships among seismic velocity, effective pressure, porosity, and clay content in sandstone: Geophysics, **54**, 82-89.

Ebrom, D., P. Heppard, and M. Albertin, 2006, Travel-time methods of V_P/V_S determination for pore-pressure prediction using look-ahead VSPs: Offshore Technology Conference, 18399.

Ebrom, D., P. Heppard, L. Thomsen, M. Mueller, T. Harrold, L. Phillip, and P. Watson, 2004, Effective stress and minimum velocity trends: 74th Annual International Meeting, SEG, Expanded Abstracts.

Ebrom, D., P. Heppard, M. Mueller, and L. Thomsen, 2003, Pore-pressure prediction from S-wave, C-wave and P-wave velocities: 73rd Annual International Meeting, SEG, Expanded Abstracts, 1370-1373.

Fatt, I., 1958, Compressibility of sandstones at low to moderate pressure: AAPG Bulletin, **42**, 1924-1957.

Fertl, W. H., G.V. Chilingarian, and H.H. Rieke III, 1976, Abnormal formation pressures, implications to exploration, drilling and production of oil and gas resources. Developments in Petroleum Science 2, Elsevier Scientific Publishing Company, Amsterdam, Oxford, New York, 1-48.

Fleet, M.E., Micas, 2003, Rock-forming minerals: Mica, Volume 3, P8, Geological Society.

Freed, R. L., and D. R. Peacor, 1989, Geopressured shale and sealing effect of smectite to illite transition: AAPG Bulletin, **73**, #10, 1223-1232.

Gardner, G. H. F., M. R. J. Wyllie, and D. M. Droschak, 1965, Hysteresis in the velocity-pressure characteristics of rocks: Geophysics, **30**, #1, 111-116.

Gassmann, F., 1951, Über die elastizität poröser medien: Vierteljahrss-chrift der Naturforschenden Gesellschaft in Zurich, **96**, 1-23.

Geertsma, J., 1957, The effect of fluid pressure decline on volumetric changes of porous rocks: Trans. AIME, **210**, 331-340.

Gordon, D. S., and P. B. Flemings, 1998, Generation of overpressure and compaction-driven fluid flow in a Plio-Pleistocene growth-faulted basin, Eugene Island 330, offshore Louisiana: Basin Research, **10**, #2, 177-196.

Greenberg, M. L., and J. P. Castagna, 1992, Shear-wave velocity estimation in porous rocks: Theoretical formulation, preliminary verification and applications: Geophysical Prospecting, **40**, 195-210.

Gretener, P. E., 1976, Pore pressure: fundamentals, general ramifications and implications for structural geology: AAPG Continuing Education Course Note Series #4, P10.

Grim, R. E., 1953, Clay mineralogy (second edition), McGraw-Hill Book Company, 465-467.

Gurevich, B., 2004, A simple derivation of the effective stress coefficient for seismic velocities in porous rocks: Geophysics, **69**, 393-397.

Gutierrez M. A., N. R. Braunsdorf, and B. A. Couzens, 2006, Calibration and ranking of pore-pressure prediction models: The Leading Edge, **12**, 1516-1523.

Heppard, P. D., H. S. Cander, and E. B. Eggertson, 1998, Abnormal pressure and the occurrence of hydrocarbons in offshore eastern Trinidad, West Indies, in Law, B.E., G.F. Ulmishek, and V.I. Slavin eds., Abnormal pressures in hydrocarbon environments: AAPG Memoir, **70**, 215-246.

Heppard, P., and D. Ebrom, 2010, Compaction and overpressure in shales: Practice and theory: Houston Geological Society Bulletin, 19-21.

Hicks, W. G., and J. E. Berry, 1956, Application of continuous velocity logs to determination of fluid saturation of reservoir rocks: Geophysics, **21**, #3, 739-754.

Hilterman, F. J., 1998, Rock property framework for comprehending deep-water seismic response: GSH 1998 Spring Symposium 14th Annual SEG Gulf Coast Technical Meeting.

Hilterman, F. J., 2001, Seismic amplitude interpretation: SEG/EAGE DISC.

Hofmann, R., X. Xu, and M. Batzle, 2005, Effective pressure or what is the effect of pressure?: The Leading Edge, **12**, 1256-1260.

Hornby, B. E., 1996, An experimental investigation of effective stress principles for sedimentary rocks: 66th Annual International Meeting, SEG, Expanded Abstracts, 1707-1710.

Hottman, C. E., and R. K. Johnson, 1965, Estimation of formation pressures from log derived shale properties: Journal of Petroleum Technology, **17**, 717-722.

Huerta, A. D., and D. L., Harry, 2012, Wilson cycles, tectonic inheritance, and rifting of the North American Gulf of Mexico continental margin: Geosphere, **8**, 374-385.

Huffman, A. R., 2002, The future of pressure prediction using geophysical methods, In Huffman, A.R., Bowers, G. L. ed. Pressure regimes in sedimentary basins and their predictions, AAPG Memoir, **76**, 217-233.

Huffman, A. R., and J. P. Castagna, 2001, The petrophysical basis for shallow-water flow prediction using multicomponent seismic data: The Leading Edge, **20**, #9, 1030-1052.

Hunnur, A. T., 2006, Smectite to illite transformation: relevance to pore pressure in the subsurface, MS Dissertation, University of Oklahoma.

Katahara, K., 2003, Analysis of overpressure on the Gulf of Mexico shelf: Offshore Technology Conference, 15293-MS.

Katahara, K., 2006, Overpressure and shale properties: Stress unloading or smectite-illite transformation? 76th Annual International Meeting, SEG, Expanded Abstracts, **25**, 1520-1524.

Khaksar, A., and C. M. Griffiths, 1996, Influence of effective stress on the acoustic velocity and log derived porosity: SPE **36981**, 173-181.

Kukla, P. A., L. Reuning, S. Becker, J. L. Urai, and J. Schoenherr, 2011, Distribution and mechanisms of overpressure generation and deflation in the late Neoproterozoic to early Cambrian South Oman salt basin: Geofluids, **11**, 349-361.

Kümpel, H. J., 1991, Poroelasticity: parameters reviewed: Geophysics Journal International, **105**, #3, 783-799.

Lahann, R. W., and R. E. Swarbrick, 2011, Overpressure generation by load transfer following shale framework weakening due to smectite diagenesis: Geofluids, **11**, 362-375.

Law, B. E., and C. W. Spencer, 1998, Abnormal pressures in hydrocarbon environments, in Law, B. E., Ulmishek, G. F. and Slavin V. I. eds., Abnormal pressures in hydrocarbon environments: AAPG Memoir, **70**, 1-11.

Leftwich, Jr. H. T., T. Engelder, 1998, The characteristics of geopressure profiles in the Gulf of Mexico basin. in Law, B. E., Ulmishek, G. F. and Slavin V. I. eds., Abnormal pressures in hydrocarbon environments: AAPG Memoir, **70**, 119-129.

Luo, X., and G. Vasseur, 1996, Geopressuring mechanism of organic matter cracking: Numerical modeling: AAPG Bulletin, **80**, #6, 856-874.

Lupa, J., and P. Flemings, 2002, Pressure and trap integrity in the deepwater Gulf of Mexico: The Leading Edge, **21**, 184-187, doi:10.1190/1.1452610.

Martinez, R. D., J. D. Schroeder, and G.A. King, 1991, formation pressure prediction with seismic data from the Gulf of Mexico: SPE Formation Evaluation, **3**, 27-32.

Mavko, G., T. Mukerji, and J. Dvorkin, 2009, The rock physics handbook tools for seismic analysis of porous media, second edition, Cambridge University Press, 273-281.

Mello, U. T., and G. D. Karner, 1996, Development of sediment overpressure and its effect on thermal maturation: Application to the Gulf of Mexico basin: AAPG Bulletin, **80**, #9, 1367-1396.

Meunier, A., 2005, Clays, Springer, Verlag Berlin Heidelberg, Germany, 338-347.

Mondol, N. H., K. Bjørlykke, J. Jahren, and K. Høeg, 2007, Experimental mechanical compaction of clay mineral aggregates - changes in physical properties of mudstones during burial: Marine and Petroleum Geology, **24**, 289-311.

Nur, A., and J. D. Byerlee, 1971, An exact effective stress law for elastic deformation of rock with fluids: Journal of Geophysical Research, **76**, 6414-6419.

Osborne, M. J. and R. E. Swarbrick, 1997, Mechanisms for generating overpressure in sedimentary basins: a reevaluation: AAPG Bulletin, **81**, 1023-1041.

Pollastro, R. M., 1993, Considerations and applications of the illite/smectite geothermometer in hydrocarbon-bearing rocks of Miocene to Mississipian age: Clays and Clay Minerals, **41**, #2, 119-133.

Prasad, M., 2002. Acoustic measurements in unconsolidated sands at low effective pressure and overpressure detection: Geophysics, **67**, 405-412.

Reed, J. C., C. L. Leyendecker, A. S. Khan, C. J. Kinler, P. F. Harrison, and G. P. Pickens, 1987, Correlation of Cenozoic sediment, Gulf of Mexico outer continental shelf: U.S. Department of the Interior Minerals Management Service Gulf of Mexico OCS Region.

Sarker, R., and M. Batzle, 2008, Effective stress coefficient in shales and its applicability to Eaton's equation: The Leading Edge, **27**, 798-804.

Sayers, C. M., and L. D. Den Boer, 2011, Rock physics-based relations for density and S-velocity versus P-velocity in deepwater subsalt Gulf of Mexico shales: The Leading Edge, **30**, 1376-1380.

Sayers, C. M., G. M. Johnson, and G. Denyer, 2002, Predrill pore-pressure prediction using seismic data: Geophysics, **67**, #4, 1286-1292.

Sayers, C., 2010, Geophysics under stress: Geomechanical applications of seismic borehole acoustic waves: SEG/EAGE DISC.

Shaker, S., 2007, Calibration of geopressure predictions using the normal compaction trend: perception and pitfall: CSEG Recorder, **32**, #1, 29-35.

Shuey, R. T., 1985, A simplification of the Zoeppritz equations: Geophysics, **50**, 609-614.

Skempton, A. W., 1960, Effective stress in soils, concrete and rock: Proceedings of Conference on Pore Pressure and Suction in Soils, Butterworth, London, 4-16.

Smith, N. E., and H. G. Thomas, 1970, Origins of abnormal fluid pressures: AAPG Bulletin (abstract), **54**, 1791.

Smith, T. M., C. H. Sondergeld, and C. S. Rai, 2003, Gassmann fluid substitutions: A tutorial, Geophysics, **68**, 430-440.

Swarbrick, R. E., and M. J. Osborne, 1998, Mechanisms that generate abnormal pressures: an overview: in Law, B. E., G. F. Ulmishek, and V. I. Slavin eds., Abnormal pressures in hydrocarbon environments: AAPG Memoir, **70**, 13-34.

Taylor, J., T. Fishburn, O. Djordjeevic, and R. Sullivan, 2011, Velocity modeling workflows for sub-salt geopressure prediction: a case study from the Lower Tertiary trends, Gulf of Mexico: Geofluids, **11**, 376-387.

Terzaghi, K., 1936, The shearing resistance of saturated soils, Proc. First Int. conf. Soil Mech., **1**, 54-56.

Todd, T., and G. Simmons, 1972, Effect of pore pressure on the velocity of compressional waves in low-porosity rocks: Journal of Geophysical Research, **77**, 3731-3743.

Verm, R., L. Liang, and F. Hilterman, 1998, Significance of geopressure in predicting lithology: The Leading Edge, **2**, 227-234.

Wyllie , M. R. J., A. R. Gregory, and G. H. F., Gardner, 1958, An experimental investigation of factors affecting elastic wave velocities in porous media: Geophysics, **23**, #3, 459-493.

Yassir N., and M. A. Addis, 2002, Relationships between pore pressure and stress in different tectonic settings: in Huffman, A., and G. Bowers eds., Pressure regimes in sedimentary basins and their prediction: AAPG Memoir, **76**, 79-88.

Yu, H., F. Hilterman, and A. Chaveste, 2011, Calibration of effective pressure coefficient for Gulf of Mexico shale from well-log data: 81st Annual International Meeting, SEG, Expanded Abstracts, 4409-4413.